

---

**Surface displacement of a Himalayan debris-covered glacier  
derived from automated cross-correlations using imagery  
acquired with unmanned aerial vehicles**

---

Master Thesis

By Sander Meijer



Supervised by Prof Dr Steven de Jong & Dr Walter Immerzeel

16 June 2015

Research thesis of Sander Meijer <sup>1</sup>

Supervised by Prof Dr Steven de Jong <sup>2</sup>

Dr Walter Immerzeel <sup>3</sup>

Master Thesis in Physical Geography, Utrecht University

Master degree: Earth Surface and Water

Master track: Fluvial Systems & Coastal dynamics and Geohazards & Earth observation

<sup>1</sup> Utrecht University, meijer3@gmail.com, 4086880

<sup>2</sup> Utrecht University, W.W.Immerzeel@uu.nl

<sup>3</sup> Utrecht University, S.M.deJong@uu.nl

<sup>1,2,3</sup> Department of Physical Geography, PO Box 80115, Utrecht, The Netherlands

***Dedicated to the Nepalese people and culture, that suffered in the  
Kathmandu Valley, Langtang National Park and any other hit region  
during the Kathmandu Earthquake in 2015***

# Preface

---

This thesis contributes to increase the general understanding of the melting behaviour of debris-covered glaciers. It helps to predict future river discharges of the major rivers in Asia. This research is the first to monitor glacial surface displacements on a high spatial scale of 0.1 m. This is done with a UAV dataset from May 2013 until May 2014.

It was an incredible opportunity to do fieldwork under such extreme environments. The research, the international team, the local people, the high-altitude mountains and the severe cyclonic storm Hudhud made my fieldwork an unforgettable experience.

I would like to thank Steven de Jong, Walter Immerzeel and Philip Kraaijenbrink for their supervision and assistance during this research and fieldwork. They put in a lot of effort in making the fieldwork possible. They also made it possible to publish the research in the paper '*Seasonal surface velocities of a Himalayan glacier derived by automated cross-correlation of unmanned aerial vehicle imagery*'. I would also like to thank Utrecht University for fieldwork remuneration and especially the Board of Examiners of geosciences for allowing me to go to Nepal. Additional thanks go out to Joseph Shea, Fionna Heuff, local porters and the trekking agency *Glacier Safari Treks* for their contributions to the fieldwork. Special thanks to kfHein foundation for funding my fieldwork to Nepal.

# Abstract

---

Glacial melt water is a source of drinking water for the 1.3 billion people living in downstream area of the Hindu Kush Himalayan region. Himalayan glaciers function as a fresh water buffer as they constantly release water, making it an important resource for people during the dry season. In this research, surface displacements are studied in order to understand more of the melting behaviour of debris-covered glaciers. Understanding these processes will help predict future water levels in rivers.

In situ, glaciological measurements are limited due to the inaccessibility of the glacier and need to be interpolated to assess the full surface dynamics. In this study, imagery of the Lirung glacier in Nepal is used that is derived from an unmanned aerial vehicle (UAV). The dataset is ortho-rectified and covers almost a full year including a summer and a winter season. The flight data are May 2013, October 2013 and May 2014. Based on a Structure from Motion process digital elevation models and ortho-rectified mosaic images are created.

Some of the glaciers in the Himalaya are covered with debris. This allows tracking the rocks on top of the glacier, where rocks move upon with the ice. The frequency cross-correlation of Cosi-Corr is using the phase in the Fourier domain to track such debris. The output of this correlation is a continuous raster map containing the surface displacement of the glacier. Fine spatial and general seasonal differences can be found in the surface displacement. During the summer, the maximum average displacement is  $6 \text{ m a}^{-1}$  while the winter displacement is  $2.5 \text{ m a}^{-1}$  at the upper part of the tongue. The lower part is nearly stagnant throughout the year. It is very likely that basal sliding is the dominating process during the higher summer. It is hypothesized that the increment of both temperature and rainfall during the summer causes a lubrication of the bedrock. Other process on the glacier is a yet unknown depression, which can be found to the north of the terminus and emergence velocities that occur near the bend of the glacier.

The high-resolution imagery and elevation models of UAVs have high potential to map surface displacements of debris-cover glaciers and help to understand general glacier dynamics on a small spatial scale.

# Table of Contents

<b>1. Introduction .....</b>	<b>7</b>
1.1. Regional impacts .....	8
1.2. Debris-covered glaciers .....	12
1.3. Traditional observations on glacial flow .....	13
1.4. Research aims .....	15
<b>2. Theoretical Background .....</b>	<b>16</b>
2.1. Glacial flow .....	16
2.2. Software .....	20
2.3. Unmanned Arial System .....	22
<b>3. Study Area .....</b>	<b>23</b>
3.1. Climate .....	24
<b>4. Method.....</b>	<b>26</b>
4.1. Fieldwork .....	26
4.2. UAV-based Structure from Motion process.....	28
4.3. Auto Cross-Correlations by Cosi-Corr.....	30
4.4. Model .....	42
<b>5. Results.....</b>	<b>42</b>
5.1. Optimal configuration .....	42
5.2. Quality of assessment .....	48
5.3. Seasonal differences .....	50
<b>6. Discussion .....</b>	<b>52</b>
6.1. Optimal Configuration .....	52
6.2. Accuracy of displacement .....	53
6.3. Glaciological interpretations .....	58
6.4. Summary .....	63
<b>7. Conclusion .....</b>	<b>64</b>
<b>8. Recommendations .....</b>	<b>66</b>
8.1. Further research.....	66
8.2. Optimal workflow for glacial displacement .....	66
<b>9. References.....</b>	<b>69</b>
Appendix A, Glacier terminology .....	73
Appendix B, IDL model .....	75

# 1. Introduction

---

The high-mountain range of the Hindu Kush Himalayan (HKH) region is frequently referred as 'the water towers' of Asia. One in five people in the world depend on water from these mountains. The region contains the third largest ice reserves in the world and the glaciers work as a fresh water buffer. Climate change induces glaciers to melt and the long-term result of this is water shortage.

Glacial melt contributes to the major rivers in Asia. This water is a major component in the ground water flux. Without glacial melt, the ground water level will drop in the HKH region. In Bangladesh 80% of irrigation-water and 97% of the drinking water originate from groundwater and thus are dependent on glacial water. India is the biggest consumer of ground water by volume. More than 60% of the water is used for irrigation. In India Bangladesh Pakistan and Nepal the annual groundwater withdrawal is approximately 35% of the world's renewable fresh groundwater withdrawal, nearly 250 km<sup>3</sup> water ([Siebert et al. 2010](#)).

A large proportion of this is used to produce rice, which is grown for the international market. Many companies face serious water shortages, especially in the dry season due to a smaller discharge in the rivers. More than 50% of the 1.3 billion people that live downstream work in the agricultural sector ([Weingartner and Messerli 2003](#)).

Drinking water supplies, energy provision, industry and irrigated agriculture partly depend on glacial melt water. A decrease in discharge will increase the problems that occur already. The unsustainable use of water is large, especially in less developed regions. Polluted waste water and overpopulation are examples of problems that already occur ([Mishra 2010](#)). Irrigation related problems could cause basic life support issues to local communities in northern India. The communities have drinking water problems due to ([Siebert et al. 2010](#)) dropping water tables. Drinking water and food production are sensitive sectors and this industry is dependent on a continuous flow of rivers. The level of the groundwater table is based on several factors, but river discharge is one of the most important factors and thus glacial melt. It has been reported that the ground water tables are declining in regions in the HRH region. The withdrawal is bigger than nature could renew and the problems increase when there is a lack of glacial melt water in rivers.

### 1.1. Regional impacts

The Hindu Kush Himalayan (HKH) region covers eight countries and is the source of the 10 major rivers in Asia. It extends over 3500 km and covers 4.3 million square meters in Afghanistan, Bangladesh, Bhutan, China, India, Myanmar, Nepal, and Pakistan. The region contains the world highest mountain range including the only 14 peaks above 8000 MASL in the world and contains unique high altitude glaciers. It is the world largest storage of ice (16%) outside the Polar Regions and is often called *The Third Pole* (ICIMOD 2014). The 67000 glaciers in the HKH region cover an area of  $1.2 \times 10^5 \text{ km}^2$ . If these fresh water reserves melt, the sea level will rise with 29,7 mm (Vaughan et al. 2013).



Figure 1, In green the Hindu Kush Himalayan Region; in blue the 10 major river basins; Red dot Langtang area; image derived from (ICIMOD 2014)

More than 210 million people live in the HKH region. 1.3 billion people and thus a fifth of the world population lives in the downstream basins of the Amu Darya, Indus, Ganges, Brahmaputra, Irrawaddy, Salween, Mekong, Yangtze, Yellow River and Tarim. The Ganges river basin is extremely densely populated and with 401 persons per square kilometres, it is the highest population density in all Himalayan river basins. It supports the life of 410 million people and nearly two-third depend on agriculture as their occupation (ICIMOD 2014).

The Indus and the Tarim have high percentages of melt water, respectively 45% and 40%. The discharge of the Indus is at a maximum of 151% of its original volume generated by snow and glacial melt (W. Immerzeel et al. 2010). During the dry seasons, lack of melt water could result in serious water shortages. A quarter of the total Chinese population depend on melting water in the dry season. Lack of water could cause enormous economic damage because water is used in many production chains. Agriculture, hydroelectric plants, Bangladesh clothing manufactures, drinking water companies and many other sectors rely on a constant supply of water. The rivers are a source of food and energy and half of the world population indirectly benefits from this region (Jianchu et al. 2007).



	Indus	Ganges	Brahmaputra	Yangtze	Yellow
Total area (km <sup>2</sup> )	1.005.786	990.316	525.797	2.055.529	1.014.721
Total population (10 <sup>3</sup> )	209.619	477.937	62.421	586.006	152.718
Annual basin precipitation (mm)	423	1.035	1.071	1.002	413
Upstream area (%)	40	14	68	29	31
Glaciated area (%)	2	1	3	0	0
Annual upstream precipitation (%)	36	11	40	18	32
Annual downstream precipitation (%)	64	89	60	82	68
Irrigated area (km <sup>2</sup> )	144.900	156.300	5.989	168.400	54.190
Net irrigation water demand (mm)	908	716	480	331	525
Mean Discharge (m <sup>3</sup> s <sup>-1</sup> )	3.850	15.000	19.824	35.000	1.365
Glacial melt in flow (%)	44,8	9,1	12,3	18,5	1,3

Table 1, Five major rivers in the HKH region. Irrigation is important in many areas in the adjacent lands; a significant part is melt water (Immerzeel et al. 2012; Jianchu et al. 2007)

#### 1.1.1. Current state

In the HKH region, there is no uniform pattern in glacial behaviour. More than 65% of glaciers that are monsoon-influenced are retreating. Only a small fraction of the remaining 35% is advancing, the majority is mainly stable or stagnant. In Karakoram region, 58% of the glaciers are stable or even accumulating, see Figure 2. Scherler et al. (2011) researched the spatial variability response of HKH glaciers affected by the change in climate. Two spatial transitions determine the differences in climate and topography. Firstly, there is an increase of winter westerlies rainfall from west to east. The glaciers in Karakoram receive 50% of the annual precipitation during winter, while the rest of the Himalayas have only 20-30% precipitation during this season. The very steep terrains surrounding the glaciers in Karakoram cause more snow avalanches that contribute to accumulation (T. Bolch et al. 2012). Secondly, the Indian monsoon creates a lot of orographic rainfall in India while the Tibet plateau is arid (Bookhagen and Burbank 2010).

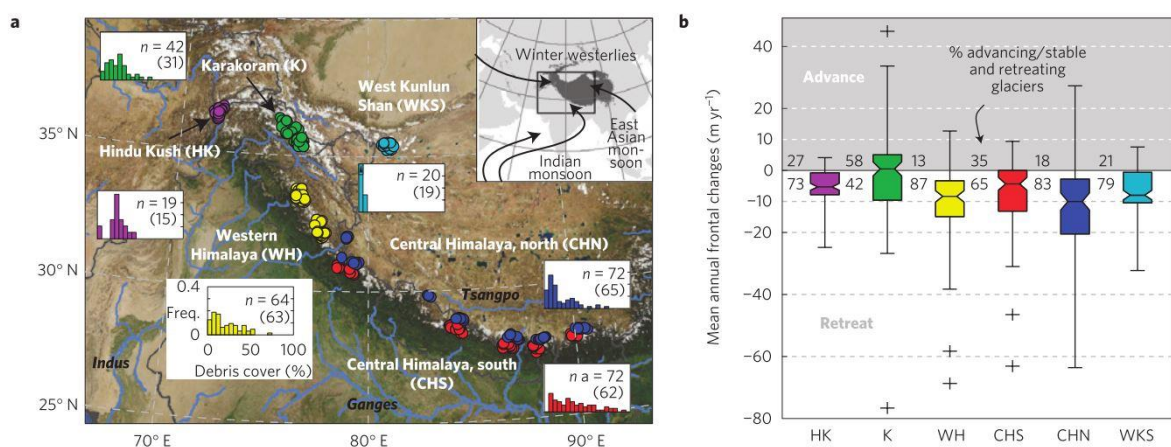


Figure 2, Left: Spatial variation of debris-covered glaciers. The winter westerlies are shown in the top right corner. Precipitation events could be related to the state of glaciers. Right: Mean annual frontal changes per region. Some regions are advancing. On average 65% of the glaciers are retreating. (Scherler, Bookhagen, and Strecker 2011)

On average, glaciers in the Karakoram region have positive glacial elevation differences, see [Figure 3](#). Many large glaciers are stable or have advanced recently in this region, due to increased winter snowfall and summer storms ([A. Kääb et al. 2012](#)).

Rock avalanches cause debris covers in central Himalaya and 13% of the glaciers there are debris-covered ([T. Bolch et al. 2012](#); [Earth et al. 2013](#)). In Bhutan, glaciers with a high accumulation can reach flow velocities of 100 to 200 m a<sup>-1</sup>. According to Bolch, glaciers beneath rock-headwalls, such as the Lirung glacier, have speeds <50 m a<sup>-1</sup>. Not all glaciers are controlled by precipitation. The behaviour of some glaciers, especially in the Karakoram area, depends on thermal conditions ([Quincey et al. 2011](#)).

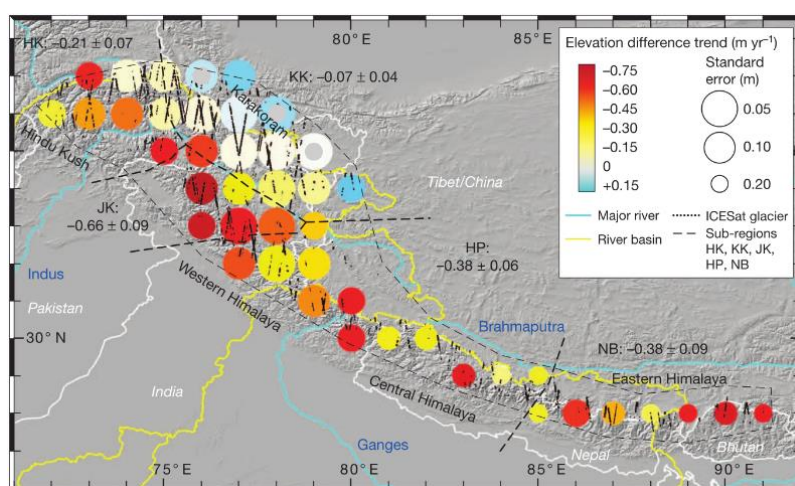


Figure 3, Study region and trends of elevation difference. Trends are based on autumn ICESat acquisitions. Trends of all cells (coloured data circles) are statistically significant except for the three cells in the Karakoram that are indicated with grey centres. Errors are one standard error. ([A. Kääb et al. 2012](#))

#### Melting glaciers in current climate

Glacial melt contributes to sea-level rise. In a period of 5 years (2003-2008) the contribution of the Himalayas was  $+0.035 \pm 0.009$  mm a<sup>-1</sup> ([A. Kääb et al. 2012](#)). Since the last Little Ice Age, between 700 and 200 years ago, glaciers have been globally retreating. In this period the temperatures were the lowest in centuries, which allowed glaciers to advance ([Barry 2006](#)). In the current state of the climate, it is warmer and therefore more than 65% of glaciers that are monsoon-influenced are retreating. The last time that the majority of the Himalayan glaciers were advancing was between 1920 and 1940 ([T. Bolch et al. 2012](#)).

#### High altitude precipitation

Precipitation, especially snow, feeds the glaciers. Little is known about the regional horizontal and vertical distribution of precipitation, especially at high altitude ([T. Bolch et al. 2012](#)). An increase in elevation and thus in temperature causes more snowfall, not necessarily more precipitation ([Bookhagen and Burbank 2010](#)). However, some scientist state that there is an correlation between altitude and precipitation ([Winiger, Gumpert, and Yamout 2005](#)). Most of the precipitation occurs in the area before the hinterland and therefore the location of a glacier is important relative to the track of the rainfall events. The amount of snowfall also depends on the shape of the precipitation curve of events and how much precipitation will fall, as shown in [Figure 4](#).

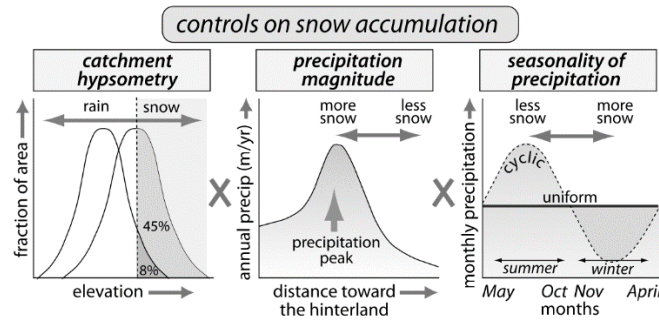


Figure 4, Conceptual summary of three dominant factors: hypsometry, spatial distribution of precipitation and seasonality of precipitation. Higher elevations, greater proximity to the precipitation peak and a longer winter season lead to more snow accumulation. (Bookhagen and Burbank 2010)

### 1.1.2. Climate change

Various studies show a global change in climate (Vaughan et al. 2013; Scherler, Bookhagen, and Strecker 2011; Fujita and Nuimura 2011). Hindu Kush Himalaya region glaciers are amongst the most sensitive glaciers in the world. The number of days that have a snow cover at elevations between 4000 and 6000 MASL. has decreased by 23 days since 1966. The region has been warming up at an annual rate of 0.16°C per decade. Winter temperatures have been rising 0.32°C per decade (Rikiishi and Nakasato 2006; Xu et al. 2009; Walter W. Immerzeel et al. 2012).

An increase in temperature can be seen in annual patterns. Six out of ten of the warmest years from 1900 until 2002 occurred in the last seven years. Change in precipitation is not clear, but high altitude precipitation is yet unknown so early records are lacking.

Most of the climate models are global, but it is difficult to downsample to high altitude and relief terrains such as the Langtang catchment. In HKH region, rainfall is strongly correlated to the Indian monsoon, while snowfall is caused by winter westerlies. We see a global trend for such processes, but it is hard to predict this on local scale. Immerzeel (2008) downscaled five global climate models to the Langtang based on hydrological processes such as evapotranspiration, surface runoff, ablation and base flow.

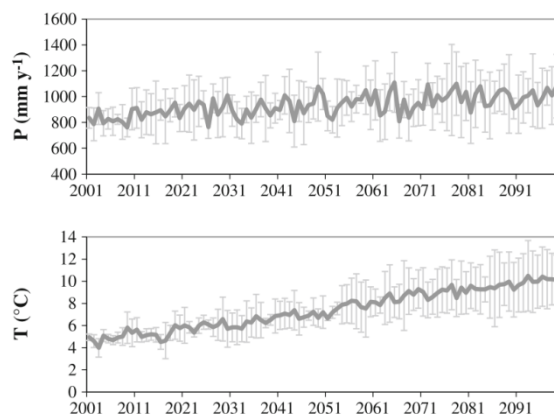


Figure 5, Increasing trend in both mean monthly precipitation and temperature for the lower Langtang catchment at Kyanging. Error bars are one standard error from five GCMs. Both show clear trends in rising precipitation and temperature (Walter W. Immerzeel et al. 2012)

A human-introduced process is black carbon. It darkens the surface and influences the melting behaviour of the ice. The black particles absorb a greater heat flux of  $+0.054 \text{ W m}^{-2}$  from  $0.007$  to  $0.13 \text{ W m}^{-2}$ . 80% of all black carbon is emitted from fossil fuels and this will increase in the future (Vaughan et al. 2013).

## 1.2. Debris-covered glaciers

Debris-covered glaciers have a unique response to climate change. Most debris-covered glaciers are isolated by the debris. The extra-glacial debris is rock material that avalanches from the surrounding slopes. Another source of debris is caused by crevasse squeezing of subglacial sediments, melt water bursting through the crevasse and conduit system, or Aeolian transport directly onto the glacier. (Reznichenko et al. 2010; World Glacier Monitoring Service 2008; Schomacker 2008). Östrem (1959) did research into the layer of moraine debris on top of glaciers. According to him there are four ways in which absorbed energy will be distributed.

1. Outgoing (long wave) radiation
2. Energy loss to the air by convection and conduction
3. Evaporation of melt water which has risen in the sand and gravel by capillary action
4. Melting of glacier ice

The albedo of a debris layer is lower than that of a plain ice layer and therefore it will absorb more energy. This could result in an increased melting of the ice. In his experiment, a debris thickness of  $0.5 \text{ cm}$  created maximum ablation. If the cover is thicker, the layer has a more insulating effect, because evaporation of melting water is not possible anymore. Nicholson & Benn (2006) plotted a curve of their similar experiments. It shows ablation per day in function of the thickness of the debris layer for several glaciers, see Figure 6.

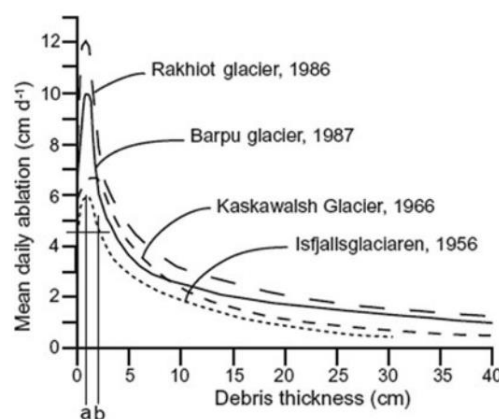


Figure 6, Ablation curve relative to the thickness of the debris layer. Small layer of debris decrease albedo and increase ablation, while a thicker layer has an insulating effect (Nicholson and Benn 2006).

The curve shows a clear diminution in ablation when the debris-layer is thicker. On a global scale 79-86% of the glaciers are retreating, especially in regions where debris-covered glaciers are uncommon (Scherler, Bookhagen, and Strecker 2011). The critical thickness is approximately 8 cm (Mihalcea et al. 2006), from this point on the debris layer has an insulating effect. It releases more energy at night than it conducts to lower layers. The critical thickness decrease with increasing altitudes, due to four parameters: humidity combined with water pressure, ablation rates of bare ice, diurnal amplitudes of radiation, shortwave radiations (Reznichenko et al. 2010).

### **1.3. Traditional observations on glacial flow**

It is essential to understand glacial flow to predict a changing melting behaviour caused by climate change. If the flow can be predicted, improved glacial models and estimations can be made. The traditional observations, mainly consisting of tracking bamboo stakes, are limited to sparse point cloud of data.

#### **1.3.1. Traditional observations**

The traditional method to monitor the dynamics of a glacier in the field is using ablation stakes. These are bamboo sticks that are drilled into the ice, because mainly the top part of a glacier is melting, the stick is fixed in the glacial ice. They move together with the ice and more parts of the stake are exposed if the top layer is melting. Position can be measured with a differential GPS and the ablation can be measured.

Another method for measuring surface displacement is by using (semi)-permanent Global Navigation Satellite System (GNSS) receivers (Rosu et al. 2014). Small dGPS devices are placed on the glacier and they measure the displacement. The disadvantages of systems like these are that the area should be under surveillance and the equipment is expensive.

Both stake- and GNSS methods collect sparse data. Glaciers are rough terrain and often hard to access. Many glaciers are located in remote area and have extreme weather conditions. Glaciers have often cliffs, water bodies, deep fractures and other obstacles. Measurements can only be limited to a number of locations due to this inaccessibility. These methods provide point spacious data or it covers a small area with high resolution. The rest of the glacier is estimated or interpolated based on this point cloud.

#### **1.3.2. Remote Sensing**

Deformation of glacial surfaces based on remote sensing has been researched in many papers (Dowdeswell and Benham 2003; a. Kääb 2005; Heid and Kääb 2012; a. Kääb and Vollmer 2000; Fujita et al. 2008; Racoviteanu, Williams, and Barry 2008; Copland et al. 2009). Crevasse tracking is commonly used to track bare-ice glacial deformation. Redpath et al. (2013) used ASTER (Advanced Space-borne Thermal Emission and Reflection Radiometer) images to determine motion of the Tasman Glacier in New Zealand. They successfully tracked crevasses with the first band of the ASTER imagery. They tried Principle Component 1 and the panchromatic band, but they found them less useful due to the amount of mismatches. They used a feature tracker called CIAS (Correlation Image Analysis).

The newer geodetic method uses remote sensing datasets and is space-borne or air-borne. Two systems can be found in remote sensing, active and passive systems.

The active systems send out a signal and measure the incoming reflected signal. Therefore, it does not depend on an external light source, such as the sun. In most cases Digital Elevation Models (DEM) can be formed. LiDAR systems have high accuracy and have potential for surface flow monitoring. Usually air-borne LiDAR have a spatial resolution of 1-2 meter resolution and vertical 5-15 cm. The DEM is suitable for comparison on annual basis. The advantage of LiDAR is the near-infrared wavelength laser that is capable of detecting snow cover ([Arnold et al. 2006](#)). The space-borne GLAS sensor of ICESat is also laser-based and can create DEM with a spatial resolution of approximately 70 meters. This is used for global monitoring of glaciers ([Carabajal and Harding 2005](#)). The Shuttle Radar Topography Mission (SRTM) was launched in 2000 and derived DEM (SRTM-DEM) can be used for monitoring but depend on snow conditions and the resolution is 30 meters ([Fujita et al. 2008](#)). Interferometry Synthetic Aperture Radar (inSAR) can be ground-based or space-borne. The sensor sends out a very narrow beam that is reflected in a certain way by the surface material and medium. When the beam is reflected, it has a specific amplitude and phase difference. Due to these characteristics, the length of the path and the absorption capacity of the ground material can be estimated. DEMs are computed by comparing the phase difference of two data sets. It can operate with cloud cover and can be used for glacier monitoring ([Sund, Lauknes, and Eiken 2014](#)).

Passive systems take photographs from air-borne or space-borne carriers. They could create DEMs by photogrammetry of stereo imagery. Most of the systems have a nadir-looking and a non-nadir-looking camera that can be used for stereo-photogrammetric DEMs. Most of the passive systems depend on the sun as their light source.

The previous American intelligence satellite Corona has two panoramic cameras with a separation angle of 30°. It has a spatial resolution of 2 to 8 meters in stereo coverage. Corona is capable to generate DEMs and operated between 1959 to 1972 ([Tobias Bolch et al. 2008](#)).

The ASTER sensor on the Terra satellite also captures stereo imagery and has a spatial resolution of 15 m in Near Infrared (NIR). The time difference between the nadir-looking visible/near-infrared and the backward-looking bands is approximately 55 s ([Fujita et al. 2008](#); [Nuimura et al. 2012](#)). The standard ASTER DEM automated delineation using multi-spectral imagery have inaccuracies in terrain with high relief as well supra-glacial debris ([Tobias Bolch et al. 2008](#)).

Spot (Système pour l'Observation de la Terre) has been used to create DEMs. The older SPOT5 and SPOT6 images have a spatial resolution of 2-2.5 meters. The new SPOT 7 –launched on 30 June 2014- is orbiting parallel to the older SPOT 6. They are designed to cover wide areas in record time. The SPOT series have been operating since 1986 and will operate until 2024.



All GeoEye-1, Worldview1 2 3, IKONOS, Pleiades have extreme high spatial resolution, between 34 and 81 cm (Juen et al. 2014). Worldview 4 (before: GeoEye-2) will be launched in 2016 and has a panchromatic resolution of 0.3 meter and multispectral resolution of 1.20 meter.

The generated DEMs from space-borne satellites are made for large scaled areas. The majority have relative coarse resolutions of tens of meters, but more important the vertical error of these elevation maps is typically not less than 10 m (Rippin et al. 2003; Wagnon et al. 2013; Nuimura et al. 2012)

Raw imagery has no physical geographical coordinates. In most cases the spatial position and elevation of the sensor is known, but in combination with distortion by lens and terrain, this is in most cases not enough. Well-measured points on the surface can be linked back to the image. These points are called Ground Control Points (GCP) and help to ortho-rectify the image to give real world coordinates to points in the image. This way the image is positioned on the right coordinate system and correct for relief. Ground control points need to be measured by dGPS in remote glacial areas and this could be problematic. The resolution of the used sensor determines the minimum size of features that can be used as GCP. If the spatial resolution is 10 m, not every feature that is smaller than 10 m is visible.

#### 1.4. Research aims

Knowledge about spatiotemporal dynamics of glaciers is essential to improve discharge predictions of the major rivers in Asia. Many glaciers are losing mass, but this is partly a natural process as the climate is changing since the Little Ice Age 200 years ago. However, it is well-known that emissions of fossil fuels accelerate the rate of climate change. It is yet unknown how climate change trends will evolve and how glaciers will respond in time (Immerzeel et al. 2012). To predict glacial mass loss the glacier dynamics and melting processes need to be studied and monitored.

The aim of this research is to **improve our understanding of processes in glacier surface dynamics and melting behaviour of debris-covered glaciers in the Himalayas.**

Glacial dynamics will be assessed by comparing surface flow velocities with the use of remote sensing. To do so a case study is conducted for the Lirung glacier in Langtang national Park in Nepal

To study how surface displacements are related to flow and melting processes, it is necessary to understand general glacial dynamics. Therefore, a literature research is conducted about how glacier dynamics are represented in the displacement of a glacial surface.

In previous glacial studies (T. Bolch et al. 2011; a. Kääb 2005), satellite imageries were used. The disadvantage of such imagery is that they have a low spatial resolution and contain atmospheric clouds. The width of glacier is only captured in a few pixels, which is not enough to study the complete surface dynamics. Therefore, an Unmanned Aerial Vehicle (UAV) is used to create high-resolution datasets. The high-resolution UAV imagery has a lot of detail and thus smaller flow

variations can be detected. In this research, the cross-correlation algorithm of the Cosi-Corr software will be used to determine surface displacements.

This includes an assessment about input data and configurations of Cosi-Corr. The automated Cosi-Corr's correlation maps will be compared with manually tracked points. Both the UAV data and the automated cross-correlation technique will create an error, which should be understood before interpreting any signals.

After the error is determined, the physical interpretation steps can be made. Spatial variations and seasonal variations are expected in surface dynamics. There are also features that can be found on glaciers that are important for melting processes, such as ice cliffs, termini and drainage systems.

All these specific research questions should increase knowledge about glacial surface dynamics and lead to a better understanding of glacier melting processes.

***To what extent can automatic cross-correlations based on UAV imagery be used to determine surface displacement at debris covered glaciers?***

***What is the accuracy of automatic displacement maps based on UAV data?***

***Which processes play a role in spatial and seasonal variations in melting behaviours?***

## 2. Theoretical Background

---

The academic background of this research is presented in this chapter, starting with the importance of glaciers in the greater Hindu Kush Himalayan region and its climate, followed by physical processes of glacial flow and glaciation, and the final subchapters contain the methods to monitor glaciers and pre-processing for cross-correlations. For glacial terminology, see [Error! Reference source not found.](#)

The location where glaciers form depends on several factors. Both the air temperature and precipitation are important. The physical characteristics of the terrain have large impact, such as slope, aspect, incoming solar radiation and geomorphology. Those factors play also a role in how glaciers are shaped.

### 2.1. Glacial flow

Glacier flow depends on several factors such as, ice geometry (thickness, steepness), ice properties (temperature, density), valley geometry (slope, curves), bedrock conditions (hard, soft, frozen or thawed bed), subglacial hydrology (washout patterns), terminal environment (temperature, altitude) and mass balance (rate of accumulation and ablation). All these factors have influence on the glacier flow. Knowledge about glacial deformation and flow processes are essential to understand surface flow.

#### 2.1.1. *Glacial deformation*

Ice move downhill due to the combination of gravitational pressure and hill slope. Glacial ice is a visco-plastic material, so it can be deformed (plastic) as well as flow (viscous). The gravity applies



a shear stress on the ice and due to plastic deformation of ice, the glaciers ice can flow downhill. (Harper et al. 2001) The stress that deforms the ice, this is called strain. Strain is important to glacier dynamics and can be either elastic or permanent, see Figure 7. Characteristics of glaciers can act differently at certain depths. There are two vertical zones: a brittle zone and a ductile zone where the brittle zone is placed on top of the ductile zone

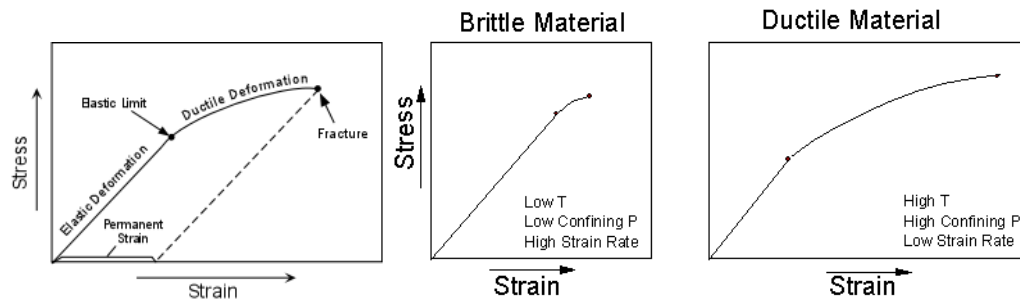


Figure 7, Left: The strain of elastic deformation is reversible, ductile deformation is permanent. Centre and right: Difference between brittle and ductile zone. The brittle material is more elastic at a given stress but fractures at a lower strain level than ductile material would (Harper et al. 2001).

In the brittle zone (sometimes: zone of rigid flow) the firn and ice will behave as a solid material. It fractures if subjected to stress that are larger than the internal strength. Crevasses, cracks in the firn, are found in this upper layer. They commonly develop in glaciers where the ice thickness decreases due increasing bed level. The brittle zone will move to faster than the bottom creating greater stress than the internal strength of the ice. The ductile zone (sometimes: zone of plastic flow) is the deeper part of the glacier that is under high pressure. The weight of the ice gives the ice its visco-plastic behaviour (Cuffey and Paterson 1970).

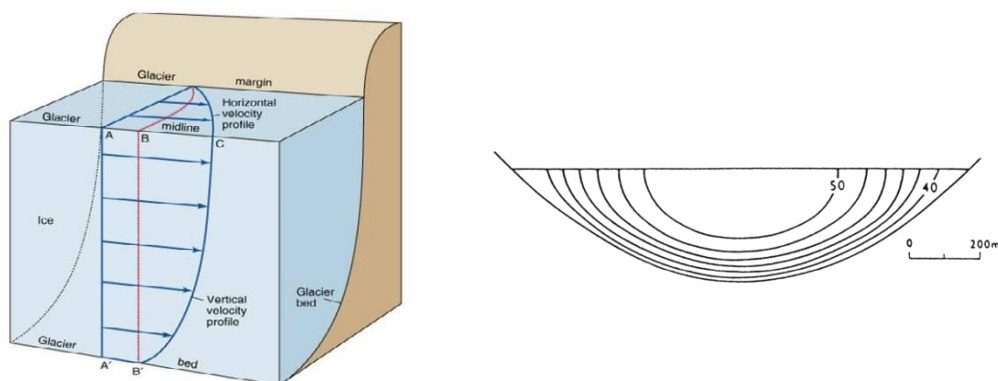


Figure 8, Left: Double cross section of glacial flow in ductile zone. Line AC is the maximum movement. That is caused by basal sliding and internal deformation. There is a logarithmical increase (B'C) of the internal deformation. The lines AB and A'B' indicate the basal sliding. Note that the basal sliding is also decreasing near the side of the glacier. Right: Longitudinal velocity ( $\text{m y}^{-1}$ ) in a transverse cross section calculated for a glacier with no basal sliding in a parabolic channel (J. F. Nye 1965)

The velocity of the ice varies within the glacier due the friction along the walls and the bedrock, as shown in Figure 8. Ice velocities are higher at the surface than near the bed. Longitudal moraines create shear stress that creates a drag near the sides of the glacier, allowing the ice at the centre of the glacier flow much faster (J. F. Nye 1965). The examples in Figure 8 are perfect parabolic and therefore the flows are symmetric. However, this is exceptional in nature.

### 2.1.2. Flow processes

There are two ways glacial movement: Basal sliding and internal deformation. Basal sliding is the movement of a mass on a slope. Internal deformation is a process of glacial flow due to the viscosity and pressure of the ice. With both processes, the ice mass moves downhill.

#### Basal sliding

Basal sliding is movement of the whole glacier that is slipping on bedrock. Basal slip is created by the pull down forces by gravity over any object on a slope that causing motion. A small layer of melt water at the ice-rock interface reduces friction and works as a lubricant. The water is either melted ice due to the earth internal heat, melt water from near the surface or the water is melted due lowering of the pressure-related melting point. Cold-based glaciers have almost no basal sliding due to lack of this layer of water and the ice is frozen to the bedrock. Temperate glaciers do have basal slide and therefore they move much faster than cold-based glaciers. Approximately 60 to 80% of the total velocity in temperate glaciers is accounted for by basal slide (Harper et al. 2001).

Near the longitudinal moraines the ice is often shallower and therefore the velocity decreases due to the relative higher friction of the bed and moraine drag (Cuffey and Paterson 1970). The basal slide velocities are uniform throughout depth. The shear stress from the bed determines largely the magnitude of the velocity. Bed shear stress depends mainly on the bed roughness and bed softness. Soft beds tend to erode faster, apply less stress and can have sub-glacial deformation.

The bed roughness depends mainly on processes as *Enhanced Basal Creep* and *Regelation*. In both processes, the ice encounters an obstacle. Regelation (<1 m) melts the ice and refreeze. If an object is in the flow path, the pressure in front of the object increases, the pressure builds up and the melting point drops. The ice will melt and flow to a region where the pressure is low. This is after the obstacle were vacuum occurs. The freezing point here is at a lower temperature due to the lower pressure and the water refreezes. By enhanced basal creep the ice moves around the obstacle (>1 m) and plastically deform the ice around the obstacle. The melting point is not reached or the morphology can easily lead the ice around the obstacle.

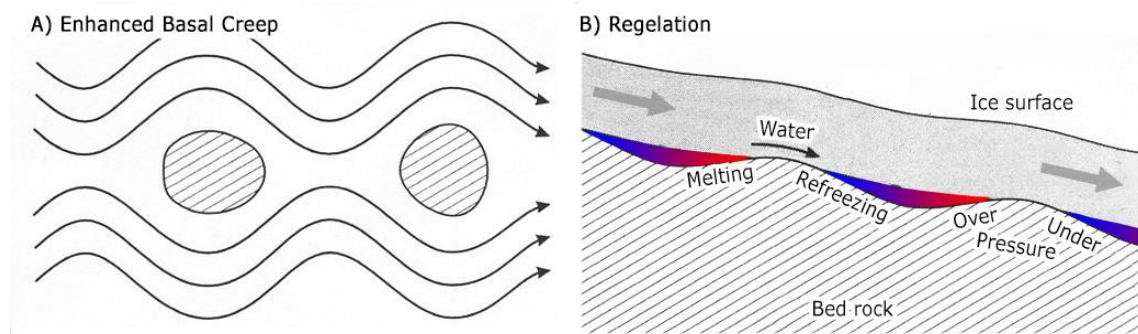


Figure 9, *Left*: Enhanced Basal Creep, ice is moving around an obstacle. *Right*: Regelation, ice is melted due to the high pressure, water flows to an area where the pressure is low. There it refreezes because the pressure is low again. There is a latent heat flow upstream. Updated from: Cuffey & Paterson, 1970.

Basal slide have the same processes as all other mass on a slope. The glacier thickness, the ice density and the slope influence the drag of the ice-bedrock interface. The gravity pulls the ice mass down over a slope  $\beta$  (°) creating the driving force.

$$\tau_b = \rho g H \sin(\beta) \quad (1)$$

Where  $\tau_b$  is the basal shear stress (Pa),  $\rho$  is the ice density,  $g$  is the gravitational acceleration ( $\text{m s}^{-2}$ ),  $H$  (m) is the ice thickness. This driving force should exceed the equilibrium shear stress. Weertman (1957) sliding law both include regelation and basal slip mechanisms in his equation –if the glacier is temperate.

$$\tau_b \approx v^2 R u^{\frac{2}{n+1}} \quad (2)$$

Where  $R$  ( $\text{Pa s}^{1/3}$ ) is a material coefficient based on Clapeyron effect,  $n$  is the creep constant of nonlinear Glen's flow law, with  $n \approx 3$ ,  $u$  is the sliding speed ( $\text{m s}^{-1}$ ). The two equations can expressed together in the following equation:

$$u^{\frac{2}{n+1}} = (\rho g H \sin(\beta) - \tau_0) (v^2 R)^{-1} \quad (3)$$

This equation result in glacial sliding speed in function of the ice thickness, slope and bedrock properties.

#### Internal deformation

The internal deformation is the way ice flows and is a process where, under huge pressure, the ice crystals rearrange themselves in layers parallel to the surface. Within the ice crystals, the water molecules are arranged in layers of hexagonal rings and this ring is called the *basal plane* of crystal. The normal to the basal plane is called the *optical axis* or the *c-axis* of a crystal (Funk 2009). Under the high pressure, the basal planes align and become coplanar. The bonds between crystals in the basal plane direction are stronger than bonds aligned to the c-axis. Therefore, ice is able to gliding on its basal planes. Ice crystals that are not rearranged can move, but need 100 time more pressure (Hansen, L 2014). This process happens only near the bottom where ice is thick and can deliver enough pressure for non-recrystallization movement.

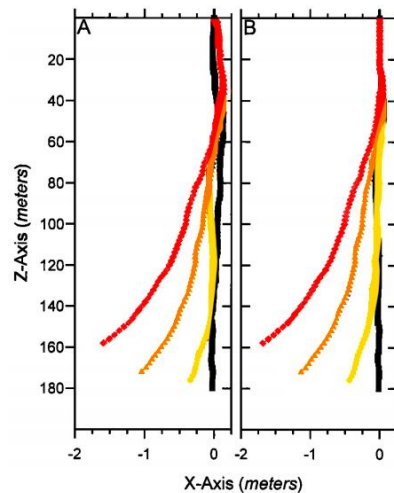


Figure 10, Inclinometer data from boreholes at the Worthington Glacier, Alaska. The black lines are measured after drilling, the red lines at the left-hand side after 70 days. Inclinometer data from basal slide would not be visible because the straight lines would be projected on each other (Harper et al. 2001)

The brittle zone lifts on top of the ductile zone, the internal deformation can be neglected in this upper layer. There is no much pressure and thus less internal drive. However, the internal deformation velocity is maximum here since the internal deformation accumulative towards the top. The surface layers lifts on a layer that is moving a little bit, that lifts on another moving layer, et cetera. The layers near the bottom have the greatest internal drive but move the slowest. This can be seen in Figure 10 were Harper et al. (2001) drilled boreholes in the ice of the Worthington Glacier, Alaska. They remeasured the boreholes three times with a final time span of 70 days. The basal slide is negligible since they plotted the boreholes on the same position.

## 2.2. Software

Surface deformations in two temporal orthorectified images can be seen as optical motion flow. There is many software packages available to measure the flow between two images, especially in computer-vision (Szeliski 2010; Triggs et al. 2000; Radke 2012; Sun, Roth, and Black 2010). For this study, one software package is taken in order to limit the extent of the research. For glaciology there are already developed several software packages. ImGRAFT, IMCORR and CIAS are designed to monitor glacial deformations. Cosi-Corr and Micmac are two packages that are developed to map mass movement and ground deformations, but both are also used in other fields.

**IMCORR** is developed at the National Snow & Ice Data Center (NSIDC 2006) by Scambos, Dutkiewicz, Wilson, & Bindshadler (1992). It is written in FORTRAN and C languages. IMCORR is Unix-based, however Tody Benham wrote a Windows Graphical User Interface for it, which is called VisiCorr (Dowdeswell and Benham 2003).

**CIAS** (Correlation Image Analysis) is a free correlation software written by Kääb & Vollmer (2000) (A. Kääb 2005a). It is able to track motion in two precisely co-registered images. It can work with normalized cross-correlation or orientation correlation implemented. CAIS is developed in IDL and integrated in Exelis ENVI. It is not open source.

**ImGRAFT** is developed at Centre for Ice and Climate, Niels Bohr Institute, at the University of Copenhagen. It is written by Messerli & Grinsted (2014). It is an open source image geo-rectification and feature tracking toolbox for Matlab.

**Cosi-Corr** (Co registration of Optically Sensed Images and Correlation) is written at California Institute of Technology. It is used in many fields, such as co seismic deformation, sand dune migrations, slow landslides and glacier flows (Lucieer, Jong, and Turner 2014; Ayoub, Leprince, and Keene 2009; Leprince, Barbot, et al. 2007). Cosi-Corr is also developed in IDL and integrated in Exelis ENVI.

**MicMac** (Multi Image Matches for Auto Correlation Methods) is French Linux-based open source software package developed by Marc Pierrot-Desseilligny. The matching process has a pyramidal approach and derives a dense point cloud using an energy minimization function and regularization (Pierrot-Deseilligny, Marc and Paparoditis 2006; Rosu et al. 2014; Girod 2012). Much of its documentation is in French. MicMac is capable of carrying out the complete process from the raw UAV data to structure from motion and create a deformation map.

### Algorithms

Vogel et al. (2012) did quantitative measurements of glacier flow over time. They used different optical flow algorithms. Vogel et al. found out that the strength of the local image gradients are important in the algorithms. There is a trade-off between feature matching and interpolation between features. Using traditional remote sensing, sub-pixel detection is important. The spatial resolution can be bigger than the actual measured deformation (Debella-Gilo and Kääb 2011). Six algorithms are evaluated by Heid & Kääb (2012). They conclude that cross-correlation on orientation images and software plug in Cosi-Corr outperform all other algorithms. Rosu et al. (2014) experimented with three sub-pixel correlators, Cosi-Corr, MicMac and Medicis. They measured ground displacement by seismotectonic events and conclude that Cosi-Corr works great with very large correlation windows, although it has not many parameters for the user to choose from. According to them MicMac appears to be less vulnerable to noise.

All packages have been briefly tested on a small part of the glacier. ImGRAFT gave good first results and it should be further investigated in a future research. It is point feature-based and therefore the produced map does not contain continuous data. This makes it fast but data need to be interpolated to have a complete coverage. CIAS is not available in the IDL command line and cannot be implemented in a model. Mic-mac and IMCORR are difficult to install because there are non-Windows programs. The first tests of Cosi-Corr gave very good results. Heid & Kääb (2012) already pointed out that Cosi-Corr and its cross-correlation algorithms can be used in glaciology. Cosi-Corr's IDL environment allows modelling the full process. This reduces the actions of the user, especially when settings need to be re-run. To narrow down this research Cosi-Corr is the only correlator that will be used in this research.

### Computations

All calculations are done on a Personal Computer with an Intel processor I5 4590 quad-core 3.3GHz, RAM 8GB DDR3-12800 and a Radeon graphical card R9 270 2GB. Typical processing times where 12 min for a Frequency correlation (F) W128 (initial Window) F62 (Final window), 27 min for

FC with W256 F128 and 144 min for a FC with W512 F128 run, with step sizes of 16px with a 20cm ortho-mosaic input.

### 2.3. Unmanned Aerial System

Unmanned Aerial Vehicles (UAV) are used in remote sensing in many fields ([Niethammer et al. 2012](#); [Hatson, de Roeck, and Ducheyne, n.d.](#); [Mancini et al. 2013](#); [Lucieer, Jong, and Turner 2014](#); [Zarco-Tejada, González-Dugo, and Berni 2012](#)), but are yet quite uncommon in glaciology ([Whitehead, Moorman, and Hugenholtz 2013](#); [W. W. Immerzeel et al. 2014](#)). UAV flights are relative cheap compared to traditional remote sensing acquisitions. Space-borne images are expensive and air-borne flights above the Himalayas are difficult. Air-borne flights are also expensive, due to the altitudes and extreme weather conditions. Receiving traditional remote sensing imagery may take a long time and weather conditions can make fly-overs useless. UAV can be used on-demand and can operate underneath cloud covers. However, many lighter UAVs are very sensitive to wind and light conditions. Unmanned aerial systems may be the bridge over the gap between terrestrial observations and traditional remote sensing.

UAVs can provide ultra-high resolution images. Spatial resolution depends on on operation height of the flight and typically varies between 1 and 20cm. It is able to create ortho-photographs and elevation models. The images have an overlap and can be stitched together and allow a DEM to be created using the principles of stereo-photogrammetry ([Lucieer, Jong, and Turner 2014](#)).

UAVs proved themselves to be useful in landslide mapping ([Niethammer et al. 2012](#)). [Lucieer et al. \(2014\)](#) used Codi-Corr semi-automatic and successfully captured the displacement, but they encountered problems with retreating of the main scarp. Therefore, some extra attention should be given to the glacial ice cliffs in this study. Scarps and ice cliffs show a similar movement in the opposite direction of the main flow. [Lucieer et al. \(2014\)](#) evaluated different types of input data. They used a UAV to create multi-temporal DEMs from the Structure from Motion process and Multi-View Stereopsis workflow was used. Their optical resolution was 1 cm with a horizontal RMSE of 7.4 cm and vertical RMSE 6.2 cm ([Lucieer, Jong, and Turner 2014](#)).

[Immerzeel, et al. \(2014\)](#) were the first to use a UAV to monitor glacier dynamics in the Himalayas. They used the two datasets of 2013 used in this research. They worked in a combined team of researchers from the International Centre for Integrated Mountain Development (ICIMOD), the federal technical institute of Zurich ETH Switzerland and the Utrecht University. They manually tracked a small amount of objects based on visual inspection.

[Whitehead et al. \(2013\)](#) also used UAVs and photogrammetry for glaciological measurements. They studied the Fountain Glacier in Antarctica and created a 1 m resolution DEM and a 0.1 m ortho with aerial triangulation. [Whitehead et al.](#) also tracked glacial flow by hand, but compared it with a SAR interferometry and found that the velocities are within  $0.5 \text{ m a}^{-1}$  of each other.



### 3. Study Area

The study area of this research is the lower part of the Lirung glacier, which is positioned 100 km north of Kathmandu in the Langtang National Park, Nepal. The Langtang catchment is about 360 km<sup>2</sup> and is located on the Main Central Thrust zone in the Himalaya mountain range. The National park has been under constant hydro-meteorological and glaciological observation since 1981. The Lirung debris-covered glacier is located west in the Langtang catchment as shown in Figure 11. The glacier used to be tribute to the main Langtang glacier.

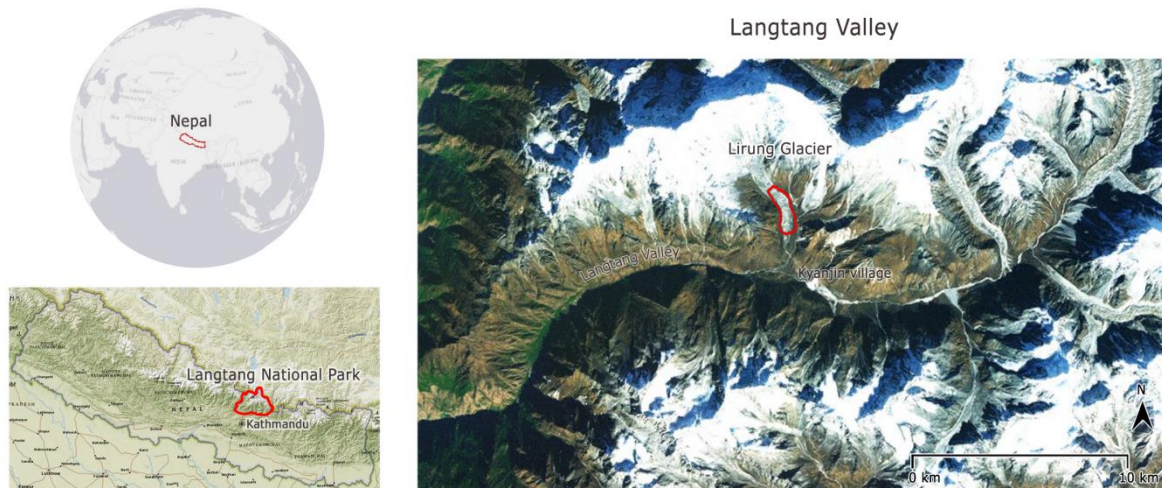


Figure 11 The study area is located in Langtang National Park, Nepal. The study area is outlined with red in the right satellite image.

The accumulation area of the Lirung glacier spreads on the steep slope of Langtang Lirung. This mountain summits at 7227 metre above sea level (MASL). The ablation area is disconnected from the accumulation area by a steep rock cliff that is free of ice. Only snow avalanches and direct snowfall feed the glacier.

The elevation of the ablation area is between 4000 and 4400 MASL, but the maximum elevation of the study area is 4200 MASL due to inaccessibility. The accumulation area of the glacier is covered by debris with a thickness from 0.5 meters near the top to about 3 meters near the terminus. The length of the ablation area is approximately 3500 m.

The thickness of the ice was  $157 \pm 10$  m near upper limit of the study area used in this research and  $20 \text{ m} \pm 5 \text{ m}$  near the terminus in the year of 1999 (Gades et al. 2000). Naito et al. (1998) estimated the thickness respectively more than 100 m and 50 m in 1996. However, they estimated the ice thickness based on flow measurements, while Gades used radio echo-sounding techniques.

Dynamics of debris-covered glaciers are quite unstudied due to the traditional monitoring methods. For this research, the Lirung glacier is chosen to study the effects of debris-covers and its glacier dynamics, like down wasting and stagnant terminus. The relative easy access to the glacier from the nearby village is also a advantage.

### 3.1. Climate

The Indian monsoon is the most prominent event in the Langtang catchment. There is a large number of precipitation days during this period from June to August. During the monsoon approximately 77% of the annual precipitation falls and precipitation occurs almost daily, as shown in Figure 12 (W. Immerzeel et al. 2014; Fountain, Nakao, and Raymond 2000). On average the Langtang catchment receives  $814 \text{ mm a}^{-1}$  of precipitation (Uppala et al. 2005), but in general the daily amount does not exceed  $20 \text{ mm d}^{-1}$  (Walter W. Immerzeel et al. 2012).

Precipitation occurs on only a few days in the dry season, running from November to May. This is caused by occasional winter westerlies troughs passing by. The intensities of those events are high and result mainly in snow.

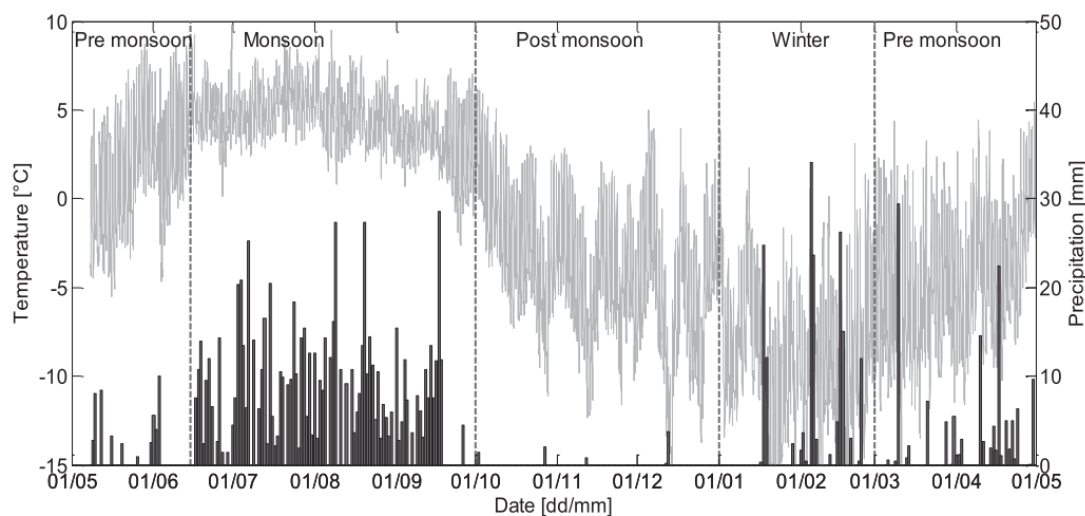


Figure 12, Daily precipitation bars in black. Hourly temperatures are in grey lines at a pluviometer at 1406 MASL. 68% to 89% of the rainfall occurs during the monsoon. Data from 8 May 2012 to 1 May 2013 (W. Immerzeel et al. 2014)

Temperature is strongly correlated with elevation (Sakai, Fujita, and Kubota 2004). As shown in Figure 13, the temperatures at the Langtang catchment can decrease by elevation from  $-0.0046 \text{ }^{\circ}\text{C m}^{-1}$  during the monsoon to  $-0.0064 \text{ }^{\circ}\text{C m}^{-1}$  during the pre-monsoon season. For the non-monsoon seasons (October to June) the mean daily air temperature is  $0.5 \text{ }^{\circ}\text{C}$  averaged over a period from 1957 to 2002 (Uppala et al. 2005). However, the daily average temperature of the surface at the Lirung glacier reaches  $20 \text{ }^{\circ}\text{C}$  (Sakai et al. 1997) and depends on several conditions such as debris thickness, humidity and wind. As shown in Figure 12 the temperature at the Lirung glacier (+4000 MASL) during the summer does not reach below freezing point, while in winter the temperature does not exceed melting point.



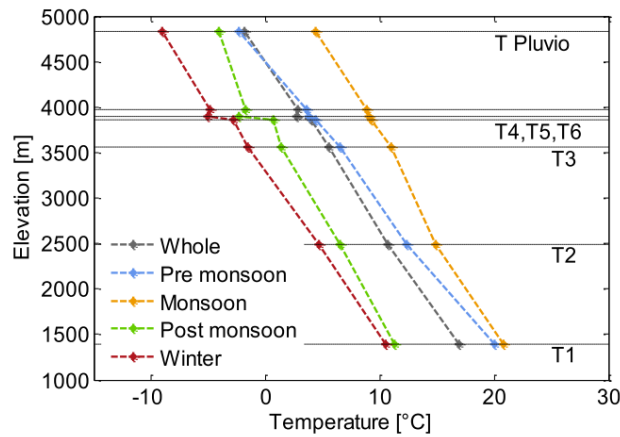


Figure 13 Mean daily temperature plotted against elevation for seven locations and four seasons from 8 May 2012 to 1 May 2013 in the Langtang catchment (W. Immerzeel et al. 2014).

The discharge in glacial rivers is at maximum in the summer season, June to September, because precipitation is mainly rainfall and glacier and snowmelt takes place. During the winter, the discharge is at minimum and mainly consists of a constant base flow. The air temperature is generally below freezing and melting does not occur. The inflow of the rain water or melt water is negligible during winters (Sakai et al. 1997).

Immerzeel et al. (W. Immerzeel et al. 2010) conclude that the rivers of the HKH region are seasonal rivers. Melting of glaciers and snow occur generally during the rain season. Future decrease in the amount of melt water will partially compensated for by an increase in precipitation (W. Immerzeel et al. 2010). However, in some rivers the input of glacier water into summer river flow could be as high as 70-80 per cent (Zemp 2007). With natural and human-related droughts, melt water might be essential for nature and people living downstream.

The Lirung glacier is the region of interest in this research. The melt water of this glacier flows in the Langtang Khola Rivier to the nearby Trisuli River. This river ends up in the Narayani/Gandaki (Nepal/India), which flows to Ganges and eventually in the Bay of Bengal. The water passes one of the most densely populated areas in the world such as northern India and Bangladesh.

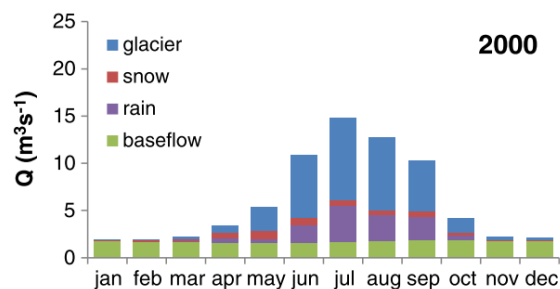


Figure 14, Multi Model Average (MMA) outcome of the research done by Immerzeel et al. (2011). Base flow is the most important factor in the winter months. During the summer, rainfall and even more glacial flow together can account for more than 85% of the total discharge.

The Lirung glacier is most likely a temperate, warm-based glacier ([Walter W. Immerzeel et al. 2012](#)). This is concluded from its location in south eastern part of the Himalayas, its morphological characteristics, the wet climate and it has a monsoon season. Therefore, both basal sliding and internal deformation play a role in surface motion. The top of the glacier flows, while the terminus is stagnant ([W. W. Immerzeel et al. 2014](#)).

Maximum ablation  $10 \text{ cm day}^{-1}$  would occur with a debris thickness of 2.5 cm at the Lirung glacier. On average the Lirung glacier has a cover that is thicker than 0,5 m and thus has an insulating effect. The dust on the Lirung have albedo values between 0.15-0.22, which is substantially lower than the 0.39 albedo of bare ice ([Adhikary S., M. Nakawo, K. Seko 2000](#)).

## 4. Method

---

Remote Sensing can be used to measure surface displacement velocities on the glacier. However, a UAV is used due to the weather conditions and budget. Three UAV image datasets are available with a timespan over 1 year. Comparing these datasets will provide insight in the surface dynamics of glaciers and their flow velocity. The manually tracking of the images is laborious and time consuming. Algorithms for automatic motion tracking will be applied.

In this chapter, the data acquisition and processes from raw images to surface displacements are explained. The first subchapter described the used UAV and flight data, followed by the Structure from Motion workflow.

Raw data from the three UAV flights have been processed into DEMs and ortho-mosaics. Different types of input data are compared, such as slopes, ortho-mosaics and hillshades. The best data type will be used in further research in spatial resolutions and correlation assessments.

A visual measured ground-truth matrix is created, in order to check the quality of the modelled output of Cosi-Corr. This matrix consists of approximately 500 random points that are measured by hand. The input data of both the manually and automated correlations are the same maps. Therefore, the error of the input data can be neglected when comparing the two methods.

### 4.1. Fieldwork

#### 4.1.1. Data acquisition

There are three datasets used in this study: May 2013 (in del coded as: A), October 2013 (B), May 2014 (C) and. The flights that are taken in May are pre-monsoon flights, the one in October is post-monsoon and around the end of the melting season. The end-of-summer snow line corresponds to the equilibrium-line altitude because the snow did not melted away above this line and the snow is situated in the accumulation zone. The snow that was below this line melted away and thus located in the ablation zone. There was no snow visible in the photos. This indicates that covered part of the glacier is the ablation zone.

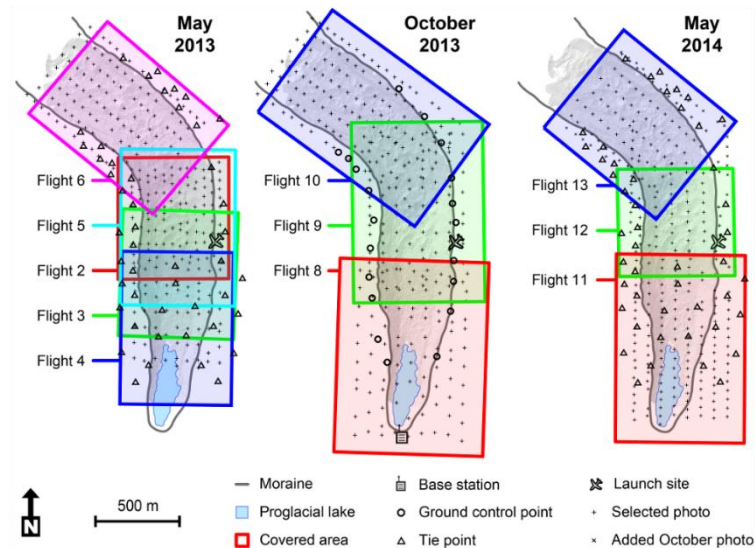


Figure 15, Overview of the three survey periods based on the 13 UAV flights with their approximate covered area, positions of the gathered images selected for processing, locations of the ground control points (GCP) and locations of the tie points (W. W. Immerzeel et al. 2014).

The flights were scheduled in the mornings to maximize flight stability, image quality and to have the same orientation of shadows. In the mornings, the wind is at minimum strength due to the turning point of the diurnal valley circulations. All of the UAV flights were launched from a boulder on the ridge of the eastern lateral moraine. The autopilot performed circular auto-landings on a nearby flat terrain. For all the flights, the images had a 70% overlap in flight direction and 60% in perpendicular to flight direction.

#### 4.1.2. Operational UAV

For this study the unmanned aerial vehicle Swinglet CAM and the eBee from SenseFly are used (SenseFly 2014). The cruise speed of the Swinglet is at  $10 \text{ m s}^{-1}$  and the battery can last for for approximately 30 minutes flights. The controls can be handled manually, however the autopilot is used. The UAV flies on waypoints with a pre-programmed flight path. The eMotion software helps



with setting up a flight plan and calculates at which points photos need to be taken. There is a radio connection between the computer and the Swinglet. This allows having inflight information monitoring and adjustments. The UAV has multiple onboard sensors. It has a wind meter that is used for flight corrections. The GPS receive keep track of its exact location that is used for flight control and it speeds up further image processing. The altimeter information is needed to calculate the DEM.

Figure 16, Swinglet CAM unmanned aerial vehicle of SensFly used for remote sensing, it create a spatial resolution of 3cm (SenseFly 2014).

On board a Canon IXUS 125 HS is mounted. The 16 megapixel (4608 x 3456 pixels) captures JPEGs. The camera's focal length was wide-angled 4.3 mm (24 mm equivalent) and has some barrel distortion. Wide open has the camera an aperture of F/3.2. The Dynamic Range of this camera is 9.5 EV at ISO100, which is quite high. (Techradar 2014). Signal to Noise Ratio for this camera is for a ISO100 39 dB, which is excellent image quality (Mazzetta, Claude, and Wageneck 2005). In the datasets used in this study the ISO values range between 125 and 250 and the shutter speeds between 1/320 and 1/1200s. The change in ISO causes some quality differences between the images, but is not significant. The images are sharper near the centres and it decreases near the corners.

## 4.2. UAV-based Structure from Motion process

Stereo-photometry is a major advantage of UAV flights. The overlap between multiple photographs can be used to determine a Digital Elevation model. These calculations are based on the Structure from Motion principle.

### 4.2.1. Mosaic image

Most sensors in traditional remote sensing are recording imagery by using a swap method. Such sensors scan a short line and after the vehicle moves, further it records a new line. The sensor repeat this process for every line of pixels, it shows similarities to an office scanner. Every line is saved into one long image. In theory, this image has only a fixed width due to the sensor, but there is no limit on how many lines it can combine in one image. This process creates long images that are called swaps.

Many UAVs use non-professional cameras that take one fixed size photograph. In theory, such cameras also work with curtain line-for-line capturing. However, the daily-use cameras in the UAV have fixed number of lines, because for every line another part of the sensor is used. In flights with non-professional remote sensing sensors multiple image are taken of the region of interest. For remote sensing it is necessary to combine images, e.g. for comparing images, in geo-references and during ortho-rectification. Images are stitched together based on the Structure from Motion workflow that uses feature tracers. The output is one large image that is called a mosaic-image.

Mosaic images are multiple combined photographs. Between two photographs should be at least 60% overlap and the same traceable features (Lemmens 2011). Images can be stitched together based on these features, called tie-points. A tie point is a feature, e.g. rocks, boulders, edges, man-made feature or anything that is clearly visible on both images. With a minimum of four tie points, a stitch can be made. Four tie points of one image are positioned over the four corresponding tie point in another image.

In flight dynamics, there are 6 degrees of freedom: forward/backward, up/down, left/right, pitch, yaw and roll. Movement in any degree of freedom result in different ground coverage in every photograph. Together with lens distortion, a spatial transformation is needed to compensate for

any optical errors. An affine transformation is possible, but a second order polynomial transformation is used in many cases due to distortion of the lens.

#### 4.2.2. Rectification

Coordinate systems are essential in communication and comparing data. Raw sensor images do not have information about the real-world coordinates and need to be linked to imagery. This is done by field-measured coordinates by dGPS. These points can be found in the image. The right coordinates can be linked to every pixel in the image by a second order polynomial transformation. This process is called geo-rectification.

Some satellites do have a geo-location accuracy of 3 meter, such as Worldview-4 (Cnes 2013). This means that a pixel has the right real-world coordinates with 90% change with 3 m accuracy. This accuracy is however not enough for glaciology research. The UAV used in this research has very poor geo-location accuracy because the vehicle is not stable and low on-board GPS accuracy.

Ortho-rectification is a process that correct for the elevation distortion. Every non-nadir pixel has a false coordinate location in the image. Ground Control Points (GCP) could correct for this incorrect projection, but need interpolation in between the GCPs. The gradient of the terrain (slope) can be large and vary locally. Interpolation is not possible in such terrain, because the values in between the CGP are changing. Every pixel should have its own GCP. The ortho-rectify workflow adjusts pixels with an elevation model. The false projection in imagery by relief can be corrected by an underlying DEM as shown in Figure 17.

There are fundamental differences between UAV and traditional photogrammetry. Firstly, UAVs do not have exact Exterior and Interior Orientation information. In traditional photogrammetry Bundle Block Adjustment (BBA) are used to solve the exterior orientation of each photograph. The Exterior Orientation (EO) of a camera is the camera position and orientation, which are unknown or limited accurate in UAVs. The Interior Orientation (IO) of the camera is based on focal length principle point and lens distortion. The EO and IO are used for geo-locate the sensor and the exact coverage of the imagery. Secondly, UAVs have large rotational and angular variations between images. This can be partly solved with tie-points when merging photographs. Together with the relative low flight elevation to the local elevations, this can create local distortion in the final mosaic image. Thirdly, UAVs have high variability in illumination, occlusions and different spatial resolutions.

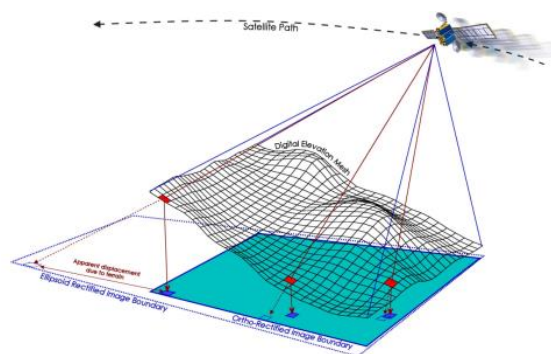


Figure 17, Raw imagery need to be corrected for local relief. A digital elevation model is used to estimate the correct location of a pixel. This process is called ortho-rectification.

All of these UAV problems are mainly caused by flight instability, but can be reduced by a large amount of tie-points that occur in multiple photos. For this reason, photographs should have a 70% overlap in flight direction and 60% in perpendicular to flight direction. Some of the tie-points can occur in nine different photographs, to lower the errors within the photos. With automated tie-point detection more observations for BBA can be generated and thus improving the accuracy of the results (Turner, Lucieer, and Watson 2012; Plets 2012).

#### 4.2.3. *Structure from Motion*

Structure from Motion (SfM) is a range imaging technique. It recovers a 3D scene from 2D projected images in stereo vision. Structure from Motion uses feature-tracking algorithms to detect and trace features within each image. Two or more overlapping images from a multi-view perspective contain information about epipolar geometry. A BBA is applied to these features to estimate the EO and IO of each camera plane and based on this information the distance to the features can be calculated. The output of the structure from motion workflow is a sparse 3D cloud.

The program used for the SfM in this study is Arcsoft and it uses the SIFT (Scale Invariant Feature Transform) feature tracker. SIFT is a region detector and is robustness against changes in rotation, scale, affine distortion and partial illumination changes. It is a popular feature detector in Computer Vision and due to its robustness SIFT is applicable on UAV data (Lucieer, Jong, and Turner 2014).

A more denser point cloud of terrain points is calculated using MVS (Multi-View Stereo) techniques from three or more images (Campbell et al. 2008). This cloud is often retextured by the original photographs for 3D orthographical mosaics or every pixel is given an elevation value to compute a DEM.

### 4.3. Auto Cross-Correlations by Cosi-Corr

A way to calculate the surface displacements is to tracked debris by hand (W. W. Immerzeel et al. 2014). This process is very time consuming. The software Cosi-Corr can process large high-resolution imagery to track debris on a high spatial scale. It uses automated cross-correlations to determine the displacement.

#### 4.3.1. *Cosi-Corr software*

Cosi-Corr was originally written for studying tectonics, but it is proven to be useful for displacement monitoring in glaciology (Heid and Kääb 2012). The first to use Cosi-Corr in glaciology was Scherler et al. (2008). They monitored the Khumbu glacier in Nepal, which is very similar to the Lirung glacier. The glaciology research with Cosi-Corr continued (Scherler, Bookhagen, and Strecker 2011; Quincey and Glasser 2009).

The code of Cosi-Corr is not open-source. It is a plugin inside Envi and a new window opens where input files are required. That makes it difficult to tweak the process or to automate the process. A complete model with pre and post processing is written in Envis IDL for this thesis. There is only one way to call Cosi-Corr in Envis IDL. It is the batch command:

```
IDL> cosi batch correlation, master.txt, slave.txt, CORR=correlation.txt, OUT=output.txt
```

The batch command is used for running multiple inputs all at once. It requires four files with information about the master-file location, slave-file location, correlation and the output location and name. Cosi-Corr outputs a file that comes with three different channels. Channel 1 is a flow field North to South (NtoS). The pixel value indicates the displacement in southern direction. This is projected in the master-file. The second channel is a similar layer with East to West (EtoW) displacement. Both EtoW and NtoS layers form the x- and y-component of a vector. This can be calculated with the Pythagorean triples. The third channel is a Signal to Noise Ratio (SNR). This layer quantifies the quality of the correlation and ranges from zero. In this range means zero there is no correlation and one means a perfect correlation (Leprince, Barbot, et al. 2007). This layer could work as a quality mask for the EtoW and NtoS layers.

Cosi-Corr has two correlators with different principles. One is a statistic correlator and the other a frequency based correlator.

#### Statistic correlation

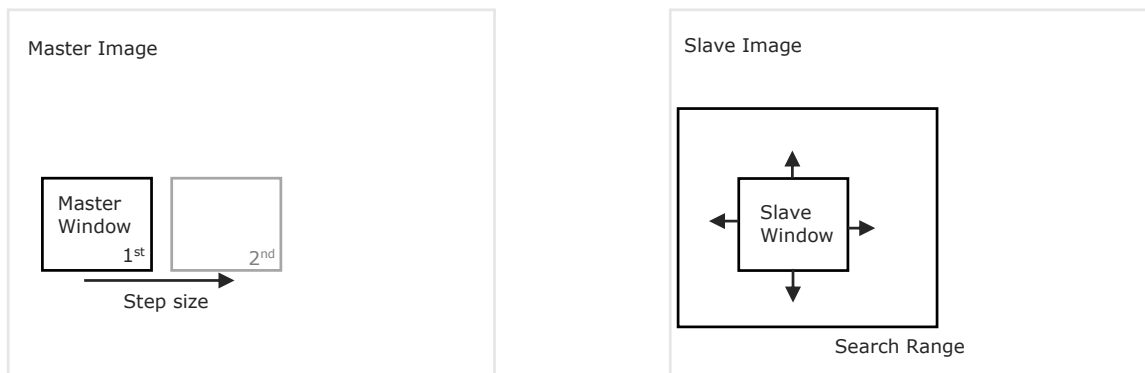


Figure 18, Statistic correlation method compares correlation coefficients from the master window and a corresponding slave window. This occurs within a search range in the slave image. The position of the next window is determined by the step-size.

The statistical correlator of Cosi-Corr is based on a window in the master image that computes correlation coefficients with a corresponding moving window in a slave image. The correlator maximizes the absolute values of the correlation coefficients. This technique is robust, but coarse compared to the other frequency correlator. The statistic correlator is recommended for correlating image that have optical noise. It can also be used for correlating two different type of data, such as a hillshade together with an ortho-mosaic (Ayoub, Leprince, and Keene 2009). The master thesis by Yaseen (2009) investigates the parameters of Cosi-Corr at the International Institute for Geo-Information Science and Earth Observation. He concludes that Cosi-Corr's frequency correlator gave the best results and for accuracy of displacement estimation, a flat non-moving area should be selected.

#### Frequency correlation

The frequency correlator of Cosis-Corr is a two-step process that is Fourier based. The first step roughly estimates the displacement on pixel level, while the second smaller window estimates the sub-pixel displacement. It is more precise than the statistic correlator is, but the frequency correlator is more sensitive to noise. It uses a 2D Fast Fourier Transformation (FFT) to correlate windows in the frequency domain. The correlation is based on the phase difference of the two windows, where it finds the maximum of the cross correlation. It is weighted by a bell-shaped window, so it centre-weight the matching. This makes the correlator more certain where the match actually comes from within the window. However, it can still correlate in areas that are outside the centre when there is low contrast. The frequency correlator uses a mask to threshold the amplitude of the log-spectrum to reduce noise.

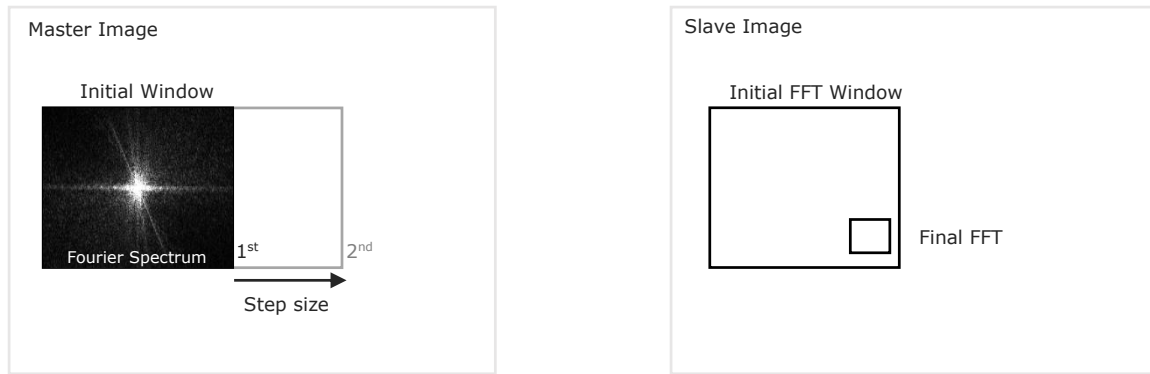


Figure 19, Frequency correlator is a two-step process. It calculates 2D Fast Fourier Transformation (FFT) from both the initial windows in the master and slave windows. It results in a displacement on pixel scale. The second step is the same process with a smaller window for sub-pixel detection.

#### Discrete Fourier Transform

An image is a two dimensional spatial signal and can be seen as a function  $f(x,y)$ . A Discrete Fourier Transformation (DFT) represents this image as the weighted sum of basis 2D sinusoidal functions. This results in a 2D spectrum  $F(u,v)$  of spatial frequencies. A DFT takes discrete numbers (pixels) and convert them into frequency log-spectrum. A simple Fourier series is based on a periodic function in a discrete spectrum with fixed dimensions, a raster image, the number of samples is known. Images are almost never complete non-periodic functions. A Fourier Transform (FT) solves this with non-periodic functions that approach infinity. The DFT can be written as (Heideman, Johnson, and Burrus 1985)

$$F(n) = \sum_{n=0}^{N-1} f(n)e^{i2\pi k \frac{n}{N}} \quad (4)$$

For  $n = 0,1$  and  $N - 1$  as sampling rate.  $N$  is the size of the window and  $n$  represents the center of a pixel. This equation is based on Euler's formula:

$$e^{i\theta} = \cos(\theta) + i \sin(\theta) \quad (5)$$

The  $e^{-ik\pi}$  is a representation of cosines and complex sinus functions with  $k$  as wave number. The original pixel value  $f(n)$  is multiplied by a cosine and a sine, which is a cross-correlator.



## Fast Fourier Transform

Fast Fourier Transformations (FFT) are efficient algorithms for running Discrete Fourier Transformations (DFT). There are many different FFTs, but the Cooley-Tukey FFT is most used (Stone 1966). It is a re-invented the algorithm that was written by C. Gauss in 1805 (Heideman, Johnson, and Burrus 1985). It computes even and odd  $n$  (pixels) separated, therefore the requirement of this algorithm is that the number of samples  $N$  in the function should be a power of two. It breaks down the signal into smaller pieces and this 'divide and conquer' principle speeds up the transformation. Fast Fourier Transform  $\hat{f}$  that describes function  $f$  towards infinity is defined as:

$$\hat{f}(\omega) = \int_{-\infty}^{\infty} f(n)e^{-i\omega n} dx \quad (6)$$

The results of this equation are sequences in the frequency domain. The frequencies are running from 0 to  $2\pi$ . The  $dx$  is the size of DFT frequency bins and is relative to the sample rate  $n$  from the DFT equation (Thévenaz, Blu, and Unser 2000). Comparing the DFT function  $F(u, v)$  and the original function  $f(x, y)$ , results in a complex number by the correlator and contain the amplitude and phase of every sine.

Every point in the logarithm spectrum represents a sinus wave function based on the amplitude and frequency. According to the Fourier theorem, the sum of these wave functions should approach the original pixel pattern, as shown in Figure 20. In reality, the wave functions can exactly have the same value as a pixel, because only the pixel centre is needed. It is common to shift the lower frequencies in the centre of the graph of two-dimensional DFTs, because of further masking possibilities in imagery. The input function  $F(u, v)$  is built up from pixels and therefore, it should be seen as a rectangular function. The FFT of rectangular function result in normalized sinc function, where  $\text{sinc}(0) = 1$ .

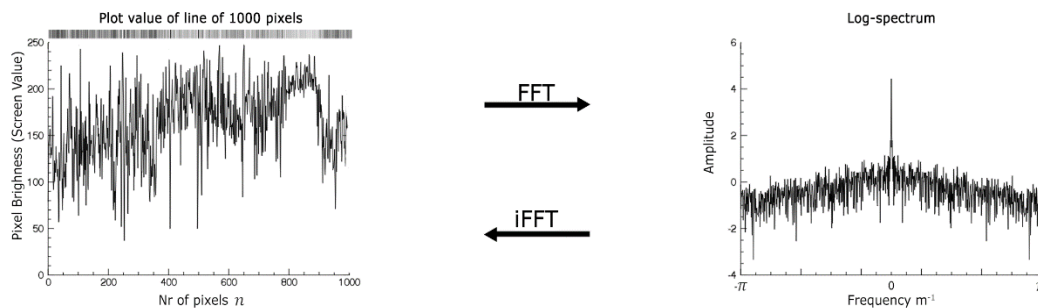


Figure 20, *Left*: The values of a line of pixels from the Lirung glacier is plotted in the left graph. The number of pixels ( $N$ ) is 1000. Frequency bin size is  $2\pi/N$ . *Right*: This computes with a FFT algorithm into a log-spectrum. An inverse FFT (iFFT) compute the original spatial domain.

The FFT output is a complex number and contains a real part and an imagery part. The amplitude is calculated by the Root of the Sum of the Squared (RSS) real and imagery parts. It has a typical peak near low frequencies. The  $F(0)$  sine does not oscillate and determines the average amplitude of  $f(x, y)$ . The corresponding phase spectrum is almost completely a random pattern and computed by the inverse tangent of imaginary part divided by the real part. Cosi-Corr

uses this phase spectrum because it is less influenced by the intensity of the pixel and therefore, different illuminations, such as shadows, are less important.

## 2D Fast Fourier Transform

In [Figure 20](#), a Fast Fourier Transform was computed from one single function, a line consisting of pixels. A FFT computation of a complete two-dimensional image is a two-step process. The first computations are FFTs of every row and followed by the second computations of FFT of every line ([Exelis 2015](#)). This results in a matrix with same resolution as the input image.

The origin of the graph is centred for mask possibilities. There are two types of filters. Firstly, a high pass filter sets the centre amplitude to zero. The high frequencies are filtered out. An inverse FFT of a high pass filter shows only edges. Secondly, a low pass filter results in a blurry image. The inverse FFT image is lacking low frequencies and thus the textures are visible and not the edges. The masking option of the frequency correlator in Codi-Corr is a high frequency filter.

The typical straight cross lines at  $v, u = 0$  are the result of the window edges. The DFT assumes that the window size equals to one period. The result of this assumption is that the image is repeating itself infinitely in both x and y directions.

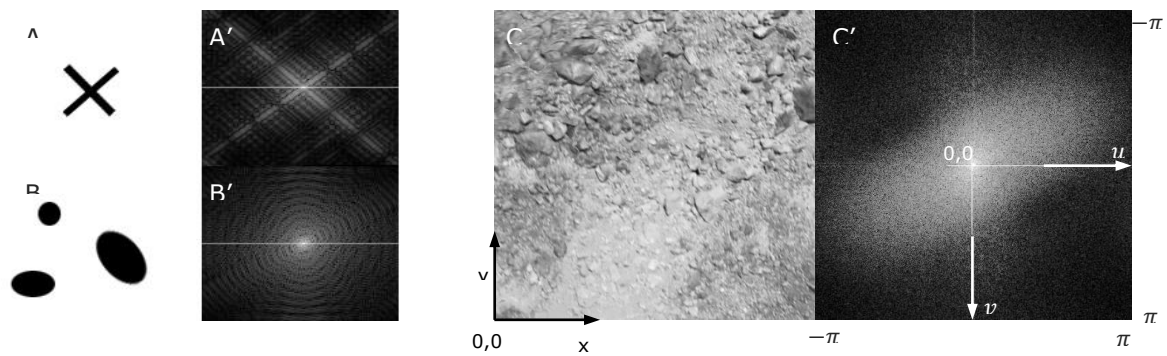


Figure 21, *Left*: Simplified 2D functions with the corresponding FFT log-spectra (') of a cross (A) and simplified rocks (B). The log spectra have unique patterns, based on edges. *Right*: A square window (128px) from the Lirung Glacier (C) is shown with its corresponding log-spectrum (C').

Codi-Corr does use the principle of a 2D FFT, but does not combine it into an image. It uses one FFT to compute the displacement per line an East to West shift (EtoW). The maximum correlation coefficient determines the displacement. Another series of FFT transformations is done per row in both images results in a North to South (NtoS) displacement ([Leprince, Avouac, et al. 2007](#)). This speeds up the process, but is vulnerable for noise image with repetitive patterns.

## Cross - Correlation

Inside the DFT function is a basic cross-correlator located. A correlator measures similarities between functions. In other words, it measures how present one function is in another. In the case of DFT the correlator tests the presence of every new sine in the function Fourier function  $F(n)$  in the original function  $f(n)$ . The simplified equation of a cross correlator is:

$$Corr_{F,f} = \sum_{n=0}^{N-1} F(n) f(n) \quad (7)$$

It is a basic multiply and accumulation process and results in a correlation coefficient. To find the most corresponding sine to the function  $f$ , the  $F(n)$  function shifts in a  $n$  step relative to function  $f$ . Every shift has its own correlation coefficient. The maximum of the correlation coefficient determines the best correlation. This is only possible when the both functions have roughly the same order of values. The normalized cross correlation solves this problem:

$$Corr\_norm_{x,y} = \frac{\sum_{n=0}^{N-1} \hat{f}(n) \hat{f}'(n)}{\sqrt{\sum_{n=0}^{N-1} \hat{f}(n)^2 \sum_{n=0}^{N-1} \hat{f}'(n)^2}} \quad (8)$$

In this equation example, the Fourier sequence of one master image  $\hat{f}$  is correlated with the Fourier sequence of the second slave image  $\hat{f}'$ . The sequences are shifted in  $n$  steps along each other to find the correlating shift. The  $n$  determine the displacement and the accuracy.

Cross-correlations are used in FFT, but they are also used to correlate one Fourier domain with another. Cosi-Corr uses a Gaussian function during the correlation the two sequences. This weights the centre more. This results in a correlation that is more edge-based. This effect can be increased by using a binary mask image that filters out the high frequencies.

#### 4.3.2. Artificial Displacement

A technique which has been used by Rosu et al. (2014) is to create an artificial displacement, to test for background noise of Cosi-Corr. A map with artificial displacement is created and correlated, see Figure 22. The velocities are increasing from zero to 70 m a<sup>-1</sup> in seven equal steps. The frequency correlator has been used with an initial window size of 128px and a final window size of 64px. An extra zone is added at the right hand side to test for extreme velocities.

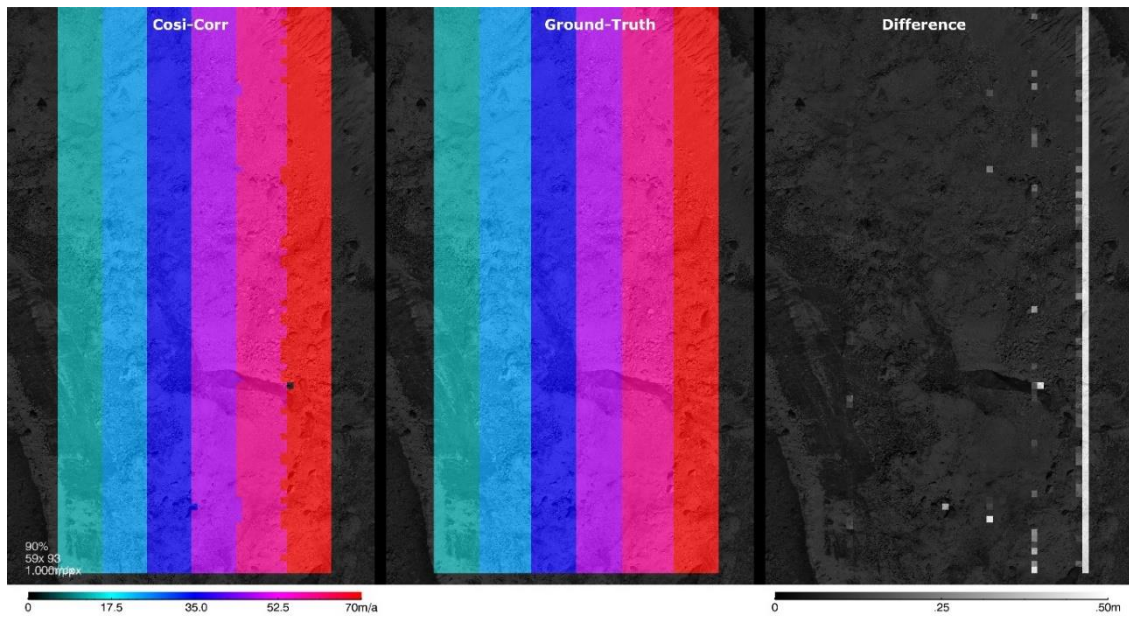


Figure 22, Left: Cosi-Corr's automated correlation of an artificial displaced section of the Lirung glacier. Mid: the manually correlated map. Right: Difference map between the manually and the automated correlation maps. A mismatch can be found around the edge of the high velocity and areas with no displacement. F W128 F64 S16

In [Figure 22](#) the east to west artificial displacement is shown. Both east-to-west and north-to-south direction are modelled, but they do not show different behaviour. The correlation results have clear borders between displacements, but Cosi-Corr contains some noise. Especially near the border between high displacement and no displacement. However, such clear borders are unlikely occurring at surface displacement of glaciers. This test indicates that Cosi-Corr is correlating fine with the Lirung ortho-mosaics and can correlate great displacements up to 70 m/a.

#### 4.3.3. Data

In this study, different kinds of input data are assessed. Three optical based derivations (brightness, Laplacian Enriched Brightness and Principle component) and three DEM based (slope aspect and shade) relief will be correlated. Finally, different spatial resolutions will be examined.

##### Input Data

The Cosi-Corr's algorithm cannot handle multi-channel image, like the RGB imagery shot by a UAV. This data should be transformed in a grey scale image. The ortho-mosaics can be computed in to brightness image. The brightness is based on the sum of the ratios of the RGB bans.

$$\text{Brightness} = 0.2126 * \text{band1} + 0.7152 * \text{band3} + 0.0722 * \text{band3} \quad (9)$$

The Laplacian enriched brightness image is based on the brightness equation, but it uses a Laplacian operator over an image that enlarges contrast-rich edges. Multiplying the Laplacian image with the original image improve sharpness and increases the contrast in edges.

The Principle Component analysis (PC) is based on the principle that some of the bands have often the same information about an object. A PC analysis is used to remove the correlations among bands to create a new band with non-correlation information. The variation of pixel values is identified based on the optimum linear combination of bands. ([Lim, Sohn, and Lee 2001](#)).

Three derivations of the ortho based imagery:

- Brightness
- Laplacian enriched brightness
- Principle Component 1

The Structure from Motion process created an ortho-mosaic image and a Digital Elevation Model (DEM). The DEM itself is not suitable for correlations because it has almost no textures. Products derived from a DEM like slope, aspect and hillshade do have textures. In the DEM derivatives, the 'surface' the glacier is computed and has therefore no optical noise. In theory, this is an advantage over the ortho-mosaic, which contain blur, shadow and grain noise. However, the DEM is based on Structure from Motion and this process encountered the noise in the prior computation stage. The slope is based on the local slope, so the edges of boulders and ice cliffs are highlighted. A shaded relief or hillshade is an original DEM with artificial shadows. The aspect image is colourized by compass points.

Three derivations of the DEM based imagery:

- Slope
- Hillshade/ Shade Relief
- Aspect

The influence of spatial resolutions is assessed. The original ortho-mosaics have a pixel size of 10cm. A second model is used as plugin to produce to create different spatial resolutions. The interpolation is based on a cubic convolution interpolation method. It closely approximates the theoretically optimum sinc of the interpolation function using cubic polynomials. ([Reichenbach and Geng 2003](#); [Exelis 2015](#))

The six different spatial resolutions that are tested:

- 10 , 20, 35, 50, 100 and 200 cm

#### 4.3.4. *Ground-Truth*

To test the capabilities of Cosi-Corr, a ground-truth map is created by hand. The errors of the master and slave image are neglected, because both the automated and manually correlated map has the same input error. The manually correlated is created by visually measuring the displacements between the two images. This is done by drawing lines from recognizable features, like boulders and bright rocks.

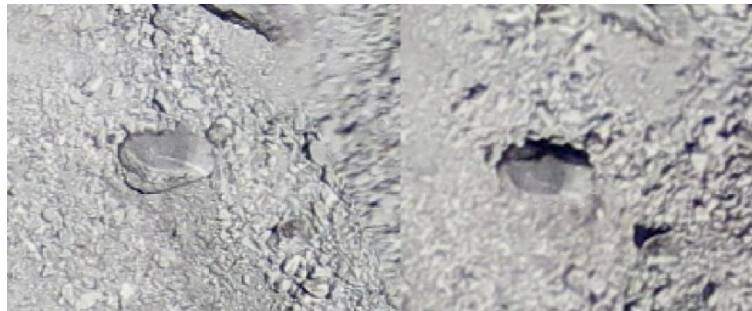


Figure 23, Parallax, shadow and blur lower the correlation of the same boulder. The south and top face are visible in the left image, while the same boulder shows the north and top face in the right image. *Left*: a diagonal edge is visible with motion blur of a mosaic-photo on the right side. *Right*: The whole photo has low image quality. During manually tracking this boulder should be avoided.

For this research, approximately 500 points are drawn randomly to track motion between the imagery of May 2013 (master image) and Oct 2013 (slave). High contrast rich features, like rocks, are tracked from the master image to the slave image. This resulted in vectors that capture the displacement. A North to South (NtoS) and an East to West (EtoW) file are created as output, similar to Cosi-Corr.

As shown in [Figure 23](#), parts of the ortho-mosaic contain blur, different shading and parallaxes. A rock that is blurred is deformed and the edge of the rock is turned into an indistinctive stroke. It is impossible to know the correct location of a blurry edge. The uncertainty can be high as 0.5 m and therefore, features with blur are not taken into the ground-truth map. Tracking a feature that has similar blur in both images could be possible, but this depends on the ortho-rectification. The rectification of a blurry feature is probably different in both images.



Parallax and shading can be problematic for recognizing boulders. A different shade and parallax can change the visual form of a rock. For these reason it is easier to recognize a cluster of rocks rather than single boulders.

#### 4.3.5. Quality assessment

One way to measure the quality of the Cosi-Corr map is to compare the difference between the automated and manually correlated vectors. This can be expressed in magnitude or phase difference and basic statistics can computed.

##### Raster data

Cosi-Corr calculates for every pixel a displacement and therefore the data is consecutive. The output is a complete raster without any gaps. The ground-truth exists of approximately 500 points. These are based on visual inspection between two imagery. The points give a displacement at exact coordinates.

To compare these ground-truth points with the Cosi-Corr raster, a normal kriging interpolation is applied to create a raster ground-truth map. The data in between these points is interpolated to the same dimensions as the automated map has. Every pixel of the manually correlated map can be plotted against the corresponding pixel from the automated correlation map. If the points are scattered around the  $y=x$  line the displacements from Cosi-Corr are in the same order of magnitude as the displacement in the visually correlated map.

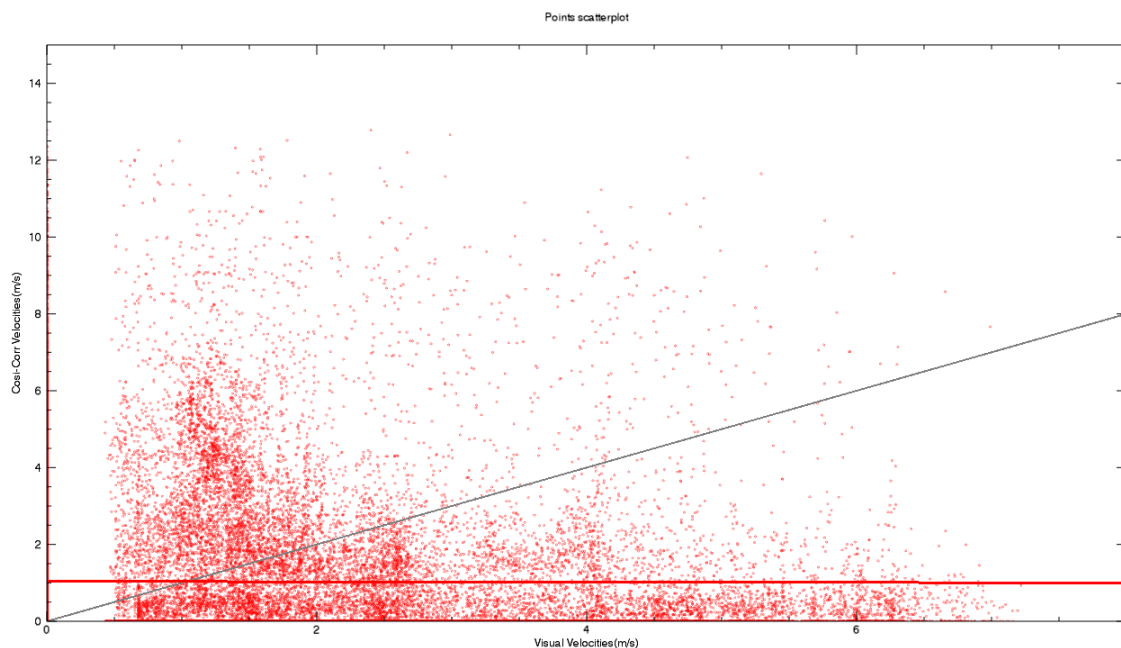


Figure 24, Scatter plot of the Cosi-Corr data on the y-axis against the visual based Ground-Truth data on the x-axis. The grey line is the  $y=x$  line. Red line is the best-fit line of the points. The visual based map has no velocities below 0.5 m/a during the monsoon period. According to this scatterplot, there is a bad correlation between the ground-truth and the Cosi-Corr map.

In Figure 24, the modelled Cosi-Corr values are plotted against the measured ground-truth values, see scatterplot. The measured values have no velocities below 0.5 m/a during the monsoon period. The reason is unknown, however, the lacking velocity is approximately 0.2 m/summer-observation that corresponds to the pixel size used in this example. The statistics of the best-fit

line are very poor. The hypothesis is that the interpolated values do not match the values of Cosi-Corr. A scatterplot with the original ~500 manually tracked points against the corresponding ~500 pixels of Cosi-Corr's correlation has better statistics. An overview of both approaches is visible in Figure 25.

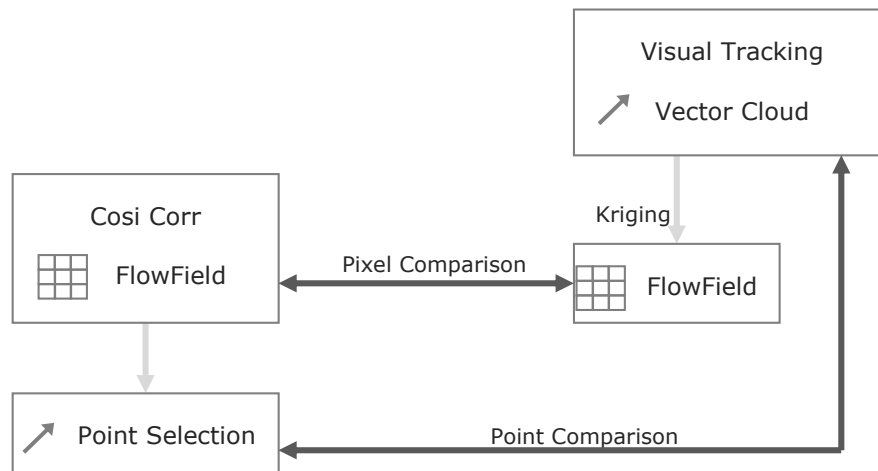


Figure 25, Schematic process flow diagram of two ways to compare modelled raster data with measured point data. One way is to interpolate the point data into a flow field and compare every pixel. This technique introduces estimated data from the interpolation. The second technique is to find the corresponding points of the measured data in the modelled data.

The coordinates of the ground-truth points can be found in the Cosi-Corr raster data. This is done by a bisection method in the model (Exelis 2015). In the data are a few outliers as shown in Figure 26. Two of these outliers have such high values (17 and 29 m/a) that they influence the statistics. Such high velocities are unrealistic on the glacier and therefore they are removed from the dataset. Removing two outliers will not influence the dataset of 500 points. They are caused by wrong correlations by Cosi-Corr and should be considered as noise. They are not interesting in the overall statistics.

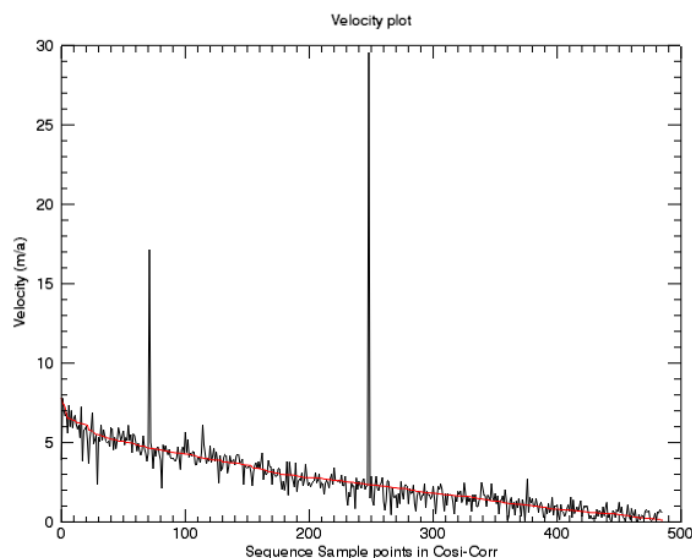


Figure 26, The red line represent the velocities of the visual-correlated points. The trend that is visible is caused by sorting by velocities in Microsoft Excel and has no physical correlations because the points are randomly taken. The black line is the pixels corresponding to the same coordinates as the visual-correlated points. They fluctuate more and have two outliers that are removed for further processing.

Noise can be dominating the signal. For this reason, a kernel could be used so that the corresponding points in Cosis-Corr are area-weighted values, but noise with large values can dominate statistics. A median kernel can correct for noise and outliers as it takes the middle value of the sorted matrix. A kernel with a maximum velocity of 6 m a<sup>-1</sup> can also be used. Tests were done with Gaussian kernel to weight surrounding pixel values. Both median and Gaussian kernel resulted in worse statistics and therefore, these steps are removed from the model.

### Statistics

The scatterplot of the manually tracked points against the corresponding Cosis-Corr points is an indication of the quality of the automated correlation. The coefficient of determination ( $R^2$ ) indicates the spread of the points that are plotted. A  $R^2$  of one indicates all the points are located on a line. The Root Mean Square Error (RMSE) measures the average magnitude of the error. It weights large errors. The RMSE is an indication of the presence of large errors.

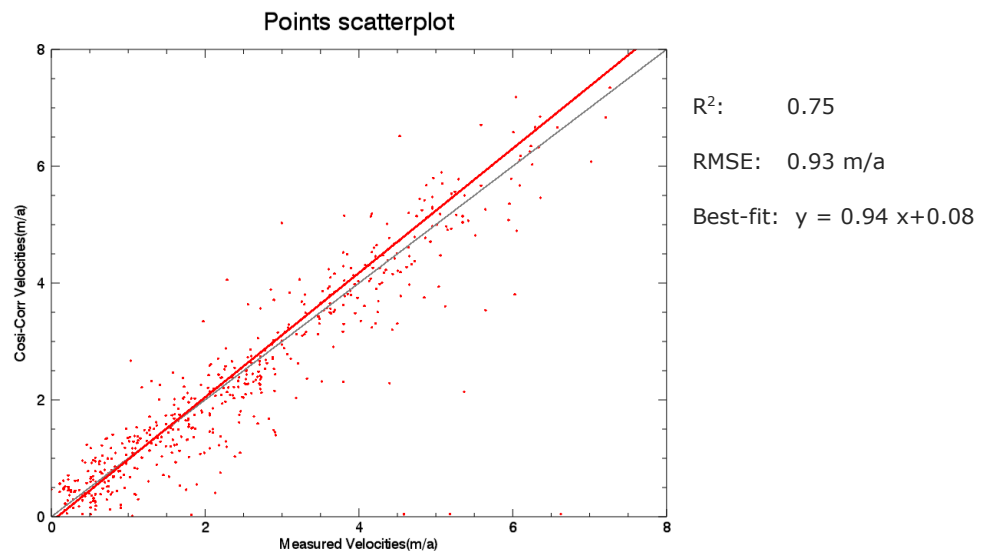


Figure 27, Scatterplot of the visual measured ground-truth points against the corresponding points from the map of Cosis-Corr. This best fit indicates an average overestimation of Cosis-Corr with velocities above 1 m a<sup>-1</sup> and an average underestimation with lower velocities.

Another statistics tool is a best-fit line of the points. The best-fit line should approximate  $y=x$ . In this case, the values of the automated displacement equal the values of the manually tracked points. The best-fit line is representing the trend line in the scatterplot. The slope ( $m$ ) determines the angle of the linear function and thus the ratio of over- and underestimation. It should approximate one. The y-intercept ( $b$ ) should be zero for a perfect correlation.

### Vectors

A projected raster image contains x and y coordinates. The pixel can contain only one value. Vectors have two dimensions ( $dx, dy$ ) and a magnitude. Therefore, a pixel value can either be the velocity in the x-displacement or in the y-displacement. Cosis-Corr uses an image for the North-to-South (NtoS) flow field and thus displacement in y-direction. Another image is used for the East-to-West (EtoW) field that represents the displacement in x-direction. Note that the NtoS field has positive values towards the south. Pythagorean triples can be used to calculate the velocity. A



vector map can be visualized by the NtoS field and EtoW field. Such maps show both velocity and direction.

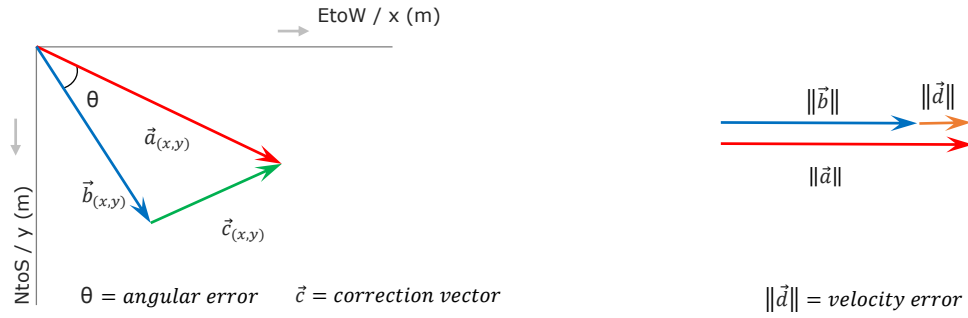


Figure 28, The modelled vector ( $\vec{a}$ ) can be compared to the measured vector ( $\vec{b}$ ). The Angular Error (AE,  $\theta$ ) is the angle between the vectors. The correction vector ( $\vec{c}$ ) is an indication of the incorrect displacement. The Velocity Error (VE,  $\|\vec{a}\|$ ) is the magnitude difference.

Angular Error (AE) is the angle between the measured vector and the modeled vector ( $\theta$ ). It shows the error in direction in degrees. The AE is more sensitive for small ( $\vec{a}$ ) and ( $\vec{b}$ ) vectors. The correction vector ( $\vec{c}$ ) has less impact on vectors that have large magnitude than smaller ones. The tangent of  $\theta$  is based on the cross and dot product of both vectors.

$$\text{TAN}(\theta) = \frac{\|\vec{a} \vec{b}\|}{a b} = \frac{a_x b_y - b_x a_y}{a_x a_y + b_x a_y} \quad (10)$$

An ATAN2 function is needed to cover for negative x values. The normal ATAN function covers only from  $-\pi/2$  to  $\pi/2$  and is therefore not useful for 360 degrees vectors. The Velocity Error (VE) is difference between the magnitudes of the two vectors. It is an indication of the magnitude errors of single pixels and can be calculated as the following.

$$VE = \|\vec{b}\| - \|\vec{a}\| \quad (11)$$

The velocity error and the angular error are used to do quality measuring optical flow in computer vision. (Brox et al. 2004). Both the AE and the VE can be averaged over all pixels resulting in respect in the Mean Angular Error (MAE) and Mean Velocity Error (MVE). The MAE is an average value in degrees of deviation between the modelled and the measured vector. A number near zero indicates that the modelled direction is perfect. The MVE is the average absolute difference between the modelled vector and the measured in the same unit as the vectors.

#### Displacement

Velocities are expressed in meter per year ( $\text{m a}^{-1}$ ), because this is set in the International System of Units. It allows comparing the data of one period with other periods. Note that the velocities are not constant throughout the year and should only be interpreted during the given period of the year. The time span of the summer displacement is 153 days and the winter covers 212 days. The maximum measured velocities during a season are not the maximum velocities that could be found on the glaciers, because they are time averaged.

## 4.4. Model

Cosi-Corr is a match program developed by Leprince et al. (Leprince, Barbot, et al. 2007; Ayoub, Leprince, and Keene 2009) and is modelled in Exelis Envi environment and is written in Interactive Data Language (IDL). For this thesis, a model is written in IDL that includes the Cosi-Corr batch code. The inputs needed for this model are a master image, slave image and correlation settings. After the Cosi-Corr correlations some post-processing is done. The model reopens the image and reverses the order of the pixels. The indices of a GeoTiff file start at the lower left pixel, while an IDL matrix starts upper left. In the next step, the Not-A-Numbers (NaNs) and Infinity numbers are removed. To reduce noise there is a limited set to the velocities. This removes unrealistic high velocities caused by noise. Finally, some statistics are computed. The images and figures are plotted to assess the correlations and saved in TIFF files. The model can be found in [Appendix B](#), IDL model.

## 5. Results

---

This section presents the results of the research. To determine the best input-product the derivatives are computed of Optical and DEM imagery. The best result of these products is used for further optimizing. Different down sampling from the 0.1 m spatial resolution will be studied, as well as different cross-correlation settings. The statistics of the manually tracked points and their corresponding automated cross-correlation points will be calculated.

### 5.1. Optimal configuration

#### 5.1.1. Assessment of optical & DEM based inputs

For the input study, the same frequency correlator of Cosi-Corr is applied to all of the cross-correlations. The correlator has an initial *Window* of 128 pixels (coded as: W128) and *Finial* window of 64 px (coded as: F64). The initial window specifies the window of first correlation and the final window determines the second sub-pixel correlation. The step size determines the amount of correlations done and the pixel-size of Cosi-Corr's the outgoing image. For this chapter, the *step-size* is set to 16 px to reduce computation time (S16), so the pixel-size has a spatial resolution of 3.2 m per pixel. It is recommended to have a *robust* iterations that is set to 2 (R2) and a *mask* that is set to 0.9 (M0.9) (Ayoub, Leprince, and Keene 2009).

Throughout this thesis, such settings will be coded as 'F W128 F64 S16 R2 M0.9'. This is in the same sequence of the following configuration: Frequency correlator (F), initial window (W), final window (F), step-size (S), robust iterations (R) and mask (M). All letters are include with a numerical value, where the windows and the step-size are in pixels.

#### Optical

The optical derivatives used in this research are a brightness image, laplacian enriched brightness image (LEB) and the Principle Component 1 (PC1). They are all computed from the 0.2 m resampled ortho-mosaic data from the monsoon period. The results can be found in [Figure 29](#). The general patterns of the surface deformation show similarities of the three cross-correlations. All correlations contain a high level of detail. The level of noise is low and is mainly located around the

edge of the image, the slope of the moraines, bare ice features and surface water. The noise surrounding ice cliffs contain extreme high velocities that are greater than  $6 \text{ m yr}^{-1}$  or missing pixels, which indicates that there was no correlation possible. The LEB image does contains slightly more overall noise. This image has isolated pixels that seem to be miss-correlated. The velocities of this individual pixel-noise are off in the order of  $0.5 \text{ m yr}^{-1}$ . This indicates two levels of noise. The local-noise in areas with low correlations, containing unrealistic noise and the single-pixel general-noise that seems to varies slightly from the rest of the surrounding pixels.

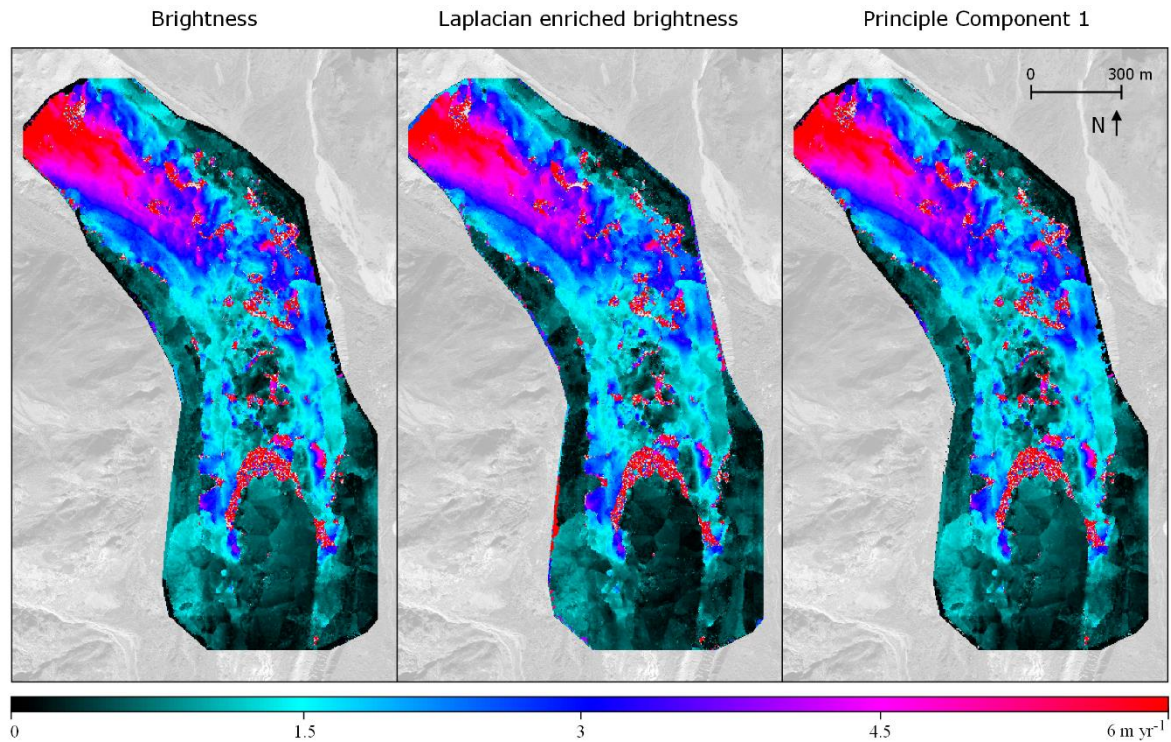


Figure 29, Intensity of the cross-correlation products of optical-image-based derivatives. The Laplacian Enriched Brightness shows best results on the lateral moraines, but contains more general-noise. The configuration for all images is: F W128 F64 S16 R2 M0.9 with a resolution of 0.2 m.

The laplacian enriched brightness image contains lower velocities on top of the lateral moraines. This dataset has an incorrect ortho-rectification, because these areas should not be moving at all. The LEB handles these areas the best of the three types of inputs and therefore the LEB can handle lower velocities better than the PC1 or the brightness image. To determine the best optical input image, the cross-correlations are compared with the ground-truth points and statistics are computed.

	RMSE $\text{m yr}^{-1}$	$R^2$	<b>b</b>	<b>m</b>	MAE $^\circ$	MVE $\text{m yr}^{-1}$
Laplacian enriched brightness	0.884	0.775	0.090	0.953	2.985	-0.024
Brightness	0.929	0.754	0.085	0.939	1.049	-0.064
Principle Component 1	1.089	0.696	0.054	0.957	1.419	-0.051

Table 2, Statistics of three optical based imagery. Laplacian Enriched Brightness has the best statistics except for the Mean Angular Error. The brightness image is the best in the MAE. The principle component 1 has lowest statistics. The configuration for all images is: F W128 F64 S16 R2 M0.9 R2 with a resolution of 0.2 m

Laplacian Enriched Brightness image has the best Root Mean Square Error (RMSE), slope and a Mean Velocity Error. It creates a larger Mean Angular Error that indicates a direction difference of almost  $\sim 3^\circ$  with an angular error standard deviation of  $32^\circ$ . Note that the outliers are removed and thus there is no local noise included. The strong edge contrast in the LEB image performs well and seems to show the best results despite the light general noise.

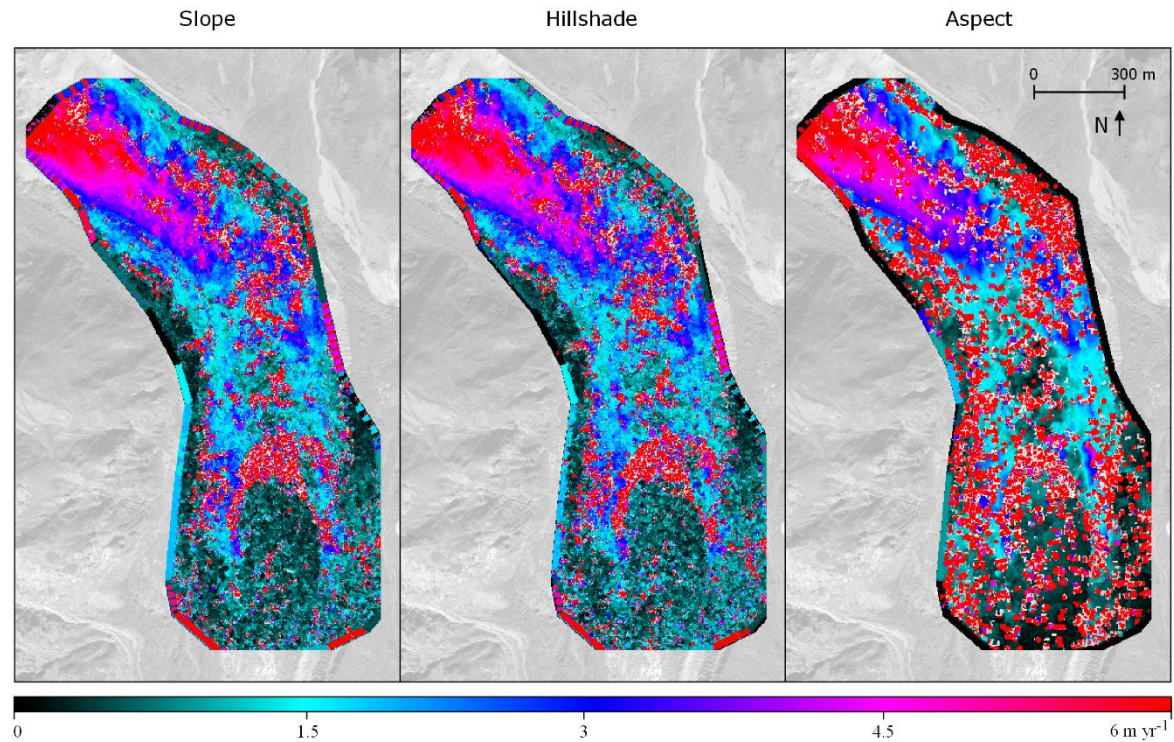
The pure brightness image has a  $\sim 1^\circ$  angular error between the measured and the modelled vector. The rest of the statistics are slightly lower than the LEB. The Principle Component 1 has the lowest scores, except for the slope (m). The low  $R^2$  however, indicates that the spread of points is large. The PC1 did not perform better than the brightness image. The concept of principle components works if the UAV data has more differences in the spectral domain. The RGB channels are too high correlated to be useful as a principle component. The extra computations relative to the brightness image is not useful.

#### Digital Elevation Models

The DEM derivatives used in this assessment are a local slope, an aspect and a hillshade. The configuration for all the DEM based images is the same as used for the optical derivatives: F W128 F64 S16 R2 M0.9. The images are computed from DEMs with a spatial resolution of 0.2 m. The intensity of the three correlations and their statistics can be found in [Figure 30](#).

The DEM based images resulted in bad correlations compared to the optical derivatives. They all contain noise local and general noise. An artificial stroke can be found near the edge of the images. The aspect image contains squared areas with unrealistic uniform high velocities. Both hillshade and aspect have no textures but plain grey shades based on shading or orientation. Across the whole image, the same combinations of greys are used. Miss-correlations are possible when there is no substantial difference between the shapes of features. The hillshade has the best statistics but far worse than all optical based imagery.





	<b>RMSE</b> m yr <sup>-1</sup>	<b>R<sup>2</sup></b>	<b>b</b>	<b>m</b>	<b>MAE</b> °	<b>MVE</b> m yr <sup>-1</sup>
Slope	1.1276	0.6194	0.458	0.7174	3.504	-0.2742
Hillshade	1.1059	0.6326	0.4426	0.7252	6.9467	-0.2694
Aspect	7.7764	0.0394	3.2221	0.8156	2.5447	2.7943

Figure 30, Three intensity of the cross-correlation products of DEM based derivatives. They all have highly noisy signals. Hillsahde has the best statistics except for the Mean Angular Error. All three inputs have very bad statistics relative to the optical based derivatives. The configuration for all images is: F W128 F64 S16 R2 M0.9 with a resolution of 0.2 m

### 5.1.2. Assessment of spatial resolution

The ortho-mosaic with 0.1 m does contains motion blur and optical error. This step is to determine the best process resolution. A high level of detail is visible in the image with a full 0.1 m resolution, but blurry UAV photographs are optical distinguishable. The blur reduces when the spatial resolution decreases. The same applies for the level of local noise. Larger pixels will cover more information and has an increased chance to be correlated correctly. The full resolution ortho-mosaic is down sampled and converted into a Laplacian Enriched Brightness images. This is based on the best results as seen in chapter 0. Down sampling of the spatial resolution can reduce noise but it also lowers the level of detail and at larger pixel-sizes, the minimum detectable deformation is larger. Displacements smaller than the size of the pixel are hard to detect. Cosis-Corr does work with sub-pixel detection but this process is less accurate (Ayoub, Leprince, and Keene 2009). This can also be seen at the 0.5 m resolution correlation in Figure 31. The images are cubic convolution down-sampled (Exelis 2015; Reichenbach and Geng 2003; Thévenaz, Blu, and Unser 2000)

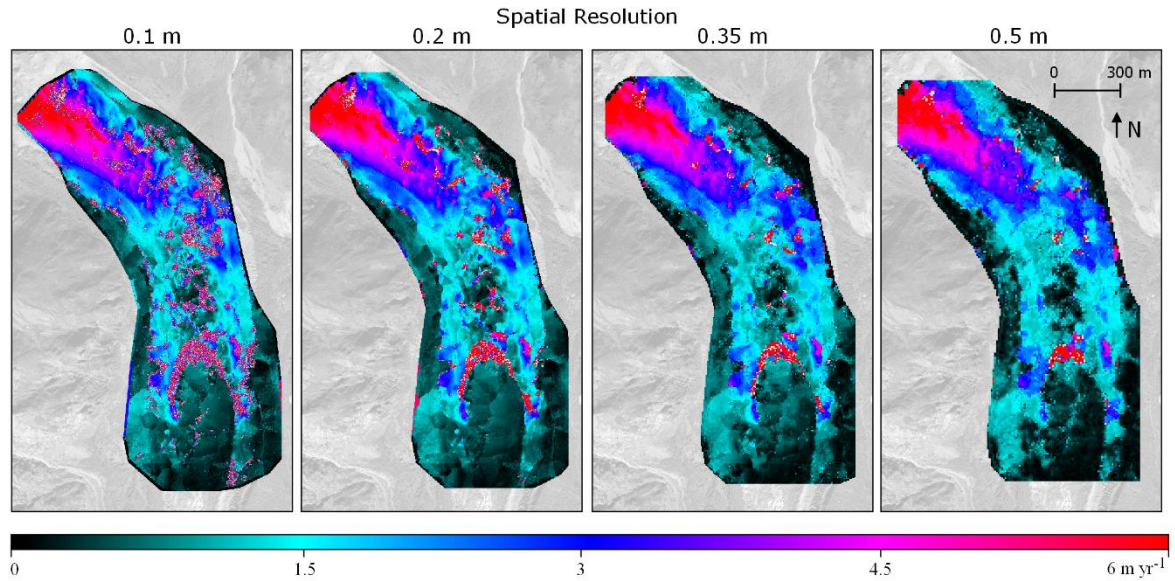


Figure 31, Cross-correlations of Laplacian enriched brightness images with resampled spatial resolutions. High resolutions have detail but also local noise. Note that low resolutions increase the real-world size of a correlation window. The configuration for all images is: F W128 F64 S16 R2 M0.9

A side effect of a larger pixel size is that the correlation window is relative larger. A window of 128px with a 0.5 m resolution is 64 m large, while the same window size is just 12.8 m in the 0.1 m resolution image. Small window sizes are not preferred, because it is depending on the maximum velocity and not on the resolution.

Another reason to reduce the spatial resolution is to lower computation times. The full 0.1 m resolution computation takes over 27 min. A double sized pixel reduces the time to 7 min and larger pixels takes even less than a minute to process. The storage sizes of the files also decrease. A doubling of the pixel size reduces the disk space to a quarter.

According to statistics in [Table 3](#), the optimum resolution for this dataset is 20cm per pixel. This is related to the amount of noise in the high resolution and the lack of information in the lower resolutions. The 0.1 m resolution contains in many regions motion blur. This will disappear when the image is cubic convolution down-sampled.

	RMSE m yr <sup>-1</sup>	R <sup>2</sup>	b	m	MAE °	MVE m yr <sup>-1</sup>
0.10 m resolution	1.072	0.701	0.106	0.955	1.604	0.0018
0.20 m	0.965	0.739	0.095	0.937	0.410	-0.057
0.35 m	1.517	0.535	0.141	0.944	3.323	0.0054
0.50 m	2.287	0.343	0.210	0.950	3.508	0.0908
1.00 m	1.453	0.531	0.209	0.907	2.858	0.0074
2.00 m	1.147	0.650	-0.0079	0.908	1.794	-0.1571

Table 3, Statistics of six optical based imagery. The optimum spatial resolution according to the statistics is around 20px. The configuration for all images is: F W128 F64 S16 R2 M0.9



The resolution is a trade-off between the level of detail on one side, and noise and computation time reduction on the other side. The 0.1 m spatial resolution could be used to research local process. While a 0.2 m pixel size could shows the overall displacement.

### 5.1.3. Optimizing correlation configurations

In the previous chapters, the settings for the correlations were kept constant:  $F$  W128 F64 S16 R2 M0.9. Each input determines the quality of the cross-correlation. In this chapter these settings are tested expect for the Step size (S). That indicates the size of the pixels and the amounts of correlations done. This is set to 16 pixels. This creates a spatial resolution of  $3.2 \text{ m px}^{-1}$  in output images. All other correlation settings are tested.

#### Window sizes

The initial window size determines the initial search kernel of the frequency correlator. A large window is less influenced by noise and it computes a smooth output. Therefore, such windows are capable to reduce most of the mass movement and ice cliff related noise. On the other hand, smaller initial windows have a finer spatial variability and they contain more details.

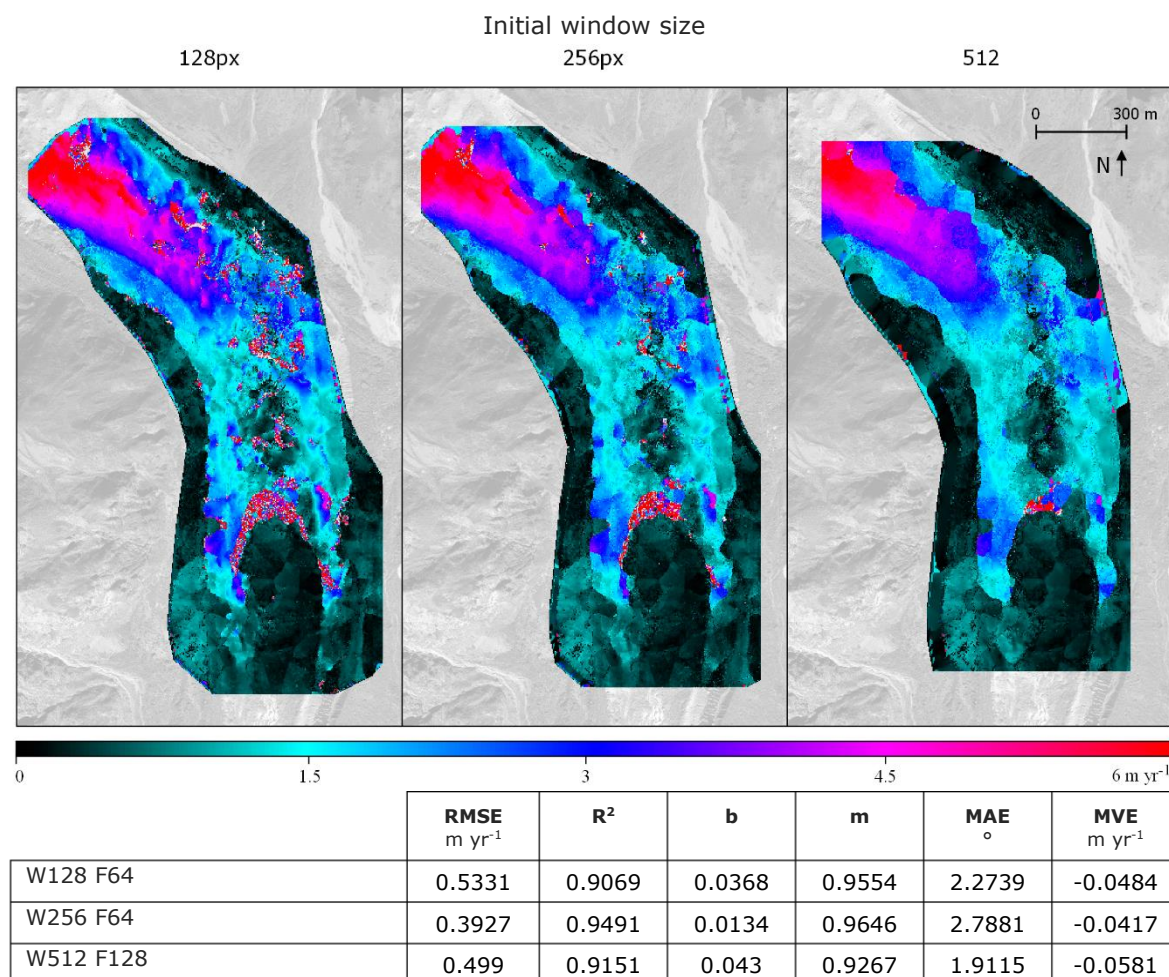


Figure 32, Three cross-correlation outputs of different initial window sizes. The large output has a low level of noise, but also a low level of detail. It also crops the image and creates artificial blob behaviour. The initial window of 128px contains a high level of detail, but the 256px window has the best statistics. Final window sizes resp. 64px, 64px, 128px. The rest of the configurations are:  $F$  S16 R2 M0.9



The results of a correlation with the 512 pixel window shows unrealistic boundaries between areas with different velocities. This artificial behaviour has a circular blob pattern and is not related to the UAV photographs. Lower initial windows show also this pattern but on a smaller scale and therefore, the effect is related to the initial window. The correlation windows are rectangular, but Cosi-Corr uses a Gaussian kernel during its correlation. This kernel might be causing the circular pattern.

Cosi-Corr creates an artificial stroke that surrounds the edge of the data. The values inside this stroke are unrealistic. The stroke has no texture and seems to be artificial. Cosi-Corr crops also any data close to the edge of the image. Both the cropping and the stroke have the same order of size as the initial window size. It should be taken into account that the frequency correlator is not capable to correlate near the edge of the data or the image.

The best window configuration for this data set is an initial window of 256 pixels. The statistics indicate that a window size of 256 pixels results in the best correlation relative to the ground-truth points. This is considering the blob behaviour at large initial windows and the optimum in the trade-off between noise and detail.

#### Mask

The Mask (M) contributes in reducing noise on the measurements. The frequency mask is applied on the cross-spectrum (Leprince, Barbot, et al. 2007). As shown in Table 4, a mask of 0.90 gives the best statistics in this dataset.

	RMSE m yr <sup>-1</sup>	R <sup>2</sup>	b	m	MAE °	MVE m yr <sup>-1</sup>
Mask 0.95	0.445	0.9325	0.0093	0.9513	2.8897	-0.0643
Mask 0.90	0.417	0.9437	0.0123	0.9527	3.1115	-0.0621
Mask 0.80	0.4762	0.9207	0.032	0.951	2.3785	-0.0556

Table 4, Statistics of three different mask values. Noise increases when decreasing the mask. Values above 0.9 do not reduce the amount of noise any further. The configuration for all images is: F W128 F64 S16 R2

The Robustness iteration (R) is the number of the times per measurement the frequency mask should be re-computed. Iterations increase the correlation accuracy and robustness. It is recommended that 2 to 4 iterations is satisfying in most cases (Leprince, Barbot, et al. 2007). A change in robustness iterations from 2 to 4 shows no difference in statistics.

## 5.2. Quality of assessment

Given the large errors in the correlation maps, physical interpretations of the correlation maps are needed. The ground-truth points are accepted as truth to assess the quality of different outputs of Cosi-Corr. However, the cross-correlation map has more spatial variety and detail than the interpolated Ground-Truth map. With a spatial resolution of 3.2 m per pixel, the cross-correlation products have ~22.000 cells. The visually tracked ground-truth contains only ~500 points, with a mean distance of 25 m between points. The automated correlation map contains 7.8 times more tracked areas. For this reason, the ground-truth points should be used to assess the quality Cosi-Corr and this is done with the ~500 points corresponding samples from the automated maps.

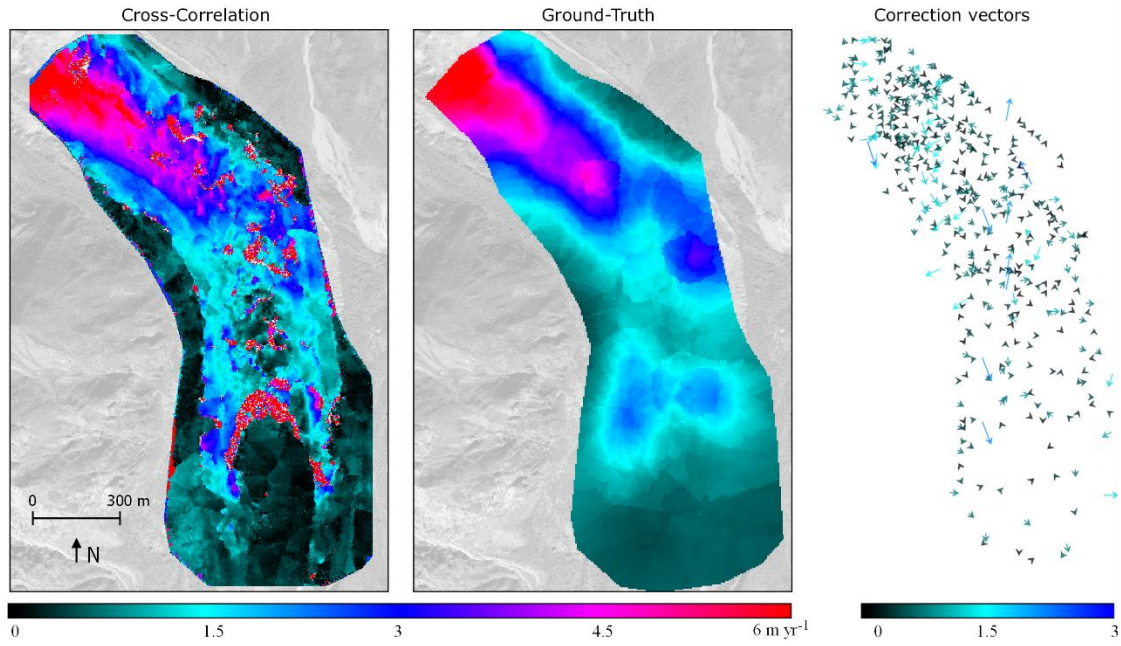


Figure 33, *Left*: Cross-correlation output of Cosi-Corr. *Centre*: Ordinary kriging interpolated ground-truth map. *Right*: The correction vectors. The non-uniformity of the correction vectors indicates that there is no constant error in both angle and magnitude. The maximum correction vector is  $1.8 \text{ m yr}^{-1}$ .

The correction vectors in right plane of [Figure 33](#) have a random pattern. The deviation between the automated and manually correlated points has no constant direction or magnitude. Therefore is not a specific under- or over-estimation. The random pattern and relative low magnitude can be explained in the inaccuracy of both the automated correlation and the manually tracked points.

The Cosi-Corr's internal Signal-to-Noise Ratio channel (SNR) is some indication of the quality of the correlation. The cell with a SNR value of one has a high correlation coefficient and values close to zero have no correlations at all ([Leprince, Barbot, et al. 2007](#)). Only off-glacial areas have uniformly perfect correlations. The glacier contains a random pattern of mixed good and bad correlations. The SNR matrix has almost no moderate values, see [Figure 34](#). There seem to be no specific areas have bad correlations, but non-moving areas do result in better correlations.

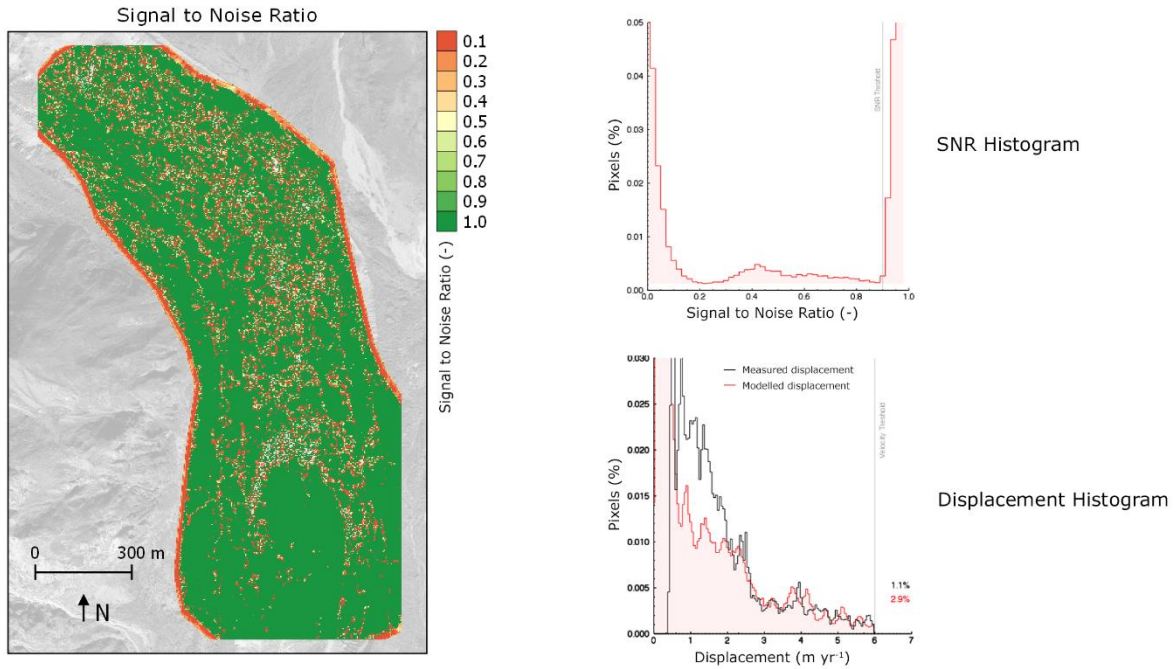


Figure 34, *Left*: Cose-Corr's SNR map, where 1 is a perfect correlation and 0 no correlation. The lowest values are uniformly spread on the glacier, except for edge related values. The displacement histogram of automated and interpolated manual correlations seems to match, if corrected for lacking low displacements.

The SNR channel is used to mask bad correlations. The histogram implies that there are mainly extreme ratios and mid-range ratios do almost not occur. During this research, the SNR threshold is set at 0.9. This includes the close-to-perfect peak visible in the histogram. Lower values are considered as low quality correlations.

The automated displacement histogram in [Figure 34](#) shows similarities with the interpolated manual displacements larger than  $2 \text{ m yr}^{-1}$ . The lower displacements of the manual correlation seem to be compress by the lack of low values. This can be explained by the lack of detail, especially in areas with low velocities. The error of correlating by hand is  $0.8 \text{ m yr}^{-1}$  and might be the reason for the offset. The displacements that have the same size of the pixels seem to be lacking in the histogram.

A maximum displacement threshold is set to remove displacement above  $6 \text{ m a}^{-1}$ . Everything that moves faster than this value is considered as noise, optical error or unwanted mass movement.

### 5.3. Seasonal differences

Previous figures in this thesis showed the surface displacement during the monsoon season from May 2013 to Oct 2013. A third image of May 2014 allows tracking displacements during the dry-season, the winter.

The lower parts of the tong are close to stagnant all year around. The average summer displacement ranges to  $5 \text{ m a}^{-1}$  in the northern part of the surveyed area. Winter velocities are considerably lower, as seen in [Figure 35](#). The average maximum velocity during this season is  $2.6 \text{ m a}^{-1}$ . The summer velocities exceed the winter displacements by factor two for 84% of the

glacier. This is ratio of two is constant throughout the glacier except near the terminus, where the summer velocities are only 10-20% larger. The winter displacements at the bend are in the order of  $1.5 \text{ m a}^{-1}$ . The summer displacements in the bend are noisy and less clear, some areas move with  $2.8 \text{ m yr}^{-1}$  while other pixels displace with just  $1.2 \text{ m yr}^{-1}$ .

The automated correlation of imagery of May 2013 and May 2014 captures 95% of the days of the year. The annual average displacements are maximum 3.2 m in the upper part of the surveyed area. The bend displace with 1.2-2.2 m in a year while the common displacement near the terminus is around  $1 \text{ m a}^{-1}$ .

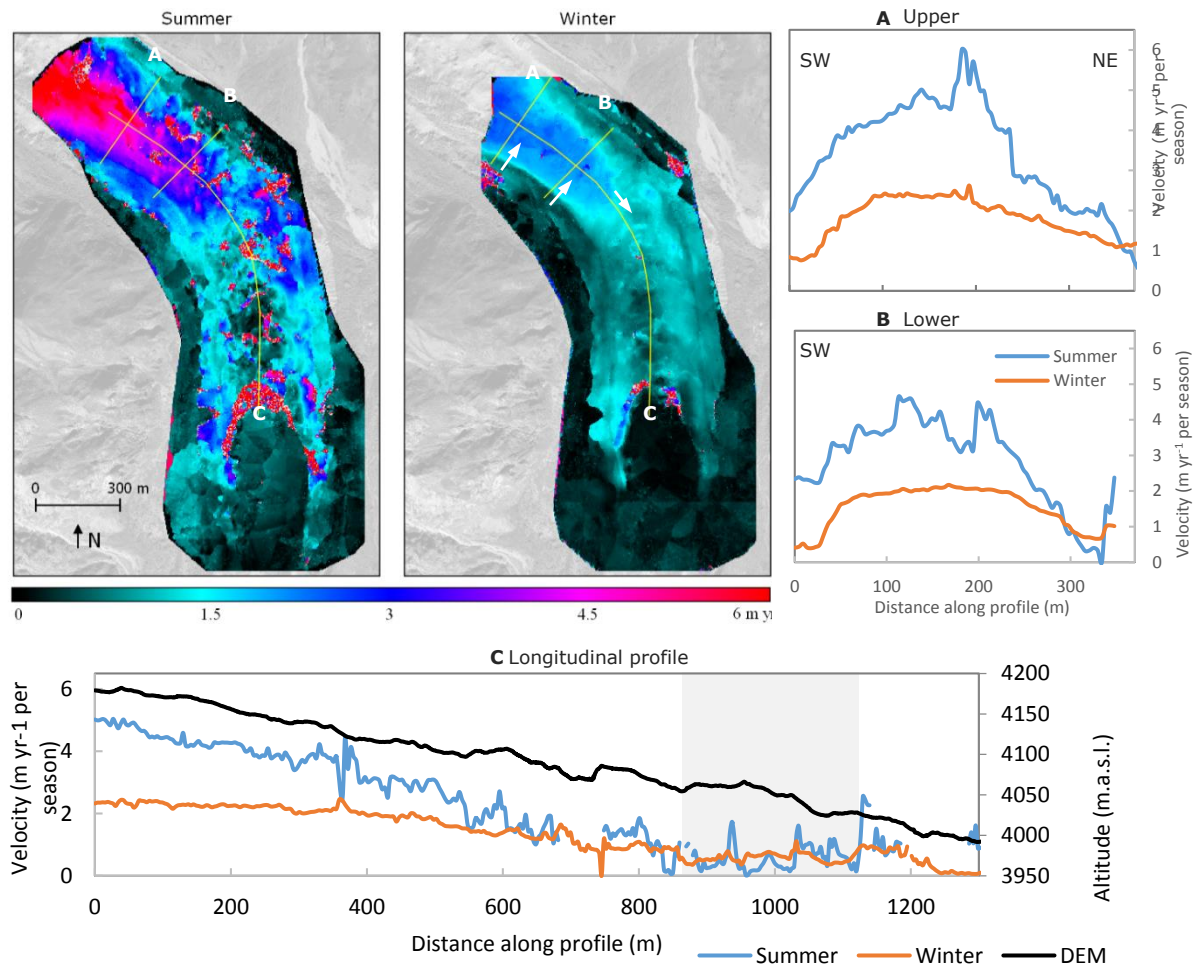


Figure 35, Seasonal displacements of summer and winter. The surface displacement decreased during the winter season, but the general pattern is unchanged. Figure A and B are cross profiles. In the longitudinal profile C is a depression visible (grey area) in both seasons. The summer velocity is in the order of two higher. The configuration for all images is: F W128 F64 S16 R2 M0.9 R2 correlation on 20cm Laplacian Enriched Brightness images.

### 5.3.1. Flow pattern

Throughout the glacier it seems the general displacement direction is lateral to the tongue, but with  $\sim 45^\circ$  angle towards the centre of the glacier. The flow direction does barely change on local scale, but note that in Figure 36 cliff-related noise and the blob-shaped defects are visible. On the lateral moraines, the displacement direction is perpendicular to the glacier and is caused by slope instability and mass movement.



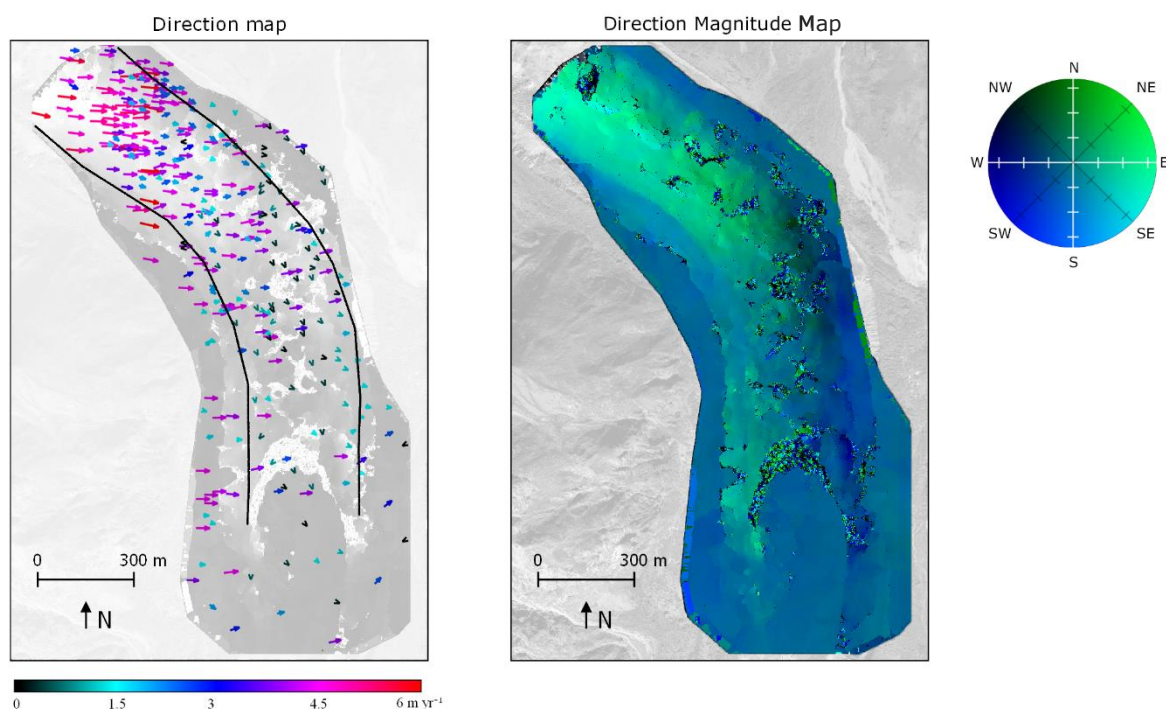


Figure 36, Left: Colorized and scaled displacement vectors indicate the flow direction and velocity. The upper part of the glacier has an EES direction with high velocities. Mass movement is visible outside the glacier (black lines).

## 6. Discussion

In this research, orthographical surface displacements are computed with Cossi-Corr software. A model was written in IDL to assess the best configurations. Then the outputs were compared with manual tracked displacement points. Each part of these assessments will be discussed in detail, starting with the accuracy of displacements, followed by the optical errors of the input and finally an assessment of quality and glaciological interpretations. Deformations are interpreted in flow velocities and patterns on a full glacial spatiotemporal scale. Specific regions are investigated with high-resolution observation.

### 6.1. Optimal Configuration

The Laplacian Enriched Brightness (LEB) images were found to provide the best statistic in relation to the visual measured ground-truth points. They contain slightly more general-noise, but this can be reduced by the right configuration and post-processing. A LEB with a spatial resolution of 0.20 m provided the best balance between noise and detail. The pixel size is small enough to determine spatial variations, but is not dominated by motion blur. With this resolution, the local-noise is reduced to areas that are considered difficult to track, i.e. ice cliffs and areas with mass movement.

The optimum initial window has 256 pixels due to the trade-off between a reduction of noise and artefacts, and the level of detail. The corresponding final window is 64 pixels large so it reduces the noise to acceptable levels. Statistics can be found in [Figure 37](#).

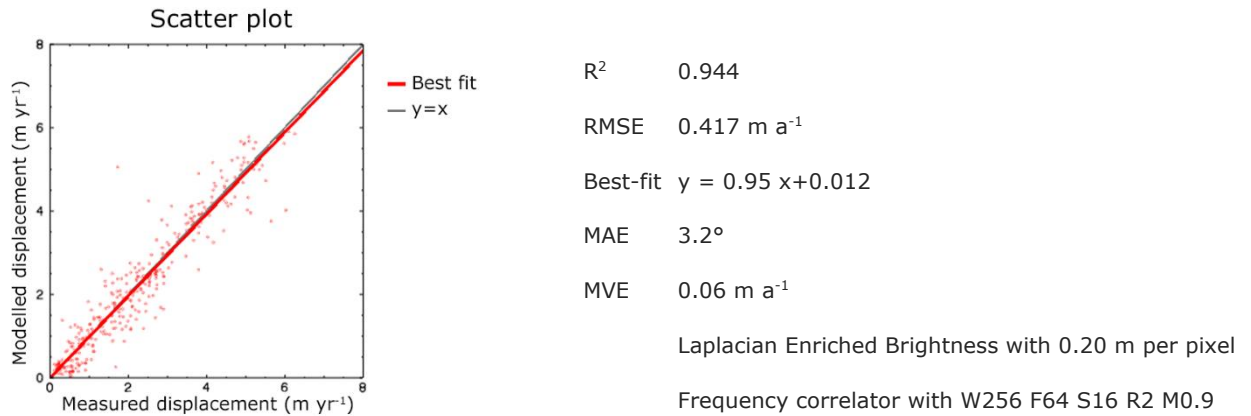


Figure 37, Statistics of the best configuration found in this research. It is based on two Laplacian Enriched Brightness images with a spatial resolution of 0.20 m per pixel. The best-fit line approaches the theoretical 1:1 line.

A cross-correlation with an initial window of  $\geq 512$  pixels and a  $\geq 0.5$  meter pixel-size compute a displacement map that shows general displacement patterns. The ice cliffs-related, general and local noises are reduced by the large correlation window. A general displacement map is useful for researching glacial flow without the local disruptions. In this research, the visual based ground-truth points are already used for a general displacement map.

On the other hand, small initial windows and small pixel sizes create a fine spatial variation map. These maps have the advantage of the level of detail and should be used for local flow processes like ice cliffs or emergence velocities.

## 6.2. Accuracy of displacement

The accuracy of the displacement is based on several factors. Firstly, the input data contains multiple optical errors and offsets. Secondly, the results of the automated displacement maps by Cosi-Corr contain artificial defects and inaccuracy.

### 6.2.1. Optical errors

The optical errors from the UAV imagery ( $E_{UAV}$ ) can be problematic for feature tracking. The manually and visually tracked points are based on one feature, e.g. boulders and rocks. The inaccuracy of tracking of one point could be large, because the features could contain parallax, blur and different shading.

In [Figure 38](#), a parallax can be seen at a boulder. Parallax is caused by different camera positions. A parallax can be corrected by stretching the image on a local scale and this can be considered as an ortho-rectification. It requires highly spatial DEM information, but the DEMs are derived from the same photos and the same parallax errors are included in the DEM. Parallaxes make manual correlation of big boulders impossible.

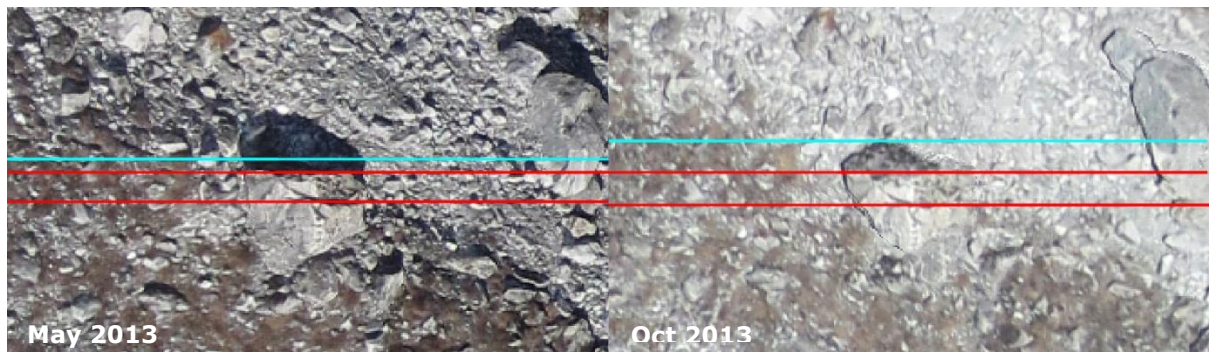


Figure 38, Parallax of a boulder as seen in the data of May 2013 and October 2013. The space in between the red lines is the same in both images. Due to parallax the right photo shows more of the north-face of the rock indicated with the space between the cyan and red line. Therefore, the rock has a different shape. The presence of the shadow could cause miscorrelations as well.

Image parallax occurs when an object with elevation is captured under an angle. This happens mainly near the edge of a photo, where the angle of towards the camera is not nadir. A parallax means that the positions of elevated objects are projected further away from the centreline of the camera. When merging two images together, this point should not be taken as common point, because it has false projection, as seen in [Figure 39](#).

Boulders that contain parallax are not used in the manual correlated points, because the uncertainty is too big. It is, however, unknown if there is any parallax at larger scales. The glacial surface of the Lirung glacier consists of steep relief.

Parallax errors can be solved by ground control points or a third nadir image of the area. The ground control points make the ortho-rectification more robust at a general scale and therefore parallax at local relief is unlikely.

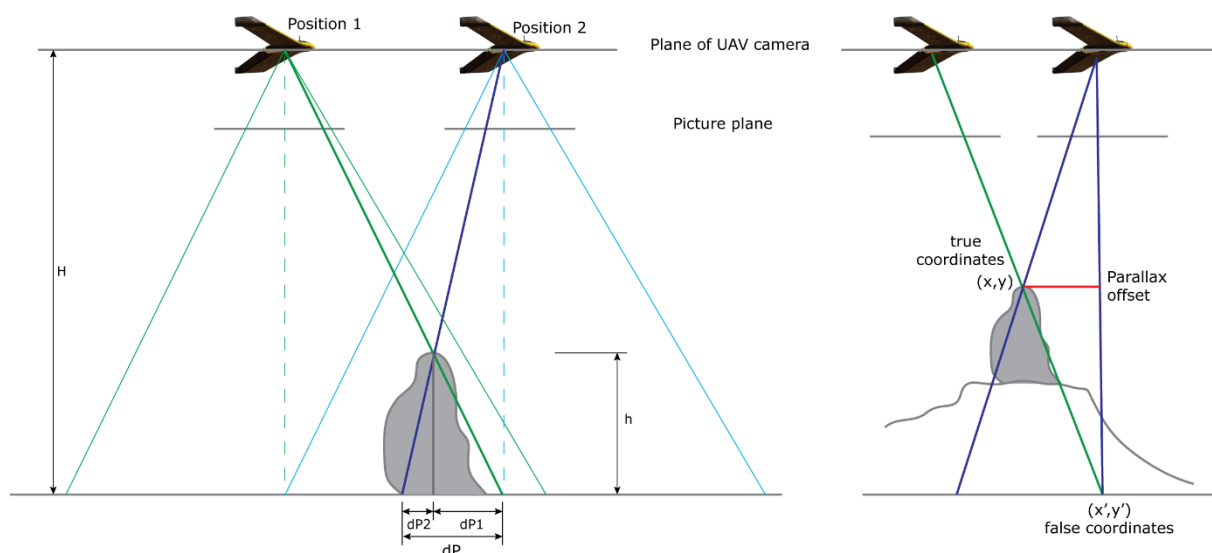


Figure 39, *Left*: the same rock is projected at different locations on the base line by two camera positions. Every image has its own parallax (resp.  $dP1, dP2$ ) that combines when stitching the images ( $dP$ ). *Right*: Rectification based on the top of a boulder in the first image creates false coordinates. When the second image finds its correlation at the boulder, the false coordinates are used. This creates a parallax offset for the rest of the image. This occurs at small scale near boulders but also on top of hills at a larger scale.



### 6.2.2. Parallax offset

The parallax in the Lirung dataset influences the Structure from Motion process. The photos are stitched together based on feature correlation, e.g. big boulders. These boulders may contain a parallax. The top of the surface is projected at a different location in the coordinate plane. This can be seen on the right side of [Figure 39](#). Rectification of this boulder with false coordinates causes a parallax offset in the rest of the image. This happened multiple times in the October 2013 Lirung dataset. The correlation equations of the Structure from Motion use boulders to rectify the image because they contain a lot of contrast, but these have false coordinates due to parallax. If in the surrounding areas, no other features are available the boulder could be unjustly rectified. This creates an offset in the rest of the image. An example is visualised in [Figure 40](#).

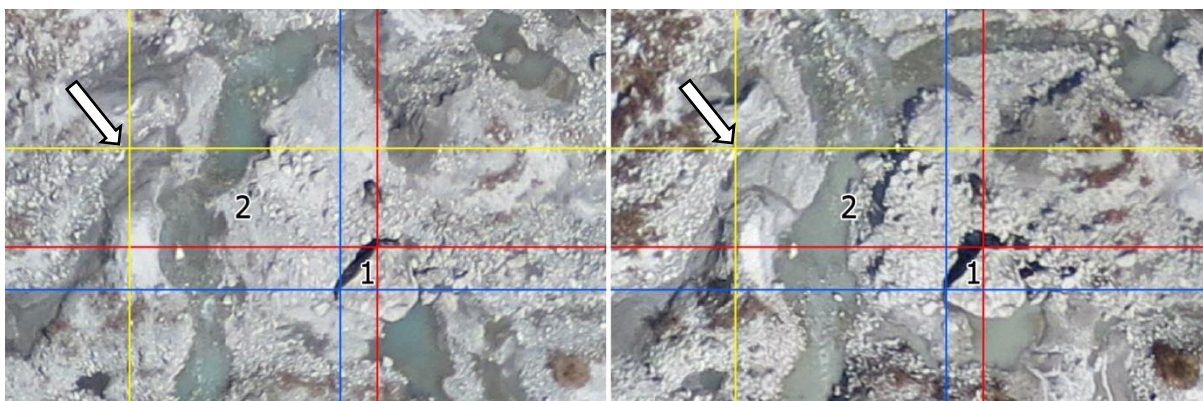


Figure 40, Wrong rectification of the top of a boulder. The SfM process has corresponding matches on the red and blue cross because both have high contrast. This is a false match due to parallax caused by the boulder. The rest of the image have no corresponding matches and is moving unjustified. This is shown by the white stone near white arrow. In the right image, the yellow cross is on top of a white stone. The left image, the cross is offset relative to the same stone.

### 6.2.3. Reducing optical errors

When manually correlating, the parallax, blur and shading can be controlled for by sampling other small white bright rocks. These features should be in the same order of twice the pixel size. Parallax and shading are probably not relevant because the relief is low. Blur can be problematic and thus highly blurry areas should be avoided when manually tracking features.

Parallax can be prevented by long focal length to capture photos orthographically. The angle in inclination is zero at nadir. The parallax cannot occur at nadir because the UAV photographs are already orthographical to the line of sight of the camera. For long focal lengths, the UAV needs to fly at higher altitude in order to maintain the same number of photographs and thus the same amount of operation time, but this increases flight instability.

Cosi-Corr uses cross correlations to track an area. A boulder that contains parallax will not dominate the automated correlation of an area. Therefore, the inaccuracy of an area correlation is lower than the error that comes with a point correlation. A parallax offset in the SfM workflow does effect Cosi-Corr and should be kept at a minimum.

#### 6.2.4. Incorrect correlation data

Seams between the UAV photos are visible to the south of the terminus in the summer dataset. This indicates false displacements within the photos and is likely to occur. This can be caused by lens distortion, incorrect cross-correlation due to motion blur, incorrect SfM process or a combination of all three. The displacement difference over a seam can be as high as 0.4 m yr<sup>-1</sup>. The false displacements show that the automated cross-correlations done by Cossi-Corr are more sensitive than the structure from motion process based on the data of an UAV.

#### 6.2.5. Displacement errors

Every step in the process chain creates an error, from capturing the raw UAV imagery to correlation of the flow maps. All these errors contribute to a final error. The error of the Root of the Sum of every error Squared (RSS) compute the final error.

$$E_{total} = \sqrt{(E_{uav})^2 + (E_{sfm})^2 + (E_{cross})^2 + (E_{ref})^2 + (E_{ortho})^2 + (E_{match})^2 + (E_{locate})^2 + (E_{surface})^2} \quad (12)$$

In [Table 5](#), an overview of the individual errors is given. The optical errors  $E_{UAV}$  depend on the stability of the UAV and the quality of the camera, parallax, noise and lens disruption. Additional errors that occur during the full processing are based on the quality of the imagery.

The errors introduced by Cossi-Corr are caused by bad correlations, miss locations and mismatches. Bad correlation errors ( $E_{cross}$ ) occur when signals are very weak, contain low contrast, extreme noise or when signals match, but the absolute values are far apart. In addition to general and local noise, there are artificial defects in the automated displacement maps. Every feature has an error that is introduced by miss locating ( $E_{locate}$ ) the correlation. Miss locations can occur when signals have repetitive patterns or an image contains parallax or blur. This occurs mainly in sub-pixel detection and the error maximum is usually in the order of the pixel size. When a correlation matches with a signal-similar feature, it is a mismatch ( $E_{match}$ ). This occurs around ice-cliffs and such mismatches can be unrealistic high. The error caused by Structure from Motion, geo-referencing, ortho-rectification ( $E_{SfM}$ ,  $E_{ref}$ ,  $E_{ortho}$ ) are measured by Immerzeel et al. The ortho-rectification of the May 2013 imagery has a horizontal error up to 0.67 m. The October 2013 data set is more accurate and has a horizontal error of 0.25 m ([W. W. Immerzeel et al. 2014](#)). The measured error of the May 2014 data is 0.76 m, but it is probably lower considering the fact that the off-glacial areas are not moving in that order of magnitude ([Heuff 2014](#)).

The vertical error of the DEM is between -0.3 and 0.6 m. The computed DEM-derivatives contain this error during the pre-processing. This error is larger than the error of the ortho-mosaic and therefore the ortho-mosaics should be used for correlations and interpretations.

The manually tracked points are compared with the Cossi-Corr flow map to measure the accuracy of the Cossi-Corr. The manually tracked points are considered as ground truth and therefore the errors are caused by Cossi-Corr. Both automated and manual correlations have the same input map. The error  $E_{cossi\_corr}$  is a root of the sum of every error squared:

$$E_{cosi\_corr} = \sqrt{(E_{cross})^2 + (E_{match})^2 + (E_{locate})^2} \quad (13)$$

The Velocity Error created by Cosi-Corr can be computed and is based on the difference of the magnitudes of the displacements between manually and automated correlations maps. The summer errors are within 7.01 m, but the bulk of measurements are less than 1.17 m. The automated correlation points of the winter season are within 1.56 m of the measured points and the bulk is even within 0.24 m. The imagery of the winter has better optical quality and thus both automated and manually correlations are more accurate. To improve the assessment of the accuracy of Cosi-Corr stakes could be measured with GPS.

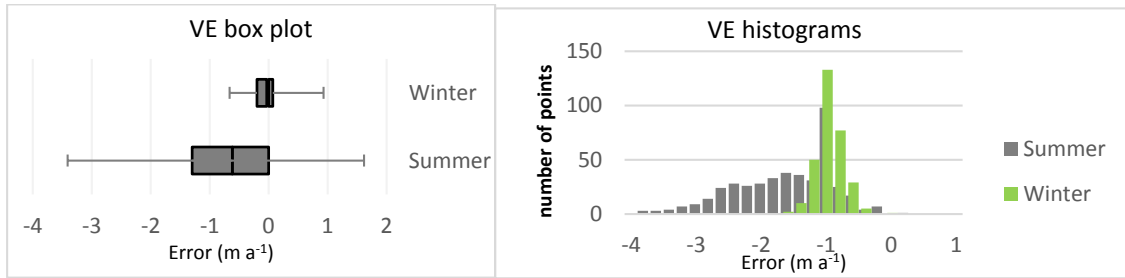


Figure 41, The *left* panel shows box plots of the velocity error (VE) based on the ~500 manually tracked points and there corresponding automated cross-correlation points for both summer and winter season. The boxes represent the interquartile range and the lines the maxima and minima. *Right*: A histogram is plotted with the VE of both seasons.

An additional error  $E_{visual}$  should be considered for compensating visual-track errors. The vectors may contain user-based inaccuracy. This is mainly a mislocation of the corresponding feature. This error is estimated at a maximum of 3 pixels. For the summer period the error is  $\pm 0.3$  meter that equals to about  $\pm 0.70$  m yr<sup>-1</sup>, respectively for the winter season is this  $\pm 0.57$  m yr<sup>-1</sup>. The absolute error for the winter is lower due to the timespan of the images. However, note that it is large relative to the magnitude of the displacement.

During the pre-process, an off-glacial area is used to rectify the mosaic image. The same area can be used to check the quality of correlations, assuming there is no displacement in this area. In the summer dataset, the lateral moraines have incorrect displacement of  $0.52$  m a<sup>-1</sup>. The area west of the terminus is even moving with more than  $1$  m a<sup>-1</sup>. During the winter, the lateral moraines move with approximately  $28$  m a<sup>-1</sup>. The displacement in the correlation map minus the input error estimates the error caused by Cosi-Corr. Both

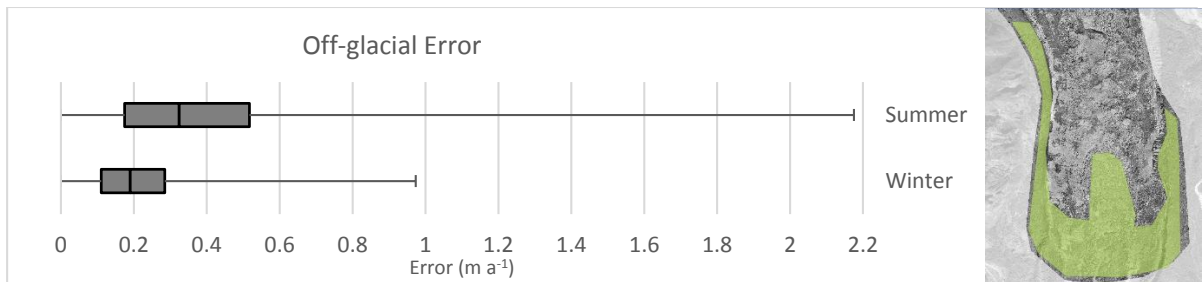


Figure 42, Box whisker plot of the off-glacial areas. The off-glacial areas are the lateral moraines and the area to the south of the terminus, projected in green in the right image.

Error		Based on	May 13	Oct 13	May 14
$E_{UAV}$	UAV inaccuracy	Stability and camera	±0.67 m	±0.25 m	±0.76 m
$E_{SfM}$	Structure from Motion	Quality of imagery*			
$E_{ref}$	Geo-referencing	Ground Control Points / GPS			
$E_{ortho}$	Ortho rectification	Digital Elevation Model*			
$E_{cross}$	Cross Correlation	Quality of imagery*	±0.63 m		±0.49 m
$E_{match}$	Correlation mismatch	Quality of imagery*			
$E_{locate}$	Correlation miss located	Quality of imagery*			
$E_{surface}$	Surface transformation	Mass movement, ice cliffs	Locally, unknown		
$E_{Total}$	based on off-glacial areas		0.52 m	0.28 m	

\*Error can partly be reduced by optimising algorithm/program settings.

Table 5, Overview of different errors that occur during the process from flying the UAV until the displacement maps. The spatial error of the imagery was given by Immerzeel et al (2014) and the error of Cosi-Corr is computed referenced to the Ground-Truth points.

### 6.3. Glaciological interpretations

The input files of the automated cross-correlations are ortho-rectified images. Tracking these images is an estimation of the orthographical surface displacements. The theoretical displacement is a combination of glacial flow, mass movement, emergence and melting processes. The empirical displacement however, includes miscorrelations, noise and process inaccuracies.

#### 6.3.1. Flow velocities

The ortho-rectified UAV imagery displacements are measured in the horizontal plane. These displacements are called kinetic boundary conditions. The surface kinematics can be computed with mass continuity from the orthographical displacement. According to Kääb (2005) mass loss or accumulation, mass advection and three-dimensional straining can be quantified. This is based on input conditions e.g. strain rates, surface slope components, medium characteristics and velocity vectors. The displacement in the horizontal plane, the output of Cosi-Corr, differs from the surface flow and the flow of a particle as shown in Figure 43.

The surface velocities should be corrected for surface slope. The average slope on the surface glacier is  $0.16 \text{ m m}^{-1}$ . Assuming there is no variation in thickness of both the debris and ice, the correction for general slope would just result in additional 0.13% displacement. However, ice thickness is decreasing in the longitudinal profile and therefore the velocities are higher.

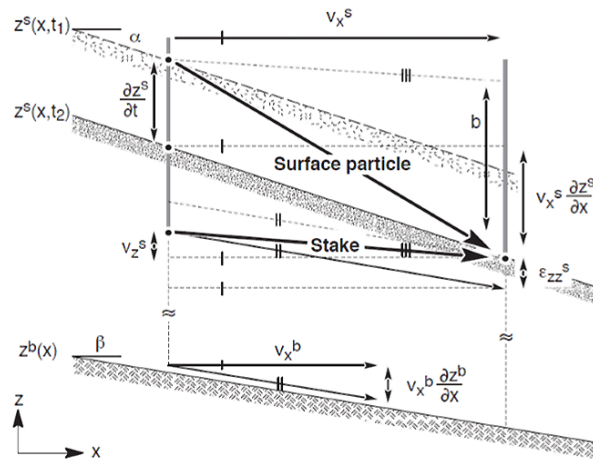


Figure 43, *Upper*: Different terms in kinetic boundary conditions. Orthographical surface displacements are different of surface flow and particle flow. *Lower*: Bedrock deformations contribute to basal slide. (A. Kääb 2005a)

The velocities found during this research are lower than Natio (2002) measured during the summer period. They stated that the glacier moved between  $13.4 \text{ m a}^{-1}$  (2.8 m in 76 days in 1994) and  $18.6 \text{ m a}^{-1}$  (7.3 m in 143 days in 1996) near the bend. The maximum velocity measured in the same area is about  $5 \text{ m a}^{-1}$  (2.1 m for 153 days in 2014). In 20 years, the surface displacement decreased between a factor 2.7 and 3.7.

The measured velocities in this study are season-averaged. This means that the actual maximum velocity is probably higher. Interval in situ measurements are needed to calibrate the model and to estimate the maximum velocity.

The data in this research covers a timespan of about one year. A multi-temporal data with a span of multiple years is required to determine a dominate signal (A. Kääb 2005b). The comparison to manually correlated map is sufficient, but strategically placed in situ measurement could calibrate the model and asses the quality of the map even further.

### 6.3.2. Flow regime

In areas where basal slide dominates, the ice moves with constant and high velocities. The basal slide is fastest in the glacial centre and it decreases towards the moraines (Copland et al. 2009). This pattern is clearly visible in the Lirung data. Summer velocities are generally twice as high as the winter velocities. The difference is probably caused by basal lubrication of subglacial water. Immerzeel et al. (2014) hypothesized that sub- and englacial conduits open during the summer and together with precipitation, the glacier is basal-slide dominated, at least in this season. Commonly at temperate glaciers, 60 to 80% of the total velocity is accounted for by basal slide (Harper et al. 2001).

Low flow velocities that have a parabolic pattern are likely to be dominated by internal deformation. The ice near the lateral moraine experiences the drag of the wall (Nozomu Naito et al. 2002). The flow patterns, however, found on the upper part of the glacier are asymmetrical, see cross section profiles in Figure 35. The flow velocities are highest in the inner bend. The ice in

the outer bend has emergence velocities. Here, according to mass continuity the ice moves more in an upward direction and less in a horizontal direction.

The change in direction of  $\sim 45^\circ$  towards the lateral moraines was also detected by Naito et al (1998). Various factors could cause this pattern. Firstly, it is that the weight of avalanches and rock fall near the moraines add up to the gravitational forces, pushing the ice towards the centre. Secondly, there might be a difference in the underlying bedrock. The lithological characteristics and topography can vary and a hyperbolic bedrock profile might cause a basal slide force that moves the ice towards the centre. Thirdly, variations of the internal stress within the ice can cause patterns like the ones found on the Lirung glacier. At bare-ice glacier, crevasses can have a  $45^\circ$  angle towards the main flow direction, see Figure 44. Strain occurring in such crevasses is larger than the internal stress and the ice breaks perpendicular to the flow (Cuffey and Paterson 1970; B. J. F. Nye 1952). The flow direction appears to change direction towards the lateral moraines with approximately  $45^\circ$ . Crevasses could exist on the Lirung glacier, but they would be filled up with debris from the surface.

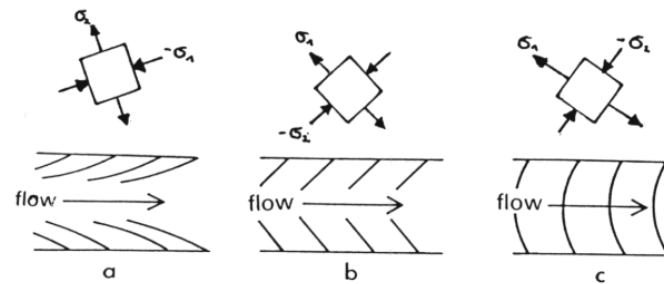


Figure 44, Different crevasses patterns with their corresponding internal stress. The pattern at the Lirung glacier might match to the stress drawn in figure b due to shear stress of the lateral moraines. (B. J. F. Nye 1952; Cuffey and Paterson 1970)

### 6.3.3. Depression

To the north of the terminus, there is a decrease of the magnitude of both winter and summer displacements. This area is almost stagnant during the summer, but it has a slightly greater velocity in the winter. In the grey section in the longitudinal profile in Figure 35 and in automated correlations in Figure 45 this depression is visible.



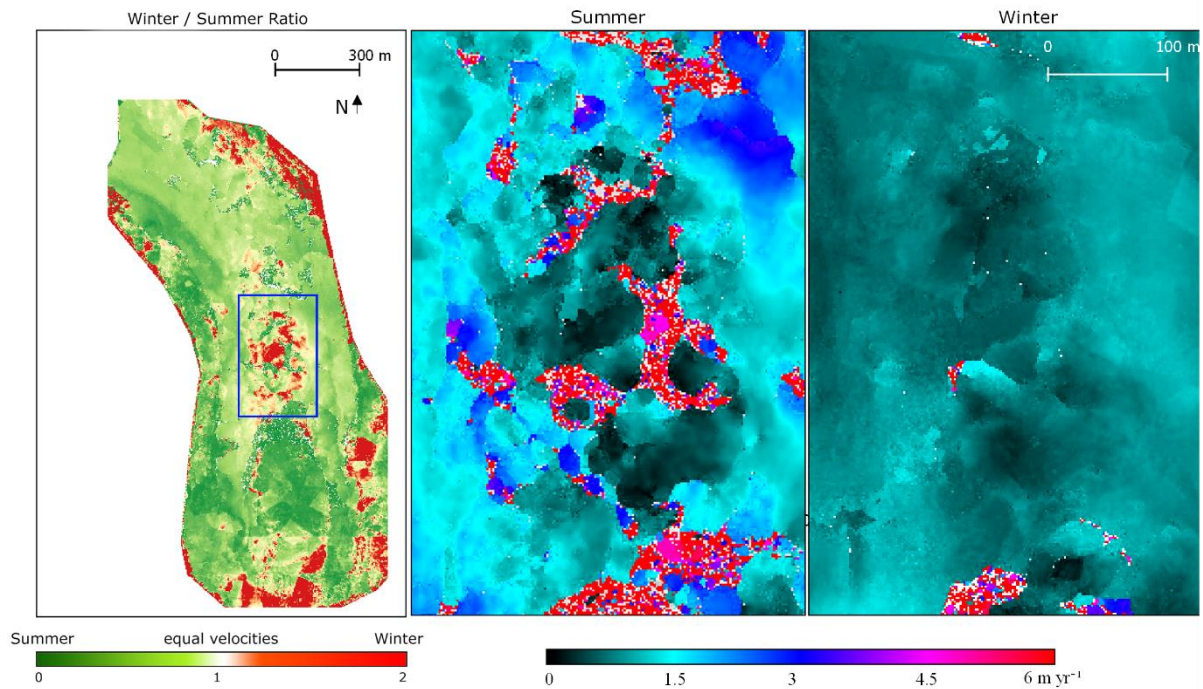


Figure 45, *Left*: Winter / Summer displacement ratio. Green colours have higher summer velocities and red colours have higher winter velocities. The bad orthorectifications cause higher winter velocities in the off-glacial areas. To the north of the terminus a depression is visible in velocities, as shown in two right images.

The physics for the depression in the magnitude of displacement in both seasons is unknown. A theory is a decreased slope in the bedrock. The local ice depth can be smaller and the friction can be larger. These factors lower the flow velocity of the ice. A bed profile is not available, but the slope of the surface does tend to decrease in this area. Another theory is that both basal slide and internal deformation are close to zero, but in ??some areas flow is driven by other processes.

In both seasons, a longitudinal gradient is visible, see the longitudinal profile in [Figure 35](#). Ice is flowing towards a stagnant area and, thus glacial volume is reduced. This can result in ice compression, emergence, mass loss or a combination of all three. The reported surface elevation gain of about 0.5 m over the summer in the bend ([Immerzeel and others, 2014](#)) is an indication of emergence velocities.

#### 6.3.4. Back wasting

Surface debris can warm up to 40 degrees by solar radiation. Bare ice cliffs receive a great amount of long wave radiation from rocks nearby. Other long wave radiation is transmitted by bare rock on the south face of mountains. This radiation travels in southern direction and therefore only north-face ice cliffs are able to receive this. South-facing ice cliffs are gentle in slope and tend to disappear. The upper part of the ice cliffs receives more sun radiation, this reduces the angle of the slope and debris covers the slope in time. North-facing ice cliffs maintain their steep slope and are therefore more stable ([Sakai, Nakawo, and Fujita 2002](#)). Because of the amount of noise near ice-cliffs, back wasting is not tractable with automated correlations of the UAV dataset used in this



study. The width of the noise stroke is some indication of the propagation rate of the ice-cliff but is very inaccurate compared to manual tracking in the ortho-mosaics.

### 6.3.5. Mass movement

The lateral moraines are steep but on top of the glacier, there is also steep relief. Mass movement, sliding, rolling and landslides are possible. Displacements perpendicular to the glacial flow are located in the steep parts of the lateral moraine. The slope instability is caused by hydrological processes together with undercutting of the foot of the slope by the glacier flowing downhill. Vegetation does increase the stability of slopes during all seasons.

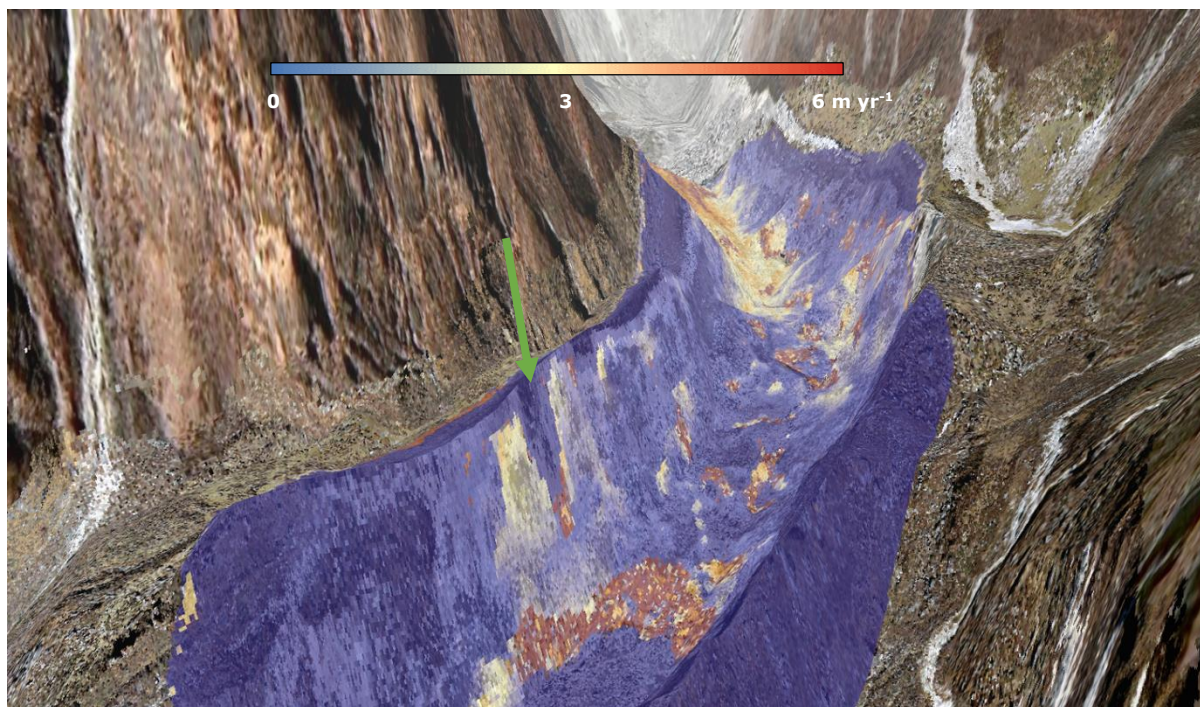


Figure 46, 3D model of the summer displacement, projected with four times vertical exaggeration. The displacements near the lateral moraines are caused by mass movement. The green arrow shows a location of vegetation that prevents mass movement.

Back wasting of cliffs and down wasting of the ice can change the geometry of the glacier causing debris to roll, slide and move (Schomacker 2008). Back wasting undercuts the ice from the debris cover and as a result, the boulders at the top of an ice cliff will fall. They end up at the foot of the cliff and could disappear in lakes creating miscorrelations with similar rocks. Their disappearing results in unrealistic high and false velocities or no correlations at all. A tracking window that is larger than the cliff can solve this problem.

### 6.3.6. Emergence

Ice volume decreases or emerges when ice is flowing towards a stagnant region. Immerzeel et al. (2014) found an elevation increment of 0.5 m ( $1.35 \text{ m a}^{-1}$ ) in the outer bend during the summer period. This emergence velocity corresponds to the decreasing velocities in the longitudinal profile. However, two other factors can contribute to this decrease in velocity. Firstly, ice compression and secondly, losing volume by melting processes. The whole glacier is down wasted with -1.09 m. Assuming that down wasting is heterogeneous at the Lirung glacier, the measured emergence is

reduced by melting. The total emergence velocity would be 1.59 m. The emergence velocity signal could be false, when down wasting process is less in the bend than elsewhere on the glacier. The strength of the emergence signal is also dependent on the vertical error of the DEMs. Naito et al. (1998) estimated that the overall emergence velocity on the Lirung Glacier is  $0.18 \text{ m a}^{-1}$ .

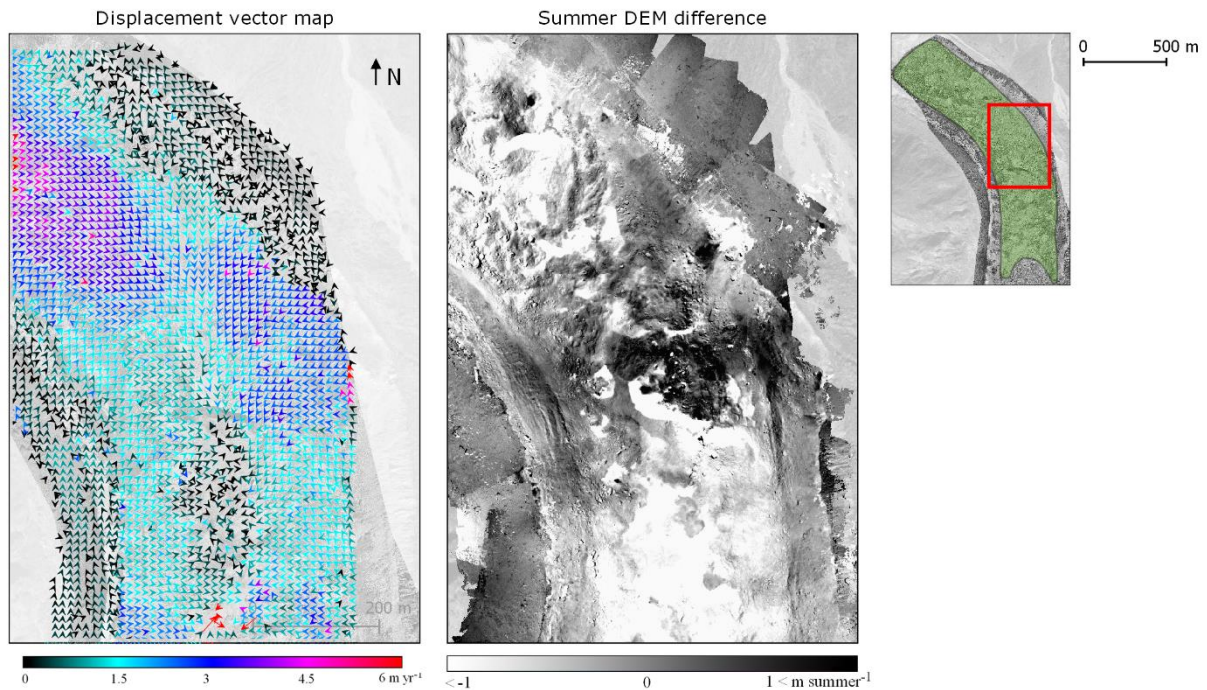


Figure 47, Elevation difference during the summer indicates emergence velocities. The displacement speed and direction support this theory. Based on a 50cm resolution with a step size of 32px

The hypothesis is that the ice in the outer bend is effected by inertia. The ice is decelerated by the increasing drag of the lateral moraine. Ice accumulates in the outer bend, because it is slowed down. A stronger displacement towards the centre of the glacier occurs because the kinetic energy is higher in the elevated bend. The measured flow direction is away from the elevated area, see displacement vectors in Figure 47.

#### 6.4. Summary

The quality of the automated cross-correlations by Cossi-Corr is based on the quality of the input data. The dataset used in this thesis contain optical errors, e.g. offsets and motion blur. The ortho-rectification of parallax created offsets and can be improved by using more ground control points. The parallaxes remain a problem and thus, areas with a high risk on parallax should be clipped out in both SfM and Cossi-Corr processes. Optical blur can cause small errors and is mainly based on the quality of the camera and flight stability. The optical quality of the UAV imagery determines the quality of the displacement maps. The configuration of the cross-correlation is less important. However, with the right settings a choice can be made to create a general flow map or highly detailed map. General flow maps can be used for overall flow research, but feature studies need a high level of detail.

The manually tracked correlation points contain an error. The points are used to estimate the error made by Cosi-Corr. The automated correlation map has more detail, spatial variability and is a full raster, while there are only ~500 manually tracked points. The quality of Cosi-Corr's tracking is more precise because it uses an area to track. The points that are tracked by hand are more sensitive for parallax, blur and user-mistakes.

Basal sliding seems to be the dominant flow regime during the summer. Near the bend, an emergence velocity is probably caused by restraining the flow when the ice moves against the moraine due to inertia. A depression in the magnitude of the displacement can be found to the north of the terminus, but it is yet unknown what factors influence this depression.

## 7. Conclusion

---

In this research, it is investigated whether UAV collected images are suitable inputs for monitoring glacier surface dynamics. This is done in 3 time steps of the debris-covered Lirung glacier in Nepal. The imagery is captured with a UAV in May 2013, Oct 2013 and May 2014. The imagery is processed with the Structure from Motion workflow and is ortho rectified. The outputs are ortho-mosaics and DEMs. They were converted into derivatives in order to use them for automated cross-correlations in Cosi-Corr. A series of manually tracked points is created to estimate the accuracy of the automated outputs and the following conclusions are drawn.

Glacial flow is a complex process that combines internal deformation and basal slide. The centre of the glacier flows faster than near the moraines due to shear stress of the lateral moraines. A similar gradient can be found from the bedrock to the surface, which has larger velocities. Therefore, the velocities at the centre of the surface are not representative for whole glacier velocities. However, with glaciological models, the gradient of velocities can be computed and the correlation maps can be used for calibration.

Overall, the Laplacian Enriched Brightness imagery provides the best optical results and statistics with 0.20 m spatial resolution correlated with a frequency configuration of W256 F64 S16 R2 M0.9. The statistics between the automated and manually correlated points have a correlation coefficient of 0.944 and a slope of the best-fit line of 0.95. This indicates that the automated and manually maps correspond. The cross-correlation algorithm can detect deformations that are smaller than the initial errors of both input images. The individual photographs can be visible in the displacements maps. Different configurations of the frequency correlator do not have a large effect on the magnitude or directions of the surface displacements and therefore, the input UAV imagery is more limiting than Cosi-Corr. The error introduced by the algorithm is relative small compared to the parallax and blur in the UAV photographs.

The general flow pattern is better distinguishable with down sampled spatial resolutions from 0.1 m up to 0.2 m. In this manner noise and optical errors could be reduced. The correlations maps based on the original UAV resolution of 0.1 m contain a fine spatial variation and can be used to

research specific local process. Light aerial vehicles are needed (like UAV or small helicopters) are necessary to capture such detailed imagery.

Summer velocities are twice as high as the winter velocities based on the available dataset of the three images. The average maximum summer velocities are  $5 \text{ m a}^{-1}$  in the northern part of the study area and the glacier is stagnant near the terminus. During the winter, the same area is stagnant but the average maximum drops to  $2.6 \text{ m a}^{-1}$ . The spatial differences in the magnitude of displacement indicate multiple flow regimes. Basal sliding could explain large displacement in the northern part. The amount of water by melt and precipitation lubricate the bedrock and thus increase the basal slide during the summer season.

The error during the summer is up to 0.52 m and 0.28 during the winter. The error is based on a series of ground-truth vectors that are measured by hand. Although the error is relative small compared to the accuracy of UAV imagery, it could be improved with higher optical quality of the imagery. The certainty of the direction of the errors is large because the Angular Errors are often in the order of a few degrees. Ice cliffs, blur and parallax can reduce the certainty of magnitude and direction of the automated correlations.

The flow direction near the moraines is towards the centre of the glacier. This might be caused by the internal shear stress that interacts with the drag of the lateral moraine. Another theory is that the mass of rock avalanches and mass movement pushes the ice away from the moraine.

The terminus itself is barely retreating. However, there is a down waste of  $1.09 \text{ m a}^{-1}$  and thus the glacier is losing mass in time. Emergence velocities might be found below the bend of the glacier. Both magnitude as direction of the displacement confirm this hypothesis. The emergence velocities are caused by a combination of the bend in the glacier and a stagnant area after the bend.

The correlation maps can be used to calibrate mass equations and hydrological models. Back- and down-wasting are difficult to monitor with these correlation maps, but could be useful in combination with in situ measurements.

This study yields insight in small spatial variations in surface displacement and can be translated into glacial flow. To understand true dynamics of debris-cover glaciers more data is needed about energy balances, conduits and bedrock characteristics. UAVs have great potential for researching temporal and spatial variations in surface dynamics and are essential to understand melting behaviour in the Himalayas.

## 8. Recommendations

---

### 8.1. Further research

This is the first time that a glacier is monitored at this spatial scale. The setup of the thesis is mainly methodical, but general physical processes are interpreted. Further research is recommended in improving the method and for interpreting the local processes in depth.

The following recommendations are made for the Cossi-Corrs settings. The best input-data is a Laplacian Enriched Brightness (LEB) image. The Laplacian kernel used is 3x3 cells, computing local edges only. Other Laplacian configurations should be researched and in addition, a combination of a hillshade combination with a LEB is possible. The lack of texture in the hillshade is solved. The hillshade contains new information about the altitude and this might improve correlations with a LEB image.

Smaller focal lengths and thus smaller resolutions ( $<0.1 \text{ m px}^{-1}$ ) during the UAV flights should be considered. This increases the optical quality of the imagery and improves the correlations. The UAV uses a camera with basic RGB channels (400 – 700 nm). Multi- or hyper-spectral cameras could be used. Different band might help with the correlations, because a unique spectral profile of a boulder can be captured. A model that uses a window based on the local predicted displacement would speed up computation. If all surrounding areas have low displacement, the window size could be decreased.

For future flights, the following steps should be considered. Most lenses reach the most sharpness at aperture of F/8.0. It depends on the camera lens, but small focal length causes great distortion, often chromatic aberration and vignette near the borders making some cameras better than others are. Full-frame cameras do have extreme small focal length since they do not have crop factors. The highest possible shutter speed could be calculated by the camera with a fixed aperture and a fixed ISO that is highest acceptable. RAW data photos are better in many ways: it increases the dynamic range, there is no automatic noise reducer, white-balance is not fixed and there is no JPEG compression. Each of these setting is based on the trade-off of quality and light conditions.

### 8.2. Optimal workflow for glacial displacement

The aim of this research is physical geographical based, writing a software packages is not the objective and is too time-consuming. However, the following paragraph is a hypothesis of the ideal workflow for a glacial feature tracker based on a DEM and ortho-rectified imagery.

From the DEM a general flow direction can be derived. Glaciers flow and slide downhill, so any uphill velocities would indicate back wasting or mass movement and they could be neglected if studying the glacial flow. The principle of pyramid layers should decrease the computation time. Pyramid layers are blurred down sampled layers of the original. Every pyramid layer is the previous layer halved. Feature trackers would detect only the major velocities on the glacier in the smallest low-res pyramid layer. In the second-smallest layer, the resolution is twice as big and therefore the velocity measured here are more precise. Since the general velocity is known in the



smallest pyramid layer, a general prediction of the velocity can be made. The search time will drop. The previous velocity gets a small correction and will guide as a general velocity in the third pyramid layer. See for more details [Figure 48](#). This process can be repeated until the desired accuracy of the flow velocity is reached. This already might be before reaching the original high-resolution layer. Stopping computations at a level that already indicate a desired accuracy could decrease computation time as well. When using Laplacian pyramid layers edges at different scales are computed.

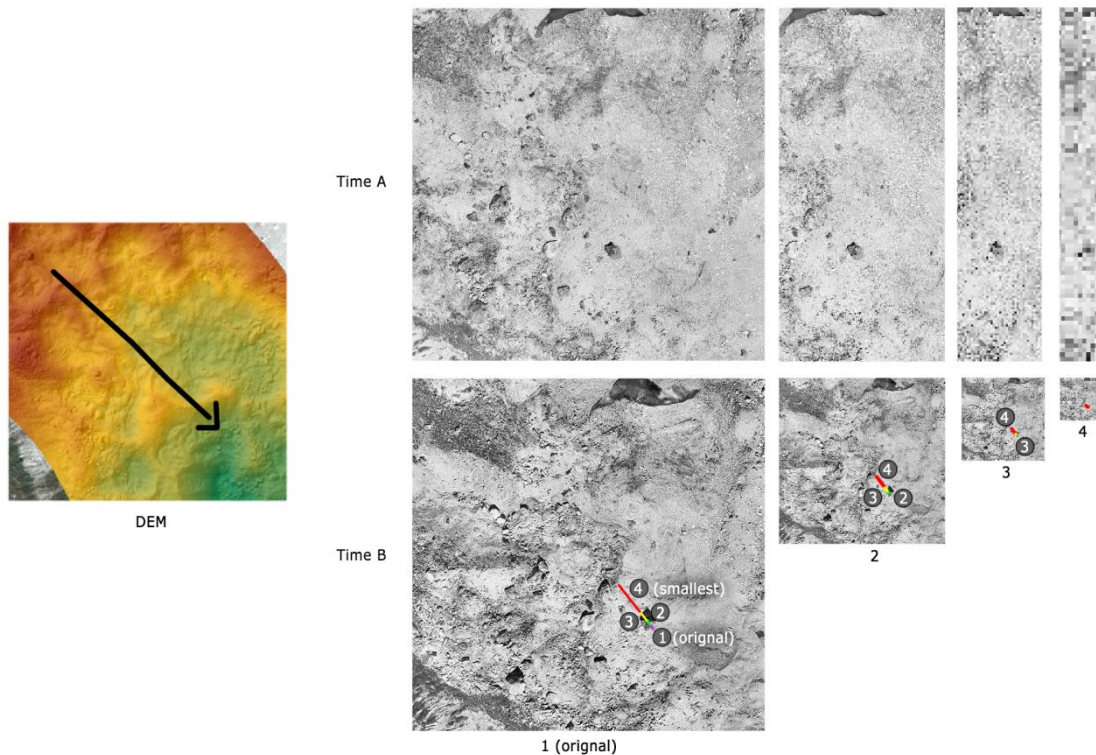


Figure 48 *Left*: With a DEM, a general downhill flow can be determined. *Right*: lower series B show pyramid layers with the same DPI. Every new layer is half of the previous layer and therefore, the details will decrease. The upper series A show the other dataset in pyramid layers but cropped and continuous height dimension. In the lower series, surface deformation is estimated by the lines. Every colour and number is an estimation of a pyramid layer. Red is the *first* estimation of the smallest layer.

### 8.2.1. Feature correspondence

Cosi-Corr works with a moving window. The algorithm tries to correlate every window on the glacier. Another technique is to work only with features. These single point features have a *correspondence* with a feature that is found and linked in another image. In the remote sensing similar process is used with *tie-points*. Features are used a lot in remote sensing, the special effects in movies, computer vision for cameras and robots ([Radke 2012](#)). A feature is one pixel in a unique cluster of pixels that cannot be found anywhere else in the same image. Most of the feature detectors, such as *Harris*, *SIFT*, *Susan*, *FAST*, *LoF* and *DoG*, have all the same principles but differ in the method. They majority work with gradients, where nearby pixels are weighted stronger than distal pixels. There is a difference in feature descriptors and detectors. A descriptor defines a feature and detectors search for suitable features or their correspondence.

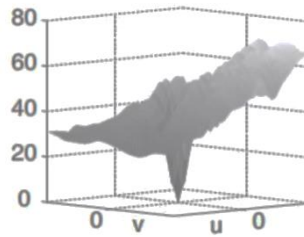


Figure 49, Example of the eigenvalues of a Harris matrix feature. The costs increase enormous when moving out of the origin. This pattern should be unique and have a corresponding pattern in the other image (Radke 2012)

Good features are positioned in contrast rich environments. They are detected on strong gradients in the intensity of the image and thus edges of objects. A straight-line edge has cross-line a strong gradient, but the along-the-line gradient will not change. Therefore, the feature could shift along the line and thus, straight-line edges are not good features. The gradient should be strong in both x and y direction. Sharp corners and blob shapes are often good features. Shadows can give contrast in one image but they can shift during the day, creating false correspondence.

The single-feature workflow lowers the computation time and works better if only a few correlations can be made, like on glaciers with bare ice. Together with the pyramid layers



## 9. References

- Adhikary S., M. Nakawo, K. Seko, B. Shakya. 2000. "Dust Influence on the Melting Process of Glacier Ice : Experimental Results from Lirung Glacier , Nepal Himalayas." *Debris-Covered Glaciers*, no. 264: 43–52. <http://books.google.nl/books?id=ghn8LV2CZ20C>.
- Arnold, N. S., W. G. Rees, B. J. Devereux, and G. S. Amable. 2006. "Evaluating the Potential of High-Resolution Airborne LiDAR Data in Glaciology." *International Journal of Remote Sensing* 27 (6): 1233–51. doi:10.1080/01431160500353817.
- Ayoub, François, Sébastien Leprince, and Lionel Keene. 2009. "User's Guide to COSI-CORR Co-Registration of Optically Sensed Images and Correlation." *Book*, 1–38.
- Barry, Roger G. 2006. "The Status of Research on Glaciers and Global Glacier Recession: A Review." *Progress in Physical Geography* 30 (3): 285–306. doi:10.1191/0309133306pp478ra.
- Bolch, T., a. Kulkarni, a. Kaab, C. Huggel, F. Paul, J. G. Cogley, H. Frey, et al. 2012. "The State and Fate of Himalayan Glaciers." *Science* 336 (6079): 310–14. doi:10.1126/science.1215828.
- Bolch, T., T. Pieczonka, and D. I. Benn. 2011. "Multi-Decadal Mass Loss of Glaciers in the Everest Area (Nepal Himalaya) Derived from Stereo Imagery." *Cryosphere* 5 (2): 349–58. doi:10.5194/tc-5-349-2011.
- Bolch, Tobias, Manfred Buchroithner, Tino Pieczonka, and André Kunert. 2008. "Planimetric and Volumetric Glacier Changes in the Khumbu Himal, Nepal, since 1962 Using Corona, Landsat TM and ASTER Data." *Journal of Glaciology* 54 (187): 592–600. doi:10.3189/002214308786570782.
- Bookhagen, Bodo, and Douglas W. Burbank. 2010. "Toward a Complete Himalayan Hydrological Budget: Spatiotemporal Distribution of Snowmelt and Rainfall and Their Impact on River Discharge." *Journal of Geophysical Research: Earth Surface* 115 (F3): F03019. doi:10.1029/2009JF001426.
- Brox, Thomas, Andrés Bruhn, Nils Papenberg, and Joachim Weickert. 2004. "High Accuracy Optical Flow Estimation Based on a Theory for Warping." *Computer Vision - ECCV 2004* 3024: 25–36. doi:10.1007/978-3-540-24673-2\_3.
- Campbell, Neill D F, George Vogiatzis, Carlos Hernández, and Roberto Cipolla. 2008. "Using Multiple Hypotheses to Improve Depth-Maps for Multi-View Stereo." *Lecture Notes in Computer Science (including Subseries Lecture Notes in Artificial Intelligence and Lecture Notes in Bioinformatics)* 5302 LNCS: 766–79. doi:10.1007/978-3-540-88682-2-58.
- Carabajal, Claudia C., and David J. Harding. 2005. "ICESat Validation of SRTM C-Band Digital Elevation Models." *Geophysical Research Letters* 32 (22): 1–5. doi:10.1029/2005GL023957.
- Cnes. 2013. "Pleiades: A Multi-Missions Concept and a Partnership Program." <http://smc.cnes.fr/PLEIADES/>.
- Copland, L., S. Pope, M.P. Bishop, J.F. Shroder, P. Clendon, Andrew Bush, Ulrich Kamp, Y.B. Seong, and L.a. Owen. 2009. "Glacier Velocities across the Karakoram Himalaya." *Annals Of Glaciology* 50 (52). International Glaciological Society: 1–18. doi:10.3189/172756409789624229.
- Cuffey, k, and W Paterson. 1970. *The Physics of Glaciers*. American Journal of Science. Vol. 269. doi:10.2475/ajs.269.2.191.
- Debella-Gilo, Misganu, and Andreas Käbb. 2011. "Sub-Pixel Precision Image Matching for Measuring Surface Displacements on Mass Movements Using Normalized Cross-Correlation." *Remote Sensing of Environment* 115 (1). Elsevier Inc.: 130–42. doi:10.1016/j.rse.2010.08.012.
- Dowdeswell, Julian a., and Toby J. Benham. 2003. "A Surge of Perseibreen, Svalbard, Examined Using Aerial Photography and ASTER High Resolution Satellite Imagery." *Polar Research* 22 (2): 373–83. doi:10.1111/j.1751-8369.2003.tb00118.x.
- Earth, Solid, The Cryosphere, J Gardelle, and E Berthier. 2013. "Region-Wide Glacier Mass Balances over the Pamir-Karakoram-Himalaya during." *The Cryosphere* 7 (4): 1263–86. doi:10.5194/tcd-7-975-2013.
- Exelis. 2015. "Idl\_Reference." [papers2://publication/uuid/62ED6BAE-786B-40F9-BC34-63B921457915](https://pubs2://publication/uuid/62ED6BAE-786B-40F9-BC34-63B921457915).
- Fountain, a, M Nakao, and C F Raymond. 2000. *Debris-Covered Glaciers: Proceedings of an International Workshop Held at the University of Washington in Seattle, Washington, USA, 13-15 September 2000*. IAHS Publication. IAHS. <http://books.google.nl/books?id=ghn8LV2CZ20C>.
- Fujita, Koji, and Takayuki Nuimura. 2011. "Spatially Heterogeneous Wastage of Himalayan Glaciers." *Proceedings of the National Academy of Sciences of the United States of America* 108 (34): 14011–14. doi:10.1073/pnas.1106242108.
- Fujita, Koji, Ryohei Suzuki, Takayuki Nuimura, and Akiko Sakai. 2008. "Performance of ASTER and SRTM DEMs, and Their Potential for Assessing Glacial Lakes in the Lunana Region, Bhutan Himalaya." *Journal of Glaciology* 54 (185): 220–28. doi:10.3189/002214308784886162.
- Funk, Martin. 2009. "Physics of Glaciers I 651-4101-00 /."
- Gades, A, H. Conway, N Nereson, N Naito, and T Kadota. 2000. "Radio Echo-Sounding through Supraglacial Debris on Lirung and Khumbu Glaciers, Nepal Himalayas." *IAHS Publication* 264 (264): 13–22. <Go to ISI>://000168875400002.
- Girod, Luc. 2012. "The Use of SfM Technologies in Geosciences: MicMac for Geologists."
- Hannachi, a., I. T. Jolliffe, and D. B. Stephenson. 2007. "Empirical Orthogonal Functions and Related Techniques in Atmospheric Science: A Review" 254 (May 2007): 243–54. doi:10.1002/joc.
- Hansen, L, H. 2014. "Ice Crystal Structure." *Centre for Ice and Climate, Niels Bohr Institute*.
- Harper, Joel T., Neil F. Humphrey, W. Tad Pfeffer, Snehalata V. Huzurbazar, David B. Bahr, and Brian C. Welch. 2001. "Spatial Variability in the Flow of a Valley Glacier: Deformation of a Large Array of Boreholes." *Journal of Geophysical Research* 106 (B5). Wiley Online Library: 8547. doi:10.1029/2000JB900440.
- Hatson, Wouter, Els de Roeck, and Els Ducheyne. n.d. "Multi-Temporal UAV Image Processing for Habitat Modeling," 1.

- Heid, T., and a. Kääb. 2012. "Evaluation of Existing Image Matching Methods for Deriving Glacier Surface Displacements Globally from Optical Satellite Imagery." *Remote Sensing of Environment* 118 (March). Elsevier Inc.: 339–55. doi:10.1016/j.rse.2011.11.024.
- Heideman, Michael T., Don H. Johnson, and C. Sidney Burrus. 1985. "Gauss and the History of the Fast Fourier Transform." *Archive for History of Exact Sciences* 34: 265–77. doi:10.1007/BF00348431.
- Heuff, Fionna. 2014. "UNKNOWN." ICIMOD. 2014. "ICIMOD." www.icimod.org.
- Immerzeel, W., Alter W., Ludovicus P H van Beek, and Marc F P Bierkens. 2010. "Climate Change Will Affect the Asian Water Towers." *Science (New York, N.Y.)* 328 (5984): 1382–85. doi:10.1126/science.1183188.
- Immerzeel, W., W., L. Petersen, S. Ragettli, and F. Pellicciotti. 2014. "The Importance of Observed Gradients of Air Temperature and Precipitation for Modeling Runoff from a Glacierized Watershed in the Nepalese Himalayas." *Water Resources Research* 50: 2212–26. doi:10.1002/2013WR014506.
- Immerzeel, W. W., P. D a Kraaijenbrink, J. M. Shea, a. B. Shrestha, F. Pellicciotti, M. F P Bierkens, and S. M. De Jong. 2014. "High-Resolution Monitoring of Himalayan Glacier Dynamics Using Unmanned Aerial Vehicles." *Remote Sensing of Environment* 150 (July). Elsevier Inc.: 93–103. doi:10.1016/j.rse.2014.04.025.
- Immerzeel, Walter W., L. P H van Beek, M. Konz, a. B. Shrestha, and M. F P Bierkens. 2012. "Hydrological Response to Climate Change in a Glacierized Catchment in the Himalayas." *Climatic Change* 110 (3–4): 721–36. doi:10.1007/s10584-011-0143-4.
- Immerzeel, W., W., P. Droogers, S. M. de Jong, and M. F P Bierkens. 2009. "Large-Scale Monitoring of Snow Cover and Runoff Simulation in Himalayan River Basins Using Remote Sensing." *Remote Sensing of Environment* 113 (1). Elsevier Inc.: 40–49. doi:10.1016/j.rse.2008.08.010.
- Jianchu, Xu, Arun Bhakta Shrestha, Ramesh Ananda Vaidya, Mats Eriksson, and Kenneth Hewitt. 2007. "The Melting Himalayas." *Development*. [http://lib.icimod.org/record/26349/files/attachment\\_532.pdf](http://lib.icimod.org/record/26349/files/attachment_532.pdf).
- Juen, M., C. Mayer, a. Lambrecht, H. Han, and S. Liu. 2014. "Impact of Varying Debris Cover Thickness on Ablation: A Case Study for Koxkar Glacier in the Tien Shan." *Cryosphere* 8 (6): 377–86. doi:10.5194/tc-8-377-2014.
- Kääb, a. 2005. "Combination of SRTM3 and Repeat ASTER Data for Deriving Alpine Glacier Flow Velocities in the Bhutan Himalaya." *Remote Sensing of Environment* 94 (4). Elsevier: 463–74. doi:10.1016/j.rse.2004.11.003.
- Kääb, a., and M. Vollmer. 2000. "Surface Geometry, Thickness Changes and Flow Fields on Creeping Mountain Permafrost: Automatic Extraction by Digital Image Analysis." *Permafrost and Periglacial Processes* 11 (September): 315–26. doi:10.1002/1099-1530(200012)11:4<315::AID-PPP365>3.0.CO;2-J.
- Kääb, Andreas. 2005a. "Remote Sensing of Mountain Glaciers and Permafrost Creep." *Schriftenreihe Physische Geographie*.
- . 2005b. "Remote Sensing of Mountain Glaciers and Permafrost Creep." *Schriftenreihe Physische Geographie* 48: 266. <http://scholar.google.com/scholar?hl=en&btnG=Search&q=intitle:Remote+Sensing+of+Mountain+Glaciers+and+Permafrost+Creep#0>.
- Kääb, Andreas, Etienne Berthier, Christopher Nuth, Julie Gardelle, and Yves Arnaud. 2012. "Contrasting Patterns of Early Twenty-First-Century Glacier Mass Change in the Himalayas." *Nature* 488 (7412): 495–98. doi:10.1038/nature11324.
- Lemmens, Mathias. 2011. *Geo-Information: Technologies, Applications and the Environment (Google eBook)*. Springer. [http://books.google.com/books?hl=en&lr=&id=n\\_tUAWYg4UQC&pgis=1](http://books.google.com/books?hl=en&lr=&id=n_tUAWYg4UQC&pgis=1).
- Leprince, Sébastien, Jean-philippe Avouac, Sylvain Barbot, François Ayoub, and Jean-Philippe Avouac. 2007. "Automatic and Precise Orthorectification, Coregistration, and Subpixel Correlation of Satellite Images, Application to Ground Deformation Measurements." *IEEE Transactions on Geoscience and Remote Sensing* 45 (6): 1529–58. doi:10.1109/TGRS.2006.888937.
- Leprince, Sébastien, Sylvain Barbot, François Ayoub, and Jean Philippe Avouac. 2007. "Automatic and Precise Orthorectification, Coregistration, and Subpixel Correlation of Satellite Images, Application to Ground Deformation Measurements." *IEEE Transactions on Geoscience and Remote Sensing* 45 (6): 1529–58. doi:10.1109/TGRS.2006.888937.
- Lim, Sunghyun Lim Sunghyun, Kwang Hoon Sohn Kwang Hoon Sohn, and Chulhee Lee Chulhee Lee. 2001. "Principal Component Analysis for Compression of Hyperspectral Images." *IGARSS 2001. Scanning the Present and Resolving the Future. Proceedings. IEEE 2001 International Geoscience and Remote Sensing Symposium (Cat. No.01CH37217)* 1 (2): 115–23. doi:10.1109/IGARSS.2001.976068.
- Lucieer, a., S. M. D. Jong, and D. Turner. 2014. "Mapping Landslide Displacements Using Structure from Motion (SfM) and Image Correlation of Multi-Temporal UAV Photography." *Progress in Physical Geography* 38 (1): 97–116. doi:10.1177/0309133313515293.
- Mancini, Francesco, Marco Dubbini, Mario Gattelli, Francesco Stecchi, Stefano Fabbri, and Giovanni Gabbianelli. 2013. "Using Unmanned Aerial Vehicles (UAV) for High-Resolution Reconstruction of Topography: The Structure from Motion Approach on Coastal Environments." *Remote Sensing* 5 (12): 6880–98. doi:10.3390/rs5126880.
- Mazzetta, J., Dennis Claude, and Bob Wageneck. 2005. "Digital Camera Imaging Evaluation." *Electro Optical Industries*, 13.
- Messerli, a., and a. Grinsted. 2014. "Image GeoRectification And Feature Tracking Toolbox: ImGRAFT." *Geoscientific Instrumentation, Methods and Data Systems Discussions* 4 (2): 491–513. doi:10.5194/gid-4-491-2014.
- Mihalcea, Claudia, Christoph Mayer, Guglielmina Diolaiuti, Astrid Lambrecht, Claudio Smiraglia, and Gianni Tartari. 2006. "Ice Ablation and Meteorological Conditions on the Debris-Covered Area of Baltoro Glacier, Karakoram, Pakistan." *Annals of Glaciology* 43 (1): 292–300. doi:10.3189/172756406781812104.

- Mishra, A. 2010. "Assessment of Water Quality Using Principal Component Analysis: A Case Study of the River Ganges." *Journal of Water Chemistry and Technology*. doi:10.3103/S1063455X10040077.
- Molnia, Bruce F. 2013. "Glossary of Glacier Terminology: A Glossary Providing the Vocabulary Necessary to Understand the Modern Glacier Environment." *Open-File Report 2004-1216*. <http://pubs.usgs.gov/of/2004/1216/>.
- Naito, N, M Nakawo, and T Aoki. 1998. "Topographical Map of the Ablation Area of the Lirung Glacier in the Langtang Valley, Nepal Himalaya." *Bulletin of Glacier Research*. 16. Japanese Society of Snow and Ice: 19-31.
- Naito, Nozomu, Tsutomu Kadota, Koji Fujita, Akiko Sakai, and Masayoshi Nakawo. 2002. "Surface Lowering over the Ablation Area of Lirung Glacier, Nepal Himalaya." *Bulletin of Glacier Research*.
- Nicholson, Lindsey, and Douglas I. Benn. 2006. "Calculating Ice Melt beneath a Debris Layer Using Meteorological Data." *Journal of Glaciology* 52 (178): 463-70. doi:10.3189/172756506781828584.
- Niethammer, U., M. R. James, S. Rothmund, J. Travelletti, and M. Joswig. 2012. "UAV-Based Remote Sensing of the Super-Sauze Landslide: Evaluation and Results." *Engineering Geology* 128 (March). Elsevier B.V.: 2-11. doi:10.1016/j.enggeo.2011.03.012.
- NSIDC. 2006. "IMCORR Software." <http://nsidc.org/data/velmap/imcorr.html>.
- Nuimura, Takayuki, Koji Fujita, Satoru Yamaguchi, and Rishi R. Sharma. 2012. "Elevation Changes of Glaciers Revealed by Multitemporal Digital Elevation Models Calibrated by GPS Survey in the Khumbu Region, Nepal Himalaya, 1992-2008." *Journal of Glaciology* 58 (210): 648-56. doi:10.3189/2012JoG11J061.
- Nye, J F. 1952. "The Mechanics of Glacier Flow." *Journal of Glaciology*, no. 11: 82-93.
- Nye, J. F. 1965. "The Flow of a Glacier in a Channel of Rectangular, Elliptic or Parabolic Cross-Section." *J. Glaciol.* 5 (41): 661-90.
- Östrem, G. 1959. "Ice Melting under a Thin Layer of Moraine, and the Existence of Ice Cores in Moraine Ridges." *Geografiska Annaler* 41 (4): 228-30. doi:10.2307/4626805.
- Pierrot-Deseilligny, Marc and Paparoditis, Nicolas. 2006. "A Multiresolution and Optimization-Based Image Matching Approach: An Application to Surface Reconstruction from SPOT 5-HRS Stereo Imagery." *ISPRS Workshop on Topographic Mapping from Space*. [http://www.isprs.org/proceedings/XXXVI/1-W41/makaleler/Pierrot\\_multiresolution\\_matching.pdf](http://www.isprs.org/proceedings/XXXVI/1-W41/makaleler/Pierrot_multiresolution_matching.pdf).
- Plets, GertjanGheyle WouterVerhoeven GeertDe Reu JeroenBourgeois JeanVerhegge JeroenStichelbaut BirgerCarver Martin. 2012. "Three-Dimensional Recording of Archaeological Remains in the Altai Mountains." *Antiquity* 86: 884-97. <http://libpublic3.library.isu.edu/login?url=http://search.ebscohost.com/login.aspx?direct=true&db=rlh&AN=79856185&site=ehost-live>.
- Quincey, D. J., M. Braun, N. F. Glasser, M. P. Bishop, K. Hewitt, and a. Luckman. 2011. "Karakoram Glacier Surge Dynamics." *Geophysical Research Letters* 38 (18): n/a - n/a. doi:10.1029/2011GL049004.
- Quincey, D. J., and N. F. Glasser. 2009. "Morphological and Ice-Dynamical Changes on the Tasman Glacier, New Zealand, 1990-2007." *Global and Planetary Change* 68 (3). Elsevier B.V.: 185-97. doi:10.1016/j.gloplacha.2009.05.003.
- Racoviteanu, Adina E., Mark W. Williams, and Roger G. Barry. 2008. "Optical Remote Sensing of Glacier Characteristics: A Review with Focus on the Himalaya." *Sensors* 8 (5). Molecular Diversity Preservation International: 3355-83. doi:10.3390/s8053355.
- Radke, Richard J. 2012. *Computer Vision for Visual Effects*. Cambridge.
- Redpath, T a N, P Sirguey, S J Fitzsimons, and a Kääb. 2013. "Remote Sensing of Environment Accuracy Assessment for Mapping Glacier Flow Velocity and Detecting Flow Dynamics from ASTER Satellite Imagery: Tasman Glacier, New Zealand." *Remote Sensing of Environment* 133: 90-101. doi:10.1016/j.rse.2013.02.008.
- Reichenbach, Stephen E., and Frank Geng. 2003. "Two-Dimensional Cubic Convolution." *IEEE Transactions on Image Processing* 12: 857-65. doi:10.1109/TIP.2003.814248.
- Reznichenko, Natalya, Tim Davies, James Schulmeister, and Mauri McSaveney. 2010. "Effects of Debris on Ice-Surface Melting Rates: An Experimental Study." *Journal of Glaciology* 56 (197): 384-94. doi:10.3189/002214310792447725.
- Rikiishi, Kunio, and Haruka Nakasato. 2006. "Height Dependence of the Tendency for Reduction in Seasonal Snow Cover in the Himalaya and the Tibetan Plateau Region, 1966-2001." *Annals of Glaciology* 43: 369-77. doi:10.3189/172756406781811989.
- Rippin, David, Ian Willis, Neil Arnold, Andrew Hodson, John Moore, Jack Kohler, and Helgi Björnsson. 2003. "Changes in Geometry and Subglacial Drainage of Midre Lovénbreen, Svalbard, Determined from Digital Elevation Models." *Earth Surface Processes and Landforms* 28 (3): 273-98. doi:10.1002/esp.485.
- Rosu, Ana-Maria Maria, Marc Pierrot-Deseilligny, Arthur Delorme, Renaud Binet, and Yann Klinger. 2014. "Measurement of Ground Displacement from Optical Satellite Image Correlation Using the Free Open-Source Software MicMac." *ISPRS Journal of Photogrammetry and Remote Sensing*, April. International Society for Photogrammetry and Remote Sensing, Inc. (ISPRS). doi:10.1016/j.isprsjprs.2014.03.002.
- Sakai, a, K Fujita, T Aoki, K Asahi, and M Nakawo. 1997. "Water Discharge from the Lirung Glacier in Langtang Valley, Nepal Himalayas, 1996." *Bulletin of Glacier Research* 15: 79-83.
- Sakai, a., K. Fujita, and J. Kubota. 2004. "Evaporation and Percolation Effect on Melting at Debris-Covered Lirung Glacier, Nepal Himalayas, 1996." *Bulletin of Glaciological Research* 21: 9-15.
- Sakai, a., M. Nakawo, and K. Fujita. 2002. "Distribution Characteristics and Energy Balance of Ice Cliffs on Debris-Covered Glaciers, Nepal Himalaya." *Arctic, Antarctic, and Alpine Research*, no. 1: 12-19. doi:10.2307/1552503.
- Scambos, Theodore a., Melanie J. Dutkiewicz, Jeremy C. Wilson, and Robert a. Bindshadler. 1992. "Application of Image Cross-Correlation to the Measurement of Glacier Velocity Using Satellite Image

- Data." *Remote Sensing of Environment* 42 (September 1991): 177–86. doi:10.1016/0034-4257(92)90101-O.
- Scherler, Dirk, Bodo Bookhagen, and Manfred R. Strecker. 2011. "Spatially Variable Response of Himalayan Glaciers to Climate Change Affected by Debris Cover." *Nature Geoscience* 4 (1). Nature Publishing Group: 156–59. doi:10.1038/ngeo1068.
- Scherler, Dirk, Sébastien Leprince, and Manfred R. Strecker. 2008. "Glacier-Surface Velocities in Alpine Terrain from Optical Satellite Imagery-Accuracy Improvement and Quality Assessment." *Remote Sensing of Environment* 112: 3806–19. doi:10.1016/j.rse.2008.05.018.
- Schomacker, Anders. 2008. "What Controls Dead-Ice Melting under Different Climate Conditions? A Discussion." *Earth-Science Reviews* 90 (3-4). Elsevier B.V.: 103–13. doi:10.1016/j.earscirev.2008.08.003.
- SenseFly. 2014. *eMotion 2.3.0*. Cheseaux-Lausanne. <https://www.sensefly.com/operations/flight-planning-control.html>.
- Siebert, S., J. Burke, J. M. Faures, K. Frenken, J. Hoogeveen, P. Döll, and F. T. Portmann. 2010. "Groundwater Use for Irrigation - A Global Inventory." *Hydrology and Earth System Sciences* 14 (10): 1863–80. doi:10.5194/hess-14-1863-2010.
- Stone, H.S. 1966. "R66-50 An Algorithm for the Machine Calculation of Complex Fourier Series." *IEEE Transactions on Electronic Computers* EC-15. doi:10.1109/PGEC.1966.264428.
- Sun, Deqing, Stefan Roth, and Michael J. Black. 2010. "Secrets of Optical Flow Estimation and Their Principles." *Proceedings of the IEEE Computer Society Conference on Computer Vision and Pattern Recognition*, June. Ieee, 2432–39. doi:10.1109/CVPR.2010.5539939.
- Sund, M., T. R. Lauknes, and T. Eiken. 2014. "Surge Dynamics in the Nathorstbreen Glacier System, Svalbard." *The Cryosphere* 8 (5): 623–38. doi:10.5194/tc-8-623-2014.
- Szeliski, Richard. 2010. *Computer Vision: Algorithms and Applications*. Springer.
- Techradar. 2014. "Canon IXUS 125 HS Review." <http://www.techradar.com/reviews/cameras-and-camcorders/cameras/compact-cameras/canon-ixus-125-hs-1071065/review>.
- Thévenaz, Philippe, Thierry Blu, and Michael Unser. 2000. "Interpolation Revisited." *IEEE Transactions on Medical Imaging* 19 (7): 739–58. doi:10.1109/42.875199.
- Triggs, Bill, Philip F. McLauchlan, Richard I. Hartley, and Andrew W. Fitzgibbon. 2000. "Bundle Adjustment — A Modern Synthesis Vision Algorithms: Theory and Practice." *Vision Algorithms: Theory and Practice* 1883: 153–77. doi:10.1007/3-540-44480-7\_21.
- Turner, Darren, Arko Lucieer, and Christopher Watson. 2012. "An Automated Technique for Generating Georectified Mosaics from Ultra-High Resolution Unmanned Aerial Vehicle (UAV) Imagery, Based on Structure from Motion (SfM) Point Clouds." *Remote Sensing* 4: 1392–1410. doi:10.3390/rs4051392.
- Uppala, S.M., P. W. Kållberg, a. J. Simmons, U. Andrae, V. Da Costa Bechtold, M. Fiorino, J. K. Gibson, et al. 2005. "The ERA-40 Re-Analysis." *QUARTERLY JOURNAL OF THE ROYAL METEOROLOGICAL SOCIETY* 131 (612): 2961–3012. doi:10.1256/qj.04.176.
- Vaughan, D.G., J.C. Comiso, I. Allison, J. Carrasco, G. Kaser, R. Kwok, P. Mote, et al. 2013. "Observations: Cryosphere." *Climate Change 2013: The Physical Science Basis. Contribution of Working Group I to the Fifth Assessment Report of the Intergovernmental Panel on Climate Change*, 317–82. doi:10.1017/CBO9781107415324.012.
- Vogel, C., a. Bauder, and K. Schindler. 2012. "Optical Flow for Glacier Motion Estimation." *ISPRS Annals of Photogrammetry, Remote Sensing and Spatial Information Sciences* 1-3: 359–64. doi:10.5194/isprsannals-1-3-359-2012.
- Wagnon, P., C. Vincent, Y. Arnaud, E. Berthier, E. Vuillermoz, S. Gruber, M. Ménégoz, et al. 2013. "Seasonal and Annual Mass Balances of Mera and Pokalde Glaciers (Nepal Himalaya) since 2007." *Cryosphere* 7 (6): 1769–86. doi:10.5194/tc-7-1769-2013.
- Weertman, J. 1957. "On the Sliding of Glaciers." *Journal of Glaciology* 3: 33–38. doi:10.1007/978-94-015-8705-1\_19.
- Weingartner, Rolf, and Bruno Messerli. 2003. "Assessing the Hydrological Significance of the World ' S Mountains." *Mountain Research and Development* 23 (1): 32–40. doi:http://dx.doi.org/10.1659/0276-4741(2003)023[0032:ATHSOT]2.0.CO;2.
- Whitehead, K, B J Moorman, and C H Hugenholtz. 2013. "Photogrammetry for Glaciological Measurement." *The Cryosphere Discussions* 7 (3): 3043–57. doi:10.5194/tcd-7-3043-2013.
- Winiger, M., M. Gumpert, and H. Yamout. 2005. "Karakorum-Hindukush-Western Himalaya: Assessing High-Altitude Water Resources." *Hydrological Processes* 19 (12): 2329–38. doi:10.1002/hyp.5887.
- World Glacier Monitoring Service. 2008. "Global Glacier Changes : Facts and Figures." <http://www.grid.unep.ch/glaciers/>.
- Xu, Jianchu, R. Edward Grumbine, Arun Shrestha, Mats Eriksson, Xuefei Yang, Yun Wang, and Andreas Wilkes. 2009. "The Melting Himalayas: Cascading Effects of Climate Change on Water, Biodiversity, and Livelihoods." *Conservation Biology* 23 (3): 520–30. doi:10.1111/j.1523-1739.2009.01237.x.
- Yaseen, Muhammad. 2009. "Evaluation of Optical Images Sub-Pixel Correlation for Estimating Ground Deformation Evaluation of Optical Images Sub-Pixel Correlation for Estimating Ground Deformation by."
- Zarco-Tejada, P. J., V. González-Dugo, and J. a J Berni. 2012. "Fluorescence, Temperature and Narrow-Band Indices Acquired from a UAV Platform for Water Stress Detection Using a Micro-Hyperspectral Imager and a Thermal Camera." *Remote Sensing of Environment* 117 (February). Elsevier Inc.: 322–37. doi:10.1016/j.rse.2011.10.007.
- Zemp, M. 2007. "Glaciers and Ice Caps." *UNEP: Global Outlook for Ice and Snow*, 115–52. doi:10.1017/CBO9780511977947.005.

## Appendix A, Glacier terminology

---

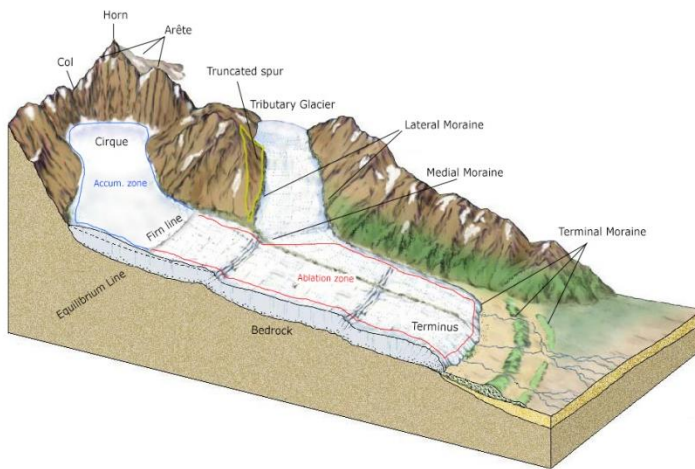


Figure 50, Glacier terminology, Image adapted, originally copyrights Prentice Hall

**Snow, Firn and Glacial Ice** - Snow consist of flakes. Firn is partly melted and refrozen snow. Glacial ice is most compact and contains trapped air. They form in this order and can take years.

**Terminus / Toe / End / Snout** - The lower-most edge of a glacier. It is the front near the foot at any given point in time.

**Firn line / snow line** - Above this line, the firn is visible and not melted away

**Accumulation zone** - The zone where mass is gained by precipitation, Aeolian transport or avalanches

**Ablation zone** - The zone where mass is lost by melting, evaporation, sublimation, Aeolian transport and calving causes mass loss,

**Equilibrium Line Altitude / ELA** - At this theoretical cross-glacial line, the mass gain equals mass loss.

**Crevasses** - Cracks in the softer and less compact top layer of the glacier. They are formed by shear stresses. Longitudinal, marginal and cross glaciers crevasses exists.

**Outwash plain** - This is the place where fluvial processes of melt water play a role. Sometimes flatten out due to the morphodynamics of the stream in combination with former glacial sediments.

**Till** - Unsorted and unstratified accumulation of glacial sediment, deposited directly by glacier ice. This happens by melting (wash out till) or moving ice (lodgement till)

**Bergschrund** - One or more parallel crevasses that develop at the head of a glacier when the ice pulls away from the bedrock wall. In summer, it opens while in the winter it will fill up again.

**Lateral Moraine** - A sediment ridge, located on a glacier surface adjacent to the valley walls. It is formed by rock fall onto the glacier.

**Medial Moraine** - A sediment ridge, located on exposed ice surface in the middle of the glacier parallel to the flow. It forms by joining two lateral moraines of two glaciers.

**Terminal Moraine / End Moraine** - A sediment ridge, cross valley, that is formed at the farthest point reached by the terminus of an advancing glacier.

**Recessional Moraine** - A sediment ridge, cross-valley, that is formed at the terminus of a retreating glacier but was stagnant for a period of time, sufficient for accumulation of sediment

**Surroundings**

**Cirque** - Bowl-shaped amphitheatre-like depression and is often positioned near summits at the head or side of the glacier.

**Tarn** - A lake formed in the basin of a cirque. Generally after melting of the glacier

**Horn / Pyramidal peak** - Sharp pointed peak formed by glacial erosion. They have a typical pyramidal shape and often connected by three or more arêtes/cirques. Four symmetrical faces make it a Matterhorn

**Arêtes** - Sharp jagged narrow ridge between two valleys or cirques. Ending either in a horn or at a truncated spur.

**Col** - Lowest point on an arête between two horns.

**Tributary glacier** - A glacier that is merging together with the main glacier. Often they are smaller and less thick.

**Truncated spurs** - A triangle shape at the end of an arête that is eroded by another glacier. It is a cross-section-like face of an arête of a tributary glacier.

Definitions derived from USGS ([2004](#))



# Appendix B, IDL model

```
; ----- Glacial_Motion_Flow -----
;
;
; Glacial surface optical motion tracker based on Cosi-Corr
; Copyrights by S.W. Meijer, Utrecht University
; Version 1, November, 2014, Meijer
;
; ENVI Classic must be running and linked to IDL (ENVI+IDL.exe)
; Tested with Cosi-Corr build nov 2014
;
; INPUTS: Pre-event file, Post-event file, Visual measured map and/or points in NtoS file and EtoW file,
; OUTPUTS: NtoS file, EtoW file, Intensity map, Vector Map, Overview plot, CSV file

; Comments
; p_ Points (and L_ for lines)
; v_ Visual
; e_ Error
; i_ full Image (every pixel)
; NtoS North to South
; EtoW East to west
; Intens Intensity (Velocity)

; ----- INPUTS -----
;

TEST      = 0 ; TEST MODE; l=on, no CosiCorr, ENVI classic must be running
CALC      = 1 ; Set RUNS lower for testing
period    = 2 ; Monsoon=1 Dryseason=2 Year=3
overview  = 0 ;
Statisticplot= 0 ;
vectorplot= 1 ;
savefiles = 0 ;
mask      = 0 ; SNR and Velocity mask
scatterplot= 0 ; Create Scatterplot full image
SNRratio  = 0.9 ; Signal to Noise ratio threshold
Maxvelocity= 6 ; Max velocities in Histogram and plot (+- 6 m/a Monsoon)

Folder    = 'E:\9_Thesis\' ; Working Directory
;Folder   = 'I:\9_Thesis\' ; Working Directory HDD OVERRULE
txtfile   = 'E:\Dropbox\Thesis\4_Data\runs.csv' ; CSV output file
;txtfile  = 'E:\9_Sander\Dropbox\Thesis\4_Data\runs.csv' ; CSV output file OVERRULE

; Loop inputs
corr_array = ['frequency','frequency','frequency'] ; statistic or frequency
;Both correlations
windowarray = ['256' , '256' , '256' ] ; >2* max velocity (~128/256px for 15 pixel displacement)
steparray   = ['16' , '16' , '16' ] ; determens resolution, LOW = high-res+ slow.
;Frequency
windowarrayF= ['64' , '128' , '64' ] ; For second subpixel estimation. 32 or 64
robustarray = ['2' , '2' , '2' ] ; Low differences. (Some in SNR)
maskarray   = ['0.90' , '0.9' , '0.8' ] ; Low mask gives peak in low velocities. Keep High.
;Statistics
seacharray  = ['20' , '20' , '20' ] ; Size where to search

if period eq 1 then begin
Project = 'Monsoon' ; Period in string (name)
Days = JULDAY(10,22,2013) $ ; May '13 to Okt '13
- JULDAY(05,18,2013) ;
;samplepoints = 'E:\Dropbox\Thesis\4_Data\L_A_V7.csv' ; CSV file with visual measured motion
;samplepoints = 'E:\9_Sander\Dropbox\Thesis\4_Data\L_A_V7.csv' ; CSV file with visual measured motion OVERRULE
v_NtoS_file = Folder+'2_DATA\V_A_NTOS_V5.tif' ; reference image
v_EtoW_file = Folder+'2_DATA\V_A_ETOW_V5.tif' ; reference image
Maxvelocity = 6
endif

if period eq 2 then begin
Project = 'Dry_Season' ; Period in string (name)
Days = JULDAY(05,1,2014) $ ; Okt '13 to May '14
- JULDAY(10,22,2013) ;
;samplepoints = 'E:\Dropbox\Thesis\4_Data\L_BC_V8.csv' ; CSV file with visual measured motion
;samplepoints = 'E:\9_Sander\Dropbox\Thesis\4_Data\L_BC_V8.csv' ; CSV file with visual measured motion OVERRULE
v_NtoS_file = Folder+'2_DATA\V_BC_NTOS_V5.tif' ; reference image
v_EtoW_file = Folder+'2_DATA\V_BC_ETOW_V5.tif' ; reference image
Maxvelocity = 4
endif

if period eq 3 then begin
Project = 'Year' ; Period in string (name)
Days = JULDAY(05,1,2014) $ ; Okt '13 to May '14
- JULDAY(05,18,2013) ;
;samplepoints = 'E:\Dropbox\Thesis\4_Data\L_BC_V8.csv' ; CSV file with visual measured motion
;samplepoints = 'E:\9_Sander\Dropbox\Thesis\4_Data\L_BC_V8.csv' ; CSV file with visual measured motion OVERRULE
v_NtoS_file = Folder+'2_DATA\V_BC_NTOS_V5.tif' ; reference image
v_EtoW_file = Folder+'2_DATA\V_BC_ETOW_V5.tif' ; reference image
Maxvelocity = 5
endif

;TYPE OF DATA
MasterInput = [Folder+'2_DATA\RAWS\Deform_NO.TIF' , Folder+'2_DATA\RAWS\Deform_NO.TIF' , Folder+'2_DATA\RAWS\Deform_NO.TIF' ]
SlaveInput = [Folder+'2_DATA\RAWS\DeformEtoW.TIF' , Folder+'2_DATA\RAWS\DeformNtoS.TIF' , Folder+'2_DATA\RAWS\DeformEtoW.TIF']
;SlaveInput = [Folder+'2_DATA\RAWS\C.tif' , Folder+'2_DATA\RAWS\C.tif' , Folder+'2_DATA\RAWS\C.tif']
MasterInput = [Folder+'2_DATA\RAWS\BC.tif' , Folder+'2_DATA\RAWS\BC.tif' , Folder+'2_DATA\RAWS\BC.tif' ] ;
SlaveInput = [Folder+'2_DATA\RAWS\C.tif' , Folder+'2_DATA\RAWS\C.tif' , Folder+'2_DATA\RAWS\C.tif']

; ----- BEGIN LOOP -----
time = SYSTIME(0) ; Currtent time code
timesseconds = Systeime(1)
runs = size(MasterInput, /N_ELEMENTS) ; Number of runs
RUNS = (CALC GT 0) ? CALC : RUNS ; Override number of runs
s = ' '
for i=0,runs-1 DO BEGIN
mid_time = Systeime(1)& print, s&print, s&print, s

; ----- INITIALS -----
;
;
start_time = Systeime(1) ; Start time per loop
masterimg = MasterInput(i) ; Pre-Event
slaveimg = SlaveInput(i) ; Post-Event
type_Corr = corr_array(i) ; statistic or frequency
griddedout = '0' ; Grided Output (should be set to zero) if stacked
Resampling = '0' ; For Noisy sub-pixel detection
```

```

Windowsize = windowarray(i) ; Half window size
Stepsize = steparray(i) ; Step size
Searchwindow= seacharray(i) ; Search Window
windowsizeX = windowarray(i) ; Initial window size
windowsizeXF= windowarrayF(i) ; Final window size
windowsizeY = windowarray(i) ; Initial window size
windowsizeYF= windowarrayF(i) ; Final window size
robustiter = robustarray(i) ; Robustness Iteration
maskthreshld= maskarray(i) ; Mask Threshold

;type_Corr = 'frequency';corr_array(i) ; statistic or frequency
;griddedout = '0' ; Gridded Output (should be set to zero) if stacked
;Resampling = '0' ; For Noisy sub-pixel detection
;Windowsize = windowarray(i) ; Half window size
;Stepsize = '16';steparray(i) ; Step size
;Searchwindow= seacharray(i) ; Search Window
;windowsizeX = '128';windowarray(i) ; Initial window size
;windowsizeXF= '64';windowarrayF(i) ; Final window size
;windowsizeY = '128';windowarray(i) ; Initial window size
;windowsizeYF= '64';windowarrayF(i) ; Final window size
;robustiter = '2';robustarray(i) ; Robustness Iteration
;maskthreshld= '0.95';maskarray(i) ; Mask Threshold

;
;
;----- File Names -----
;
CD, Folder+'1_RUNS\' ; Working Directory
MAP = STRMID (Time,8,2)+' '+STRMID (time,4,3)+$ ; Project Name
' Run '+STRMID (time,11,2)+STRMID (time,14,1)+'0' ;
IF test EQ 0 THEN BEGIN ;
FILE_MKDIR, MAP & CD, Folder+'1_RUNS\'+MAP ; Create new map, when test=0
ENDIF ;
Typedata=STRMID (STREX (mastering (0), '[a-zA-Z0-9_]'+$), $ ;
/EXTRACT),1,5) ; Type of dataset
filename= Project+'_'+Typedata ; Cosi-Corr output filename
;
;
;----- Statistics -----
;
; Statistic = the statistic input of Cosi-corr ; e.g statistic 32 32 16 16 7 7 1
; Name of the run including the input values ;
IF type_Corr EQ 'statistic' THEN BEGIN ;
statistic = type_Corr+s+Windowsize+s+Windowsize+s+$ ; statistic input
Stepsize+s+Stepsize+s+Searchwindow+s+Searchwindow+$ ;
s+griddedout ;
name = Typedata+s+'S: Window:'+$ ;
Windowsize+' Step:'+Stepsize+' Search:'+Searchwindow ;
ENDIF ELSE BEGIN ;
statistic = type_Corr+s+windowsizeX+s+windowsizeY+s+ $ ; statistic input
windowsizeXF+s+windowsizeYF+s+Stepsize+s+Stepsize+$ ;
s+robustiter+s+maskthreshld+s+Resampling+s+$ ;
griddedout & name=Typedata+s+'F: W'+windowsizeX+' F'+$ ;
windowsizeXF+' S'+Stepsize+' R'+robustiter+' M'+$ ;
maskthreshld & ENDELSE ;
;
;
;----- Creating Files -----
;
IF test EQ 0 THEN BEGIN ; Create 4 input .txt files for Cosi-Corr
filename='master.txt'%OPENW,1,filename=PRINTF,1,masterimg%CLOSE,1 ;
filename='slave.txt'%OPENW,2,filename=PRINTF,2,slaveimg%CLOSE,2 ;
filename='correlations.txt'%OPENW,3,filename=PRINTF,3,statistics%CLOSE,3 ;
filename='output.txt'%OPENW,4,filename=PRINTF,4,filename%CLOSE,4% ENDF ;
;
;
;----- Processing -----
;
;
;----- Cosi Corr -----
;
print, '% -----'+STRCOMPRESS (string(i+1))+ ' Run: '+name+ ' -----' ; e.g. % ----- 1 run: ortho Stat. Window:64 StepSearch:10px -----
IF test EQ 0 THEN BEGIN ; Cosi-Corr batch, ENVI classic and Cosi-Corr must running
cosi_batch_correlation, 'master.txt', 'slave.txt', CORR='correlations.txt', OUT='output.txt', NO_OPEN=1
elapsed_time = Systemtime (1) - start time & IF elapsed_time LE '60' THEN print, '% Duration Cosi-Corr: '+ STRCOMPRESS (string ($
round (elapsed_time)))+'sec' ELSE print, '% Duration Cosi-Corr: '+ STRCOMPRESS (string (round (elapsed_time/60)))+'min'
;
;
;----- Re-open image -----
;
ENVI_OPEN_FILE, filename, r_fid=fid, NO_REALIZE=1 ; Reload image in IDL
ENVI_FILE_QUERY, fid, dims=dims, nl=nlines, ns=nrows ; Retrieve header info
proj = ENVI_GET_MAP_INFO (FID = fid) ; Get Projection
EtoW = ENVI_GET_DATA (fid=fid, dims=dims, pos=0) ; East to West band
NtoS = ENVI_GET_DATA (fid=fid, dims=dims, pos=1) ; North to South band
SNR = ENVI_GET_DATA (fid=fid, dims=dims, pos=2) ; Signal 2 Noise band
EtoW = reverse (EtoW,2) ;
NtoS = reverse (NtoS,2) ;
SNR = reverse (SNR,2) ;
ENVI_OPEN_FILE, mastering, r_fid=fid2, NO_REALIZE=1 ;
ENVI_FILE_QUERY, fid2, dims=dims2 ; Open Original
ORIGINAL = ENVI_GET_DATA (fid=fid2, dims=dims2, pos=0) ;
ENVI_OPEN_FILE, v_NtoS_file, r_fid=fid3, NO_REALIZE=1 ;
ENVI_FILE_QUERY, fid3, dims=dims3, nl=v_nlines, ns=v_nrows ; Open Visual North to South
v_NtoS = ENVI_GET_DATA (fid=fid3, dims=dims3, pos=0) ;
ENVI_OPEN_FILE, v_EtoW_file, r_fid=fid3, NO_REALIZE=1 ;
ENVI_FILE_QUERY, fid3, dims=dims3 ; Open Visual East to West
v_EtoW = ENVI_GET_DATA (fid=fid3, dims=dims3, pos=0) ;
v_proj = ENVI_GET_MAP_INFO (FID = fid3) ; Get Projection
points = READ_CSV (samplepoints, HEADER=SedHeader) ;
SAVE, /VARIABLES, FILENAME='variables'+string (i,format='(I0)')+'.sav' ; To work later without ENVI classic
;
ENDIF ;
;
a='
a='
a='----- Post processing -----
a='
a='
print, '% Start post-processing' & mid time = Systemtime (1)
IF test EQ 1 THEN BEGIN
; If the run is a test open the old data to test run without Cosi-Corr & and tweak some parameters
RESTORE, Folder+'1_RUNS\09_Feb_Run_1440\variables'+string (i,format='(I0)')+'.sav'
CD, Folder+'1_RUNS\09_Feb_Run_1440\'
TEST = 1
; SNRratio = 0.9 ; !!!
runs = 1 ; !!!
overview = 0 ;
Statisticplot = 0 ;
vectorplot = 1 ;
savefiles = 0 ;
mask = 0 ;
scatterplot = 0 ;

```

```

; maxvelocity = 6;
ENDIF

; ----- Basics -----
empty = make_array(nrows,nlines, value=0) ; Create null image
ROIpercent = N_ELEMENTS(WHERE(ORIGINAL NE ORIGINAL(1), /NULL))/ $ ; Percentage pixels contain data
; (float(N_ELEMENTS(WHERE(ORIGINAL EQ ORIGINAL(1), /NULL)))+$
; N_ELEMENTS(WHERE(ORIGINAL NE ORIGINAL(1), /NULL)))
; Monsoon case ~0.49%
; Change velocity from per period to per year
EtoW = (EtoW/float(DAYS))*365.0
NtoS = (NtoS/float(DAYS))*356.0
v_NtoS = (v_NtoS/DAYS)*365
v_EtoW = (v_EtoW/DAYS)*365
; Remove NAN infinity
SNR = [WHERE(FINITE(SNR, /NAN), /NULL)] = 0
EtoW = [WHERE(FINITE(EtoW, /NAN), /NULL)] = 0
NtoS = [WHERE(FINITE(NtoS, /NAN), /NULL)] = 0
v_EtoW = [WHERE(FINITE(v_EtoW, /INFINITY), /NULL)] = 0
v_NtoS = [WHERE(FINITE(v_NtoS, /INFINITY), /NULL)] = 0
EtoW2=EtoW & NtoS2=NtoS
EtoW2 = [WHERE(SNR LT SNRratio)] = 0 ; Remove SNR lower than SNR ratio input
NtoS2 = [WHERE(SNR LT SNRratio)] = 0
intens2 = SQRT((NtoS2^2) + (EtoW2^2))
EtoW2 = [WHERE(intens2 GT maxvelocity)] = 0 ; Remove SNR lower than SNR ratio input
NtoS2 = [WHERE(intens2 GT maxvelocity)] = 0
x = (proj.MC[2]+proj.ps[0]*INDGEN(nrows)) ; Rows (samples)
y = reverse(proj.MC[3]-proj.ps[1]*INDGEN(nlines)) ; Lines
v_x = v.proj.MC[2]+v.proj.ps[1]*INDGEN(v_nrows) ; Visual Rows (samples)
v_y = reverse(v.proj.MC[3]-v.proj.ps[1]*INDGEN(v_nlines)) ; Visual_Lines
v_NtoS_Sized = CONGRID(v_NtoS, nrows, nlines, /INTERP)
v_EtoW_Sized = CONGRID(v_EtoW, nrows, nlines, /INTERP)
intens = SQRT((NtoS2^2) + (EtoW2^2)) ; Intensity map
v_Intens = SQRT((v_NtoS2^2)+(v_EtoW2^2))
v_Intens_Sized = SQRT((v_NtoS_Sized^2)+(v_EtoW_Sized^2))
SNRmaxvelo = SNR
SNRmaxvelo = [WHERE(intens GT Maxvelocity)]=0
intensmaxvelo = intens
intensmaxvelo = [WHERE(intens GT Maxvelocity)]=0 ; Remove High velocities

; ----- i_ full raster Image -----
i_cross = (v_EtoW*NtoS) + (EtoW*v_NtoS) ; || A B || = A B sin(θ) = Ax By + Bx Ay = CROSS
i_dot = (v_EtoW*v_EtoW) + (v_NtoS*v_NtoS) ; A•B = A B cos(θ) = Ax Bx + Ay By = DOT
i_angle = 180/!PI*atan(i_cross,i_dot) ; tan(θ) = || A B || / A•B
i_e_NtoS = (NtoS-v_NtoS) ; NtoS relative towards visual
i_e_EtoW = (EtoW-v_EtoW) ; EtoW relative towards visual
i_e_intens = SQRT((i_e_EtoW^2)+(i_e_NtoS^2))
i_MAE = Mean(i_angle) ; Velocity Error
i_MVE = Mean(intens-v_Intens_Sized) ; Mean Angular Error (MAE)
; Scatterplot correlations
i_m = REGRESS(REFORM(v_Intens_Sized,N_elements(v_Intens_Sized)), $
; REFORM(intens,N_elements(intens)), CONST=i_b,CORRELATION=i_r)
i_r2 = i_r*i_r ; p_m = slope, p_b= B and p_r= R2
i_RMSE = SQRT(MEAN((v_Intens_Sized-intens)^2)) ; R2
; RMSE

; ----- P_Points -----
p_nr = points.field1 ; points, x and y
p_x = points.field2 ; points, x and y
p_y = points.field3
p_v_NtoS = points.field5 ; Table with p_v_NtoS (Visual)
p_v_EtoW = points.field4
p_NtoS = NtoS2(value_locate(x,p_x),value_locate(y,p_y)) ; Corresponding Points in Cosi-Corr
p_EtoW = EtoW2(value_locate(x,p_x),value_locate(y,p_y))
p_v_etow = abs(p_v_etow)*fix(abs(p_EtoW)/p_EtoW) ; Correct Sign
p_v_NtoS = abs(p_v_NtoS)*fix(abs(p_NtoS)/p_NtoS)
p_v_NtoS = float(p_v_NtoS)/days*365.0 ; Table with p_v_NtoS (Visual)
p_v_EtoW = float(p_v_EtoW)/days*365.0
p_v_Intens = SQRT((p_v_NtoS^2)+(p_v_EtoW^2))
p_intens = SQRT((p_NtoS^2) + (p_EtoW^2)) ; Intensity map
; Errors
p_cross = (p_v_EtoW*p_NtoS) + (p_EtoW*p_v_NtoS) ; || A B || = A B sin(θ) = Ax By + Bx Ay = CROSS
p_dot = (p_v_EtoW*p_EtoW) + (p_v_NtoS*p_NtoS) ; A•B = A B cos(θ) = Ax Bx + Ay By = DOT
p_angle = 180/!PI*atan(p_cross,p_dot) ; tan(θ) = || A B || / A•B
p_MAE = Mean(p_angle) ; Mean Angular Error (MAE)
p_MVE = Mean(abs(p_intens)-abs(p_v_intens)) ; Mean Velocity Error (MAE)
; Scatterplot correlations
p_m = REGRESS(p_v_intens,p_intens, CONST=p_b,CORRELATION=p_r) ; p_m = slope, p_b= B and p_r= R2
p_r2 = p_r*p_r ; R2
p_RMSE = SQRT(MEAN((p_v_intens-p_intens)^2)) ; RMSE
; Corrector Vector
p_e_NtoS = (p_NtoS-p_v_NtoS) ; NtoS relative towards visual
p_e_EtoW = (p_EtoW-p_v_EtoW) ; EtoW relative towards visual
p_e_intens = SQRT((p_e_EtoW^2)+(p_e_NtoS^2)) ; Velocity Error
; z = GRIDDATA(p_x,p_y, p_e_intens,DIMENSION=[nlines,nrows],/KRIGING )
; sdf=image (z) ; Spatial distribution of velocity error

; ----- Histograms -----
SNRH = float(HISTOGRAM(SNRmaxvelo, LOCATIONS=xbin1, $
; BINSIZE=0.02,MIN=0.0000001, MAX=1))/float($
; N_ELEMENTS(SNR[WHERE(SNR GT 0)]))
intensH = FLOAT(HISTOGRAM(intensmaxvelo, LOCATIONS=xbin2, $
; BINSIZE=0.05,MIN=0.0000001, MAX=Maxvelocity))$
; /float(N_ELEMENTS(SNR[WHERE(SNR GT 0)])) ; HISTOGRAMS Normalized, Corrected for NULL/NaN
visualH = HISTOGRAM(v_Intens, LOCATIONS=xbin3, $
; BINSIZE=0.05,MIN=0.0000001, MAX=Maxvelocity)$
; /float(N_ELEMENTS(v_Intens[WHERE(v_Intens GT 0)]))

; ----- Plotting -----
print, '% Start plotting' ;
colors=['red','green','blue','fuchsia','lime','black','maroon',$ ;
'dark green','dark blue','cyan','dark orange','dim grey','grey'] ; Plot colors
img=[2,3,4,6,7,8] ; Plot positions

; ----- OVERVIEW PLOT -----
if overview eq 1 then begin
; Signal to Noise (UPPER)
if statisticplot eq 0 then begin
SNRplot = PLOT(xbin1, SNRH, XRange=[0,1],YRange=[0,0.05], histogram=1, axis_style=1, $ ; PLOT Signal To Noise Ratio
; TITLE='Signal to Noise Histogram',XTITLE='SNR Ratio',YTITLE='pixels (%)',/current,$
; COLOR=colors(i),FONT_SIZE=9,LAYOUT=[4,2,1], /DEVICE, MARGIN=[250,80,50,80],$
; DIMENSIONS=[1500,800],FILL_BACKGROUND=1,FILL_TRANSPARENCY=95,FILL_COLOR=colors(i))
; SNR Threshold line
SNRline = PLOT(MAKE_ARRAY(n_elements(XBIN1),1,/float,VALUE=SNRratio),xbin1*25,/overplot,$ ; LINE SNR Threshold line
; AXIS_STYLE=1,TRANSPARENCY=50,color='grey')
; legend = TEXT([0.023*((SNRratio)*0.19)],[0.85], 'SNR Threshold',color='grey',FONT_SIZE=8,$ ; TEXT 'SNR Threshold'

```

```

TRANSPARENCY=50, target=SNRplot)&legend.rotate,90
endif;

;----- STATISTICS PLOT (UPPER) -----
if statisticplot eq 1 then begin
p_scatter = plot(p_v_intens,p_intens, xrange=[0,8],$ ; PLOT Scatterplot of points
yrange=[0,8],LINESTYLE=1,SYMBOL='dot',DIMENSIONS=[1500,800],$
sym_size=3.5,sym filled=1,/DEVICE,MARGIN=[250,80,50,80],$
/CURRENT,LAYOUT=[4,2,1],SYM TRANSPARENCY=75,$
TITLE='Points scatterplot',YTITLE='Cosi-Corr Velocities(m/a)',$
FONT_SIZE=9,XTITLE='Measured Velocities(m/a)',color=colors(i))
p_oneplot = plot(FINDGEN(81)/10,FINDGEN(81)/10,overplot=1,color='grey',thick=2) ; LINE 1:1 line. perfect corr
p_bestfit = plot(FINDGEN(81)/10,p_m##(FINDGEN(81)/10)+p_b,overplot=1,color=colors(i),thick=3) ; LINE Best fit line
endif;

;----- Velocity (LOWER) -----
intensplot = PLOT(xbin2,intensH,XRANGE=[0,Maxvelocity+1],YRANGE=[0,0.03],HISTOGRAM=1,$ ; PLOT Velocity Plot
AXIS_STYLE=1,TITLE='Velocity Histogram',XTITLE='Velocity [m/a]',LAYOUT=[4,2,5],$
COLOR=colors(i),/CURRENT,YTITLE='pixels (%)',/DEVICE,MARGIN=[300,80,50,80],$
FILL_BACKGROUND=1,FILL_TRANSPARENCY=95,FILL_COLOR=colors(i),FONT_SIZE=9)
Visualplot = PLOT(xbin3,visualH,YRANGE=[0,0.03],HISTOGRAM=1,AXIS_STYLE=1,COLOR='black',$
LAYOUT=[4,2,5],/DEVICE,MARGIN=[300,80,50,80],/CURRENT,XRANGE=[0,Maxvelocity+1],$
FONT_SIZE=9)
;Velocity Threshold line
VELOline= PLOT(MAKE_ARRAY(n_elements(XBIN2),1,/float,VALUE=MaxVelocity),xbin2*25,$ ; LINE Velo Threshold line
TRANSPARENCY=50,AXIS_STYLE=1,color='grey',/overplot)
legend = TEXT([0.023*((MaxVelocity-1)*0.19)/MaxVelocity],[0.35],'Velocity Threshold',$ ; TEXT 'SNR Threshold'
FONT_SIZE=8,TRANSPARENCY=50,target=intensplot,color='grey')&legend.rotate,90
;Percentage Velocities above 5 m/s
legend0 = TEXT([0.215],[0.095+(0.020)],STRING(float(N_ELEMENTS(v_Intens[WHERE($
v_Intens GT Maxvelocity,/null])))/float(N_ELEMENTS(INTENS[WHERE($
v_Intens GT 0,/null])))*100,format='(f0.1)')+ '%',FONT_SIZE=9,color='black') ; TEXT % Velo > 5 m/s manual
legend1 = TEXT([0.215],[0.095-(i*0.020)],STRING(float(N_ELEMENTS(INTENS[WHERE($
INTENS GT Maxvelocity,/null])))/float(N_ELEMENTS(INTENS[WHERE($
INTENS GT 0,/null])))*100,format='(f0.1)')+ '%',FONT_SIZE=9,color=colors(i)) ; TEXT % Velo > 5 m/s Auto
;----- Intensity Image RUN > 1 -----
;original_sized = CONGRID(original,nrows,nlines,/INTERP)
;im2= image(original_sized,x,y,/CURRENT,MARGIN=[0],/device,LAYOUT=[4,1,img(i)])
im = image(BYTSCL(float(intens)),MAX=MAXvelocity,MIN=0.000001,/NAN),x,y,/CURRENT,$ ; IMAGE Intensity Image
RGB_TABLE=11,MARGIN=[0],/device,LAYOUT=[4,1,img(i)],TRANSPARENCY=000)
if mask eq 1 then begin
imask = float(empty)
imask [WHERE(intens GT Maxvelocity OR SNR LT SNRratio AND SNR NE 0)]=1 ; Alpha High velocity = 1
intensScale = make_array(nrows,nlines,value=255)intensScale(1)=0 ; RGB Create black image
intensAlpha = {[intensScale]},[intensScale],$ ; RGBA Combine
[[intensScale]],[(imask)]]
imaskplot = image(intensAlpha,x,y,LAYOUT=[4,1,img(i)],$ ; MASK Mask to cover low SNR
/DEVICE,MARGIN=[0],/CURRENT)
endif
Colorbar = COLORBAR(POSITION=[0.26,0.08,0.49,0.09],FONT_SIZE=9,TICKNAME=['0',STRMID(string($ ; COLORBAR Colorbar
MAXvelocity*0.25),6,4),STRMID(string(MAXvelocity*0.5),5,5),STRMID(string($
MAXvelocity*0.75),6,4),STRMID(string(MAXvelocity),6,4)+'m/a'],TARGET=im)
legend2 = TEXT([0.3+(i*0.25)], [0.95],name,color=colors(i),FONT_SIZE=11) ; TEXT Headers
p_plot_r2 = TEXT([0.3+(i*0.25)], [0.92],R2:'+'STRING($
p_r2,format='(f0.3)'),FONT_SIZE=9,color=colors(i))
p_plot_m = TEXT([0.35+(i*0.25)], [0.92],m:'+'STRING($
p_m,format='(f0.3)'),FONT_SIZE=9,color=colors(i))
p_plot_rmse = TEXT([0.4+(i*0.25)], [0.92],RMSE:'+'STRING($
p_rmse,format='(f0.3)'),FONT_SIZE=9,color=colors(i))
legend3 = TEXT([0.26+(i*0.25)], [0.16],STRCOMPRESS(nrows)+$ ; NUMBER Dimensions in pixels
'x'+STRCOMPRESS(nlines),color='white',FONT_SIZE=9)
legend4 = TEXT([0.262+(i*0.25)], [0.145],STRING($ ; NUMBER PixelSize in meters
proj.PS(1),format='(f0.1)')+ 'm/px',color='white',FONT_SIZE=9)
legend5 = TEXT([0.26+(i*0.25)], [0.175],STRMID(ROUND(n_elements(v_x))+ 'x'+STRCOMPRESS($ ; NUMBER Coverage of data
GT 0.00001))/ (nlines*nrows*ROIpercent)*100,9)+'%',color='white',FONT_SIZE=9)
;----- Visual Image RUN = 1 -----
if RUNS eq 1 THEN BEGIN
im2 = image(BYTSCL(REVERSE(float(v_Intens),2),MAX=MAXvelocity,MIN=0.000001,$ ; IMAGE Show Visual image
/NAN),v_x,v_y,LAYOUT=[4,1,3],/DEVICE,MARGIN=[0],/CURRENT,xrange=[min(x),max(x)]$)
;
; yrange=[min(y),max(y)],RGB_TABLE=11)
im2 = image(BYTSCL(REVERSE(float(v_Intens_sized),2),MAX=MAXvelocity,MIN=0.000001,$ ; IMAGE Show Visual image
/NAN),x,y,LAYOUT=[4,1,3],/DEVICE,MARGIN=[0],/CURRENT,xrange=[min(x),max(x)]$)
; yrange=[min(y),max(y)],RGB_TABLE=11)
; p_plot
; plot(points.FIELD1),(points.FIELD2),SYMBOL='circle',sym_size='0.5',/current,$ ; POINTS Visual points
; SYM FILLED=1,SYM_FILL COLOR='gold',LINESTYLE=1,LAYOUT=[4,1,3],AXIS_STYLE=0,$
; xrange=[min(x),max(x)],yrange=[min(y),max(y)]
;----- Difference Image RUN = 1 -----
im3 = image(BYTSCL(REVERSE(float(v_Intens_Sized-REVERSE(intens,2)),2),MAX=Maxvelocity,$ ; IMAGE Show difference
MIN=0.000001,/NAN),MARGIN=[0],/CURRENT,LAYOUT=[4,1,4],/DEVICE)
;imaskplot = image(intensAlpha,x,y,LAYOUT=[4,1,4],/DEVICE,MARGIN=[0],/CURRENT) ; MASK Plot Mask SNR
Colorbar = COLORBAR(POSITION=[0.76,0.08,0.99,0.09],FONT_SIZE=9,TICKNAME=['0',STRMID($ ; COLORBAR Plot Colorbar
MAXvelocity*0.5),6,3),STRMID(MAXvelocity),6,3)+'m'],TARGET=im3)
v_legend3 = TEXT([0.26+(0.25)], [0.16],STRCOMPRESS(n_elements(v_x))+ 'x'+STRCOMPRESS($ ; NUMBER Dimensions in pixels
N_ELEMENTS(transpose(v_y))),color='white',FONT_SIZE=9)
v_legend4 = TEXT([0.262+(0.25)], [0.145],STRMID(STRING($ ; NUMBER PixelSize in meters
proj.PS(1),7,4)+'m/px',color='white',FONT_SIZE=9)
endif;
endif;

if RUNS eq 1 AND vectorplot eq 1 THEN BEGIN
;----- VECTOR PLOT -----
v = VECTOR(transpose(NtoS),-transpose(EtoW), (y), reverse(x), $ ; Vector Map
/DEVICE,MARGIN=[0],dimensions=[2000,2000],$
auto_color=1,RGB_TABLE=11,AUTO_RANGE=[0.0001,$
Maxvelocity],ASPECT_RATIO=1,AXIS_STYLE=0)
endif;

;----- Scatter PLOT -----
if scatterplot eq 1 then begin
i_scatter = plot(REFORM(v_intens,N_elements(v_intens)),reverse(REFORM(intens,$
N_elements(intens))), xrange=[0,8],SYM TRANSPARENCY=75,$
yrange=[0,8],LINESTYLE=1,SYMBOL='dot',DIMENSIONS=[1500,800],$
sym_size=3.5,sym filled=1,/DEVICE,MARGIN=[250,80,50,80],$
TITLE='Points scatterplot',YTITLE='Cosi-Corr Velocities(m/s)',$
FONT_SIZE=9,XTITLE='Visual Velocities(m/s)',color=colors(i))
i_oneplot = plot(FINDGEN(81)/10,FINDGEN(81)/10,overplot=1,color='grey',thick=2)
i_bestfit = plot(FINDGEN(81)/10,i_m##(FINDGEN(81)/10)+i_b,overplot=1,color=colors(i),thick=3)
endif;

;----- Output -----
;
;
;
;
;
end_time = (Systemtime(1)-mid_time)& IF end_time LE '60' THEN print, '% Duration handling: '+ $
;

```

```

STRCOMPRESS(string(round(end_time))+'sec' ELSE print,$
'% Duration handling:' + STRCOMPRESS(string(round(end_time/60)))+'min'
print,'% Run finished' & print, '% Full image ' $
+ ' MAE: '+STRCOMPRESS(string(i_MAE)) $
+ ' MVE: '+STRCOMPRESS(string(i_MVE)) + ' RMSE: ' +STRCOMPRESS(string(i_RMSE)) $
+ ' R2: ' +STRCOMPRESS(string(i_r2)) + ' m: '+STRCOMPRESS(string(i_M))
print, '% Sample Points ' $
+ ' MAE: '+STRCOMPRESS(string(p_MAE)) $
+ ' MVE: '+STRCOMPRESS(string(p_MVE)) + ' RMSE: ' +STRCOMPRESS(string(p_RMSE)) $
+ ' R2: ' +STRCOMPRESS(string(p_r2)) + ' m: '+STRCOMPRESS(string(p_M))
print, '% Velocities above '+STRMID(maxvelocity,7,3)+' m/s is '+STRMID((STRING(float(N_ELEMENTS(INTENS[WHERE(INTENS $
GT Maxvelocity, /null])))/float(N_ELEMENTS(INTENS[WHERE(INTENS GT 0, /null])))*100,6,4)+'%'
;

; ----- Save Images -----
IF savefiles EQ 1 THEN BEGIN
print, '% Saving files'
ENVI_WRITE_ENVI_FILE,reverse(EtoW,2), out_name=string(i,format='(I0)')+ '_EtoW'+STRJOIN(STRSPLIT(name,'.', ':', &
/EXTRACT),' '),/INVISIBLE,MAP_INFO=proj
ENVI_WRITE_ENVI_FILE,reverse(NtoS,2), out_name=string(i,format='(I0)')+ '_NtoS'+STRJOIN(STRSPLIT(name,'.', ':', &
/EXTRACT),' '),/INVISIBLE,MAP_INFO=proj
ENVI_WRITE_ENVI_FILE,reverse(SNR,2), out_name=string(i,format='(I0)')+ '_SNR'+STRJOIN(STRSPLIT(name,'.', ':', &
/EXTRACT),' '),/INVISIBLE,MAP_INFO=proj
ENVI_WRITE_ENVI_FILE,reverse(intens,2),out_name=string(i,format='(I0)')+ '_Intensity'+STRJOIN(STRSPLIT(name,'.', ':', &
/EXTRACT),' '),/INVISIBLE,MAP_INFO=proj
;v.save, "test.png", RESOLUTION=300, /TRANSPARENT, height=2000, width=2000,ANTIALIAS=1
ENDIF
;

; ----- Save Results -----
IF test eq 0 THEN BEGIN
openu, lun, txtfile, /GET LUN, /APPEND
printf,lun,format='(250($,f0.4,""))',i_MAE,i_MVE,i_r2,i_RMSE,i_m,p_MAE,p_MVE,p_r2,p_RMSE,p_M,$
(float(N_ELEMENTS(INTENS[WHERE(INTENS GT Maxvelocity, /null)]))/float(N_ELEMENTS(INTENS[WHERE(INTENS GT 0, /null)])), $
(n_elements(intens[WHERE(intens GT 0.00001)])/(nlines*nrows*ROIpercent)*100, (proj.PS(1)),end_time,p_b,i_b
printf,lun,name+', ' +time
free_lun, lun
ENDIF
;

; ----- Save CSV points -----
csvfile= string(i,format='(I0)')+STRJOIN(STRSPLIT('CSV '+STRJOIN(STRSPLIT(name,'.', ':', /EXTRACT),' ')+ '_R2'+STRMID(p_r2,format='(f0.3)')+ $
' RMSE '+STRMID(p_rmse,format='(f0.3)')+ '_B'+STRMID(p_b,format='(f0.3)')+ '_M'+STRMID(p_m,format='(f0.3)')+ $
'_MAE'+STRMID(p_mae,format='(f0.3)')+ '_MVE'+STRMID(p_mve,format='(f0.3)')+ '_ ', /EXTRACT),'-')+ '.csv'
OPENW, lun, csvfile, /GET LUN
printf,lun, 'Nx','X','Y','V_EtoW','V_NtoS','EtoW','NtoS','AE','VE' ; Open Existing file
for j=0,size(p_nr, /N_ELEMENTS)-1 DO BEGIN ; Header
printf,lun, format='(600(f0,""))',p_nr(j),p_x(j),p_y(j),p_v_EtoW(j),p_v_NtoS(j), $ ; Info per point
p_etow(j),p_ntos(j),p_angle(j),p_intens(j)-p_v_intens(j)
ENDFOR
free_lun, lun ; closes the file
;

;
;_p_scatter = plot(p_v_intens,p_intens, xrange=[0,8],$ ; PLOT Scatterplot of points
; yrange=[0,8],LINESTYLE='',SYMBOL='dot',DIMENSIONS=[1500,800],$
; sym_size='3.5',sym_filled=1,TITLE='Points scatterplot', YTITLE='Cosi-Corr Velocities (m/a)', $
; FONT_SIZE=9, XTITLE='Measured Velocities (m/a)',color=colors(i)
; p_oneplot = plot(FINDGEN(81)/10,FINDGEN(81)/10,overplot=1,color='grey', thick=2) ; LINE One to one line. perfect correlation
;_p_bestfit = plot(FINDGEN(81)/10,1/p_m##(FINDGEN(81)/10)-p_b,overplot=1,color=colors(i), thick=3) ; LINE Best fit line of scatter plot
;dsf=plot(p_v_ntos)
;dsf2=plot(p_ntos,overplot,'r')
;
;
;
;_G_scatter = plot(p_v_intens,G_intens,LINESTYLE='',SYMBOL='dot',sym_size='3.5',sym_filled=1,overplot,$
; /CURRENT, SYM_TRANSPARENCY=75,color='green')
;_G_bestfit = plot(FINDGEN(81)/10,G_m##(FINDGEN(81)/10)+G_b,overplot=1,color='green', thick=3) ; LINE Best fit line of scatter plot
;print, '% Sample Points ' $
;+ ' MAE: '+STRCOMPRESS(string(p_MAE)) $
;+ ' MVE: '+STRCOMPRESS(string(p_MVE)) + ' RMSE: ' +STRCOMPRESS(string(g_RMSE)) $
;+ ' R2: ' +STRCOMPRESS(string(g_r2)) + ' m: '+STRCOMPRESS(string(g_M))
;
; ----- END LOOP (i) -----
ENDFOR;
;
model_time = (Systime(1)-timesecconds) & print, s & IF model_time LE '60' THEN print, '% ----- Model '+MAP+ ' is finished in'+ $
STRCOMPRESS(string(round(model_time))+' sec -----' ELSE print,$
'% ----- Model '+MAP+ ' is finished in'+ STRCOMPRESS(string(round(model_time/60))+' min -----' & END
;
; ----- END -----

```